Summer 2009

High power mid-wave and long-wave infrared light emitting diodes: device growth and applications

Edwin John Koerperick
University of Iowa

HIGH POWER MID-WAVE AND LONG-WAVE INFRARED SUPERLATTICE LIGHT EMITTING DIODES: DEVICE GROWTH AND APPLICATIONS

by

Edwin John Koerperick

An Abstract

Of a thesis submitted in partial fulfillment of the
requirements for the Doctor of Philosophy
degree in Electrical and Computer Engineering in the
Graduate College of The
University of Iowa

July 2009

Thesis Supervisors: Professor Thomas F. Boggess
Professor John P. Prineas

ABSTRACT

High brightness light emitting diodes based on the InAs/GaSb superlattice material system have been developed for use in mid-wave and long-wave infrared optoelectronic systems. By employing a multiple-active region device configuration, high optical output has been demonstrated from devices in the 3-5 μm and 7-12 μm spectral bands. Mid-wave infrared optical output in excess of 0.95 mW/sr has been observed from 120×120 μm^2 devices with peak emission at 3.8 μm, and nearly 160 μW/sr has been measured from devices of the same size operating at 8 μm. Larger devices (1×1 mm^2) with output as high as 8.5 mW/sr and 1.6 mW/sr have been demonstrated with mid-wave and long-wave devices, respectively, under quasi-DC bias conditions.

The high switching speed inherent to small area light emitting diodes as well as potentially high optical output make these devices appealing candidates to improve upon the current state-of-the-art in infrared projection technology. Simulation of thermal scenes with wide dynamic range and high frame rates is desirable for calibration of infrared detection systems. Suitable projectors eliminate the need for observation of a live scene for detector calibration, thereby reducing costs and increasing safety. Current technology supports apparent temperature generation of up to approximately 800 kelvin with frame rates of hundreds of frames per second; strong desire exists to break these barriers.

Meeting the requirements of the aforementioned application requires development of the InAs/GaSb superlattice material system on multiple levels. Suppressing parasitic recombination channels via band structure engineering, improving carrier transport between active regions and confinement within active regions, reduction of defect-assisted recombination by optimizing device growth, and improving device fabrication and packaging are all routes requiring exploration. This work focuses on the latter two components of the optimization process, with emphasis on molecular beam epitaxial growth

of high quality devices. Particular attention was paid to tailoring devices for thermal imaging applications and the design tradeoffs and limitations which impact that technology. Device performance and optimization success were gauged by electronic, optical, morphological, and structural characterization.

Abstract Approved: _____
Thesis Supervisor

_____
Title and Department

_____
Date

_____
Thesis Supervisor

_____
Title and Department

_____
Date

HIGH POWER MID-WAVE AND LONG-WAVE INFRARED SUPERLATTICE LIGHT EMITTING DIODES: DEVICE GROWTH AND APPLICATIONS

by

Edwin John Koerperick

A thesis submitted in partial fulfillment of the
requirements for the Doctor of Philosophy
degree in Electrical and Computer Engineering in the
Graduate College of The
University of Iowa

July 2009

Thesis Supervisors: Professor Thomas F. Boggess
Professor John P. Prineas

Graduate College
The University of Iowa
Iowa City, Iowa

CERTIFICATE OF APPROVAL

PH.D. THESIS

This is to certify that the Ph.D. thesis of

Edwin John Koerperick

has been approved by the Examining Committee for the thesis requirement for the Doctor of Philosophy degree in Electrical and Computer Engineering at the July 2009 graduation.

Thesis Committee:

Thomas F. Boggess, Thesis Supervisor

John P. Prineas, Thesis Supervisor

David R. Andersen

Sudhakar M. Reddy

Hassan Raza

Christopher M. Cheatum

ACKNOWLEDGMENTS

I would foremost like to thank my advisor, Tom Boggess, for his guidance and support throughout my graduate career. Tom also encouraged my research ambitions as an undergraduate; my experience during that time inspired me to continue my education. I appreciate very much Tom's flexibility, as I was encouraged to participate in many aspects of research; ranging from ultrafast spectroscopy to molecular beam epitaxy. In addition, I had the experience of helping rebuild Tom's labs after flooding largely destroyed the first floor of the IATL facility in 2008. While the acquisition and setup of state-of-the-art equipment and experiments in the aftermath was an exciting (and often irritating) challenge, I believe we all agree that the evacuation, cleanup, and de-mucking processes is something we'd rather not repeat.

Professor John Prineas was kind enough to allow me to work extensively with his group on molecular beam epitaxial growth, the results of this collaboration are the foundation of this thesis. I appreciate the time John invested to work with me, and hope that I was able to make a positive contribution to his research efforts as well.

My interaction with past and present group members and collaborators has been invaluable. It was a pleasure to work with Kimberley Hall and Kenan Gündoğdu, who were kind enough to involve me with research on ultrafast phenomena in semiconductor quantum dots. Jim Hicks, Dennis Norton, and Ben Olson have all provided valuable support; this work is certainly sounder thanks to their involvement. I would especially like to thank Jon Olesberg, who offered patience and guidance in working with me on LED development, as well as allowed me to make use of his $\mathbf{K} \cdot \mathbf{p}$ software which was used to generate numerous models in this thesis.

I am also indebted to my parents, Richard and Mary Koerperick; their continual support will be forever appreciated. More than once I had questioned whether nine years of higher education would be tolerable; their moral support helped overcome my

reservations.

The staff at the University of Iowa Central Microscopy Research Facility (CMRF), and in particular Jonas Baltrusaitis and Jean Ross, have been extremely helpful with equipment training and data analysis. All atomic force and scanning electron microscope images, as well as XPS data presented in this thesis, were acquired at the CMRF. I appreciate the eagerness from the CMRF staff to assist me with imaging tasks which were novel to the facility at the time; it is an indispensable multidisciplinary resource.

Finally, I would like to thank the Test Resource Management Center (TRMC) Test and Evaluation/Science and Technology (T&E/S&T) Program for their support. This work was funded by the T&E/S&T Program through the University of Iowa contract number W91ZLK-06-C-0006.

ABSTRACT

High brightness light emitting diodes based on the InAs/GaSb superlattice material system have been developed for use in mid-wave and long-wave infrared optoelectronic systems. By employing a multiple-active region device configuration, high optical output has been demonstrated from devices in the 3-5 μm and 7-12 μm spectral bands. Mid-wave infrared optical output in excess of 0.95 mW/sr has been observed from 120×120 μm^2 devices with peak emission at 3.8 μm, and nearly 160 μW/sr has been measured from devices of the same size operating at 8 μm. Larger devices (1×1 mm^2) with output as high as 8.5 mW/sr and 1.6 mW/sr have been demonstrated with mid-wave and long-wave devices, respectively, under quasi-DC bias conditions.

The high switching speed inherent to small area light emitting diodes as well as potentially high optical output make these devices appealing candidates to improve upon the current state-of-the-art in infrared projection technology. Simulation of thermal scenes with wide dynamic range and high frame rates is desirable for calibration of infrared detection systems. Suitable projectors eliminate the need for observation of a live scene for detector calibration, thereby reducing costs and increasing safety. Current technology supports apparent temperature generation of up to approximately 800 kelvin with frame rates of hundreds of frames per second; strong desire exists to break these barriers.

Meeting the requirements of the aforementioned application requires development of the InAs/GaSb superlattice material system on multiple levels. Suppressing parasitic recombination channels via band structure engineering, improving carrier transport between active regions and confinement within active regions, reduction of defect-assisted recombination by optimizing device growth, and improving device fabrication and packaging are all routes requiring exploration. This work focuses on the latter two components of the optimization process, with emphasis on molecular beam epitaxial growth

of high quality devices. Particular attention was paid to tailoring devices for thermal imaging applications and the design tradeoffs and limitations which impact that technology. Device performance and optimization success were gauged by electronic, optical, morphological, and structural characterization.

TABLE OF CONTENTS

LIST OF TABLES

Table

LIST OF FIGURES

Figure

CHAPTER 1
INTRODUCTION

Interest in infrared optical technology continues to grow as an ever increasing number of applications are discovered in academia, industry, and the military. While solid state emitters and detectors of optical radiation in the visible and near infrared (NIR) are numerous and well studied, devices operating in the mid-wave (MWIR) and long-wave infrared (LWIR) require further development to improve efficiency, output power, and device fabrication. The infrared region of the electromagnetic spectrum lies between the terahertz and visible bands as shown in Figure 1.1. As atmospheric absorption of radiation in the 3-5 μm and 8-12 μm bands is minimal, these regions of the spectrum may be exploited for a variety of purposes. Optoelectronics in the IR have applications in healthcare, spectroscopy, imaging, and defense to name a few. In order to realize the full potential of solid state optical devices in the IR, further development is needed to improve device performance and reduce development and manufacturing costs.

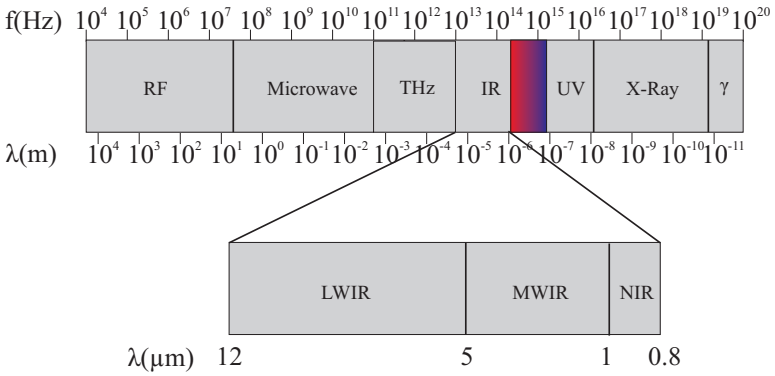

Figure 1.1: The spectrum of electromagnetic radiation. While uses are widespread and instrumentation abundant for radiation in spectral bands such as RF, microwave, and (visible) optical, the technology to exploit the MWIR, LWIR, and THz bands requires further development.

Infrared optoelectronics based on the InAs/Ga(In)Sb superlattice (SL) material

system pose many potential advantages to competing technologies for MWIR and LWIR infrared emission and detection. Currently the most common detector systems in the infrared are based on HgCdTe (MCT) for LWIR, and InSb for MWIR detection. While the device performance of MCT detectors may approach theoretical limits, several drawbacks exist for this material system. MCT devices must be cooled, often to cryogenic temperatures, to suppress device heating and parasitic Auger recombination [1]. Epitaxial growth of this system poses difficulties in compositional control and homogeneity across wafers due to the high background pressure of mercury during growth [2]. The MCT material system has also been employed in negative and positive luminescent devices [3], however output powers from these devices are limited, with emission in the nanowatt regime [4].

Thermal emitters require high physical device temperatures to produce moderate optical output and apparent temperatures, as the emission spectrum is broadband in nature, often that of a grey body. Thin film resistor arrays are the current state-of-the-art technology for infrared scene generation (ISG), whereby a thermal scene may be projected from an array of emitters onto a suitable detector array (camera) [5, 6]. Conventional deposition and lithography techniques are employed to pattern a resistor array on a silicon substrate, and individual elements are addressed by corresponding drive electronics. The frame refresh rate is slow in these devices due to the long thermal time constant of several milliseconds, posing limitations where high speed imaging is desired. High frame rates minimize so-called "ghosting" of a scene, whereby an undesired replica image trails behind the intended image. Resistive emitter arrays with resolution as high as 1024×1024 and apparent temperature capability exceeding 700 K have been realized, however there is much interest in exploring alternative technologies to surpass the capabilities of resistive systems.

Detectors and emitters based on InAs/Ga(In)Sb SLs have the useful property of tunability of the operating wavelength throughout the MWIR and LWIR spectral bands,

as well as other useful characteristics which will be described in the following. Such a broad range of spectral operation makes this material system suitable for a variety of applications. Single element detectors have been demonstrated with performance similar to that obtainable with HgCdTe detectors [7]. Infrared detector arrays are being developed by several research groups in hope of improving upon HgCdTe-based cameras [8, 9, 10]. Growth of two detector regions with different cutoff wavelengths may be used to yield dual-band detectors [11]. In the case of emitters, coupling multiple active regions which are tuned to different emission wavelengths allows a single pixel to emit radiation in several spectral bands simultaneously. Laser diodes based on the InAs/Ga(In)Sb system, or multilayer SLs incorporating InAs/Ga(In)Sb layers, have also been realized [12, 13, 14].

This work focuses on the development of InAs/GaSb LEDs for use in infrared projection systems. Efforts were also made to develop high power single element devices which may be useful in infrared sensing and spectroscopic applications. Optimization of the MBE growth and device active regions benefits both goals simultaneously, as identical device wafers can be used in both applications. Separate device fabrication and packaging schemes are necessary to individually address the issues pertinent to high power output and high density LED arrays. Generally, high power LEDs require fabrication with a relatively large device size, on the order of 1×1 mm^2, to allow high input current levels and packaging of the devices in a manner which most efficiently extracts the optical emission. Large format infrared LED arrays require a substantially smaller size of the LED mesa in order to keep the pixel pitch and overall array size small. Device size and pixel pitch in this case are often governed by the physical layout of existing infrared cameras which are used for detection, as well as the limitations imposed by growth, fabrication, and packaging. Values of array pitch in the range of 48×48 μm^2 to 120×120 μm^2 allow compatibility with existing drive electronics, testing facilities, and focal plane array detectors.

1.1 III-V Semiconductor Materials for Infrared Applications

Compound semiconductors with constituents in groups III and V of the periodic table may be employed in bulk, alloy, or multiple layer structures to grow materials suited for infrared applications. Of particular interest are InAs, GaSb, and AlSb (the so-called 6.1 Å compounds) as these materials possess similar lattice constants as shown in Figure 1.2.

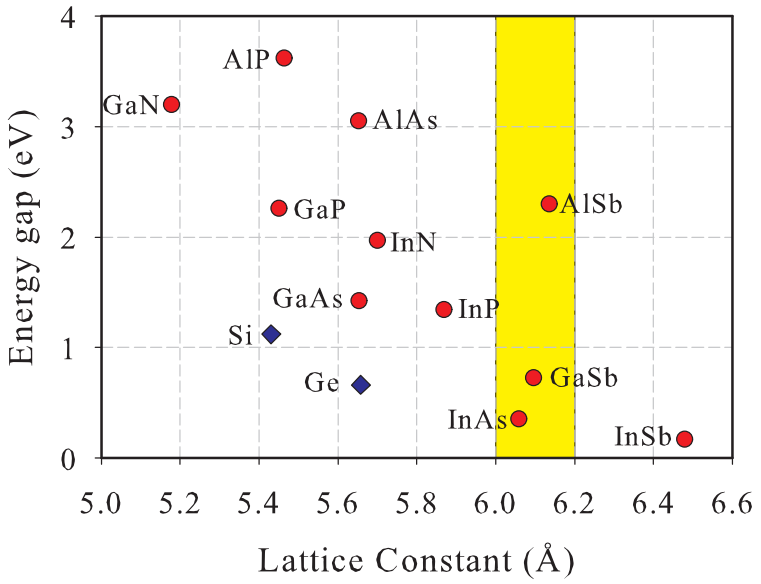

Figure 1.2: Lattice constants and energy gaps of several semiconductor materials. Materials in the III-V system are marked by circles, and elemental semiconductors by diamonds.

Using materials with similar lattice constants reduces the effect of strain and lifts certain restrictions on layer thickness that are imposed by strain. The lattice mismatch between InAs and GaSb is only 0.62%, which is useful for producing quasi lattice-matched structures where overall device strain may be minimized. In contrast, GaSb grown on GaAs yields a mismatch of 7.3%, which can lead to high levels of defects and dislocations in the subsequent structure if measures are not taken to include transition

layers or thick buffer layers which smooth the growth surface and reduce dislocations in the device [15, 16]. Use of GaAs as a substrate for growth of infrared devices is attractive due to the availability of semi-insulating substrates which are very transparent throughout the infrared spectrum, having an absorption coefficient on the order of only 2 cm^{-1}. Dislocations result from the tendency of the material to relieve the effects of strain and allow the lattice to enter a lower energy state. The formation of dislocations in strained systems can also be viewed as the tendency of the system to undergo an increase in entropy. Defects and dislocations break the translational symmetry of the crystal lattice; providing paths for nonradiative recombination and electrical shorting. A primary task in the design and growth of semiconductor structures is reduction of imperfections in the crystal which degrade device performance.

According to force balance and energy balance considerations in the material, the critical layer thickness (CLT) is the maximum thickness of a layer whereby all of the mismatch is accommodated by coherent strain [17]. Layers thicker than a given CLT experience misfit dislocation formation to accommodate the lattice mismatch. In the case of InAs grown on a GaSb substrate, the calculated CLT is approximately 200 Å, however experimentally obtained values of the CLT are often much larger [18]. It is, from a structural point of view, thus desirable to grow InAs/Ga(In)Sb devices on GaSb substrates whenever possible to avoid large lattice mismatch and the inevitable defects generated with large-mismatch heteroepitaxy.

Unintentionally doped GaSb has a background p-type dopant concentration of 10^{16}-10^{17} cm^{-3} due to a native defect [19, 20], and consequently high intervalence band absorption. Lightly n-doped GaSb substrates, on the other hand, exhibit relatively low absorption coefficients in the MWIR as shown in Figure 1.3. Absorption in the LWIR is considerably higher, however substrate thinning to reduce absorption is often a simpler approach than growing on mismatched substrates. Absorption of photons by intersubband transitions and free carriers attenuates light passing through a material,

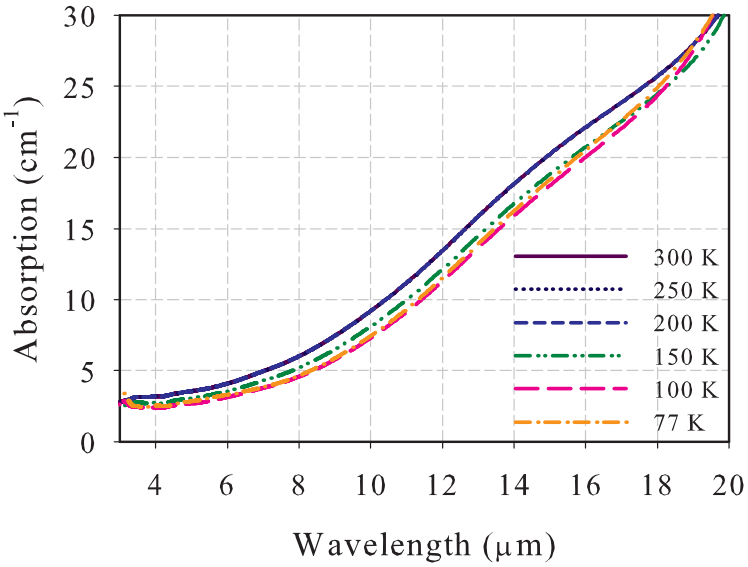

Figure 1.3: Temperature dependent absorption plots of Te-doped GaSb taken by FTIR spectroscopy. The room temperature n-doping density was given as $\sim 6.6 \times 10^{16}$ cm^{-3} by the vendor.

effects which are more pronounced at longer wavelengths. In the process of free carrier absorption, a photon loses its energy to an electron or hole which is excited to a higher energy state within the conduction or valence band, respectively. Free carrier absorption scales as λ^2, and thus is especially problematic in the long-wave infrared. Intersubband absorption is due to transitions within the conduction and valence bands, and may cause considerable absorption losses at long wavelengths.

1.2 Semiconductor Heterostructures

The periodic and closely packed arrangement of atoms in a solid gives rise to continuum energy levels called energy bands. The structure of the energy bands determines the electronic and optical properties of the solid; it is thus useful to have the ability to tailor a crystal to have a given set of electronic properties by properly designing the layer structure and constituent compositions. Epitaxial growth techniques are well suited to this task, as very thin layers may be deposited in a controlled manner. A

plethora of devices may be realized by properly choosing the constituent materials and their placement in the growth stack. Contrary to a homostructure where a device consists of the same material with regions of different doping levels, a heterostructure device employs layers of different composition which are in atomic contact. The ability to grow high quality materials with abrupt changes in composition is exceedingly significant for optoelectronic devices [21].

Placing a layer of material such as GaAs between barrier layers of a material with a larger bandgap such as AlGaAs [an example of a type-I alignment, Figure 1.4(a)] creates a quantum well potential which, given a sufficiently thin well region, yields

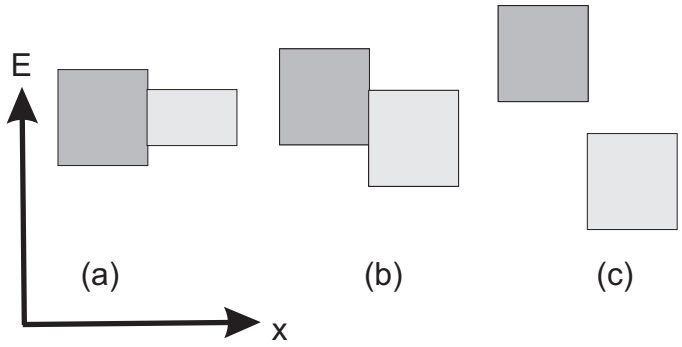

Figure 1.4: Band alignments of semiconductors in atomic contact, where (a) is type I, (b) is type II offset, and (c) is type II broken-gap.

discrete energy levels in the growth direction. Still further confinement may be imposed on a semiconductor material by employing growth conditions which encourage two and three-dimensional growth. Quantum dot structures are grown by depositing a thin layer of only a few monolayers of material onto a material with a smaller lattice constant. The effects of strain thereby cause three dimensional growth and essentially remove the three spatial degrees of freedom of a charge carrier, causing pronounced quantization of the energy levels.

An interesting case of the semiconductor heterostructure is the superlattice: a periodic repetition of semiconductor layers which exhibits properties different than the

component materials [22]. Superlattice devices where InAs and Ga(In)Sb are the component layers [23] have a type II broken-gap band alignment as shown in Figure 1.4 (c). The optical properties of a heterostructure depend upon the alignment of the bands and the degree of overlap between the electron and hole wavefunctions. Structures such as InAs/Ga(In)Sb superlattices comprise a system where electrons and holes are principally localized in different layers, leading to spatially-indirect transitions. Under equilibrium, holes tend to localize in the Ga(In)Sb material, and electrons in the InAs, as shown in Figure 1.5. For thin layers the electron-hole wavefunction overlap is appreciable in

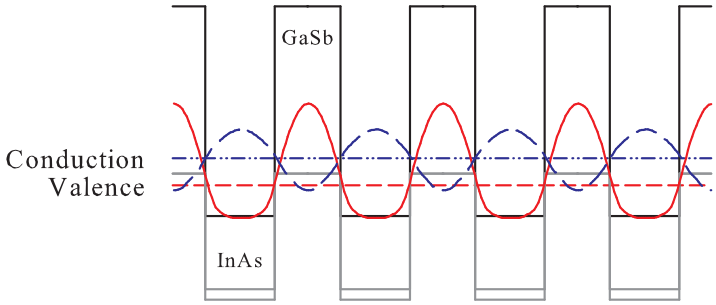

Figure 1.5: Type-II band alignment of the InAs/GaSb superlattice system. Black lines denote the conduction band, gray indicates the heavy and light valence bands. The envelope function of the valence state (solid) is well localized to the GaSb regions, having a value of nearly zero in the InAs layers. The conduction envelope function (long dash) shows reduced confinement compared to holes due to the light electron effective mass in InAs and consequently lower resistance to tunneling. The conduction (dot-dashed) and valence (short dashed) bulk band edges of the superlattice show a bandgap smaller than either of the constituent layers.

this system, which may lead to a high interband transition probability. Tuning of the energy gap in InAs/Ga(In)Sb superlattices is possible by varying the layer thicknesses. Increasing the thickness of the Ga(In)Sb layer, for instance, typically causes a blue shift in the energy gap, while increasing the thickness of InAs causes a red shift. In the

extreme case of very thick layers, the energy gap approaches zero and the superlattice behaves as a semimetal. Thinning of the superlattice such that the layers are thinner than the electron de Broglie wavelength imposes quantum confinement on the carriers. Sufficiently thin layers cause separation of the electron and hole states, thereby forming a bandgap. The small bandgaps achievable with the InAs/Ga(In)Sb system make it a particularly attractive solution for MWIR and LWIR detectors [24] and emitters [25].

A potentially useful degree of freedom in the type-II superlattices is the incorporation of indium in the GaSb layers. Several advantages may be realized by replacing the binary compound with a ternary: thinner layers may be used, strain in the $Ga_{1-x}In_xSb$ causes splitting of the hole states and may suppress nonradiative recombination, the density of states in the valence and conduction bands may be better matched, and the addition of indium yields design flexibility. The indium content in the GaSb material acts to increase the lattice constant, making the $Ga_{1-x}In_xSb$ layers compressively strained to a GaSb substrate. As an example, Figure 1.6 shows the band structures for a binary-binary and a binary-ternary type-II superlattice: both have the same energy gap. While the bandgap is 130 meV at 77 K in both cases (cutoff wavelength of 9.5 μm), the splitting of the heavy and light hole states is nearly resonant with the bandgap in the binary-binary case, however the resonance is removed by using the ternary compound. Using strain to separate the hole states is useful in suppressing band-to-band Auger recombination processes which require conservation of energy and momentum. Narrow bandgap materials may experience enough hole state splitting to provide a useful amount of Auger suppression. The apparent lack of dispersion in the growth direction for the top hole states in Figure 1.6 owes to the high degree of confinement of the holes to the Ga(In)Sb layers and correspondingly high effective mass. Dispersion calculation in the growth direction was carried out to the boundary of the mini-zone, or $k_z = \pi/d_{SL}$ where k_z is the growth direction wave vector and d_{SL} is the superlattice period.

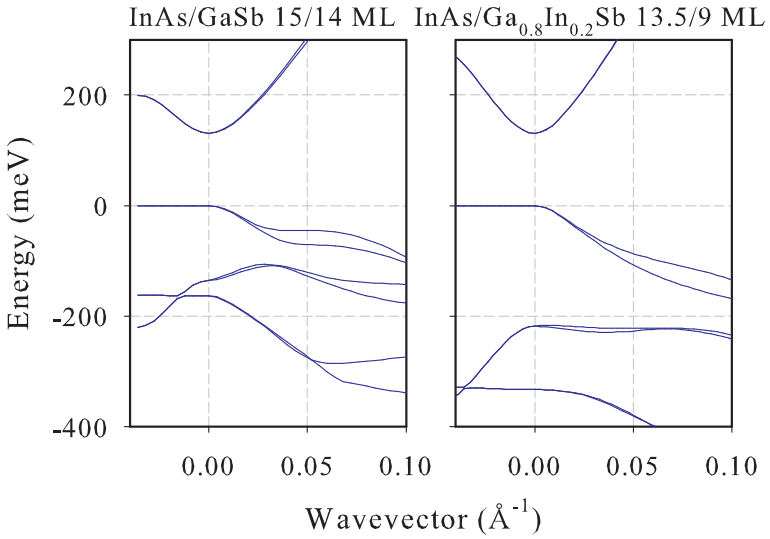

Figure 1.6: Band structures of InAs/GaSb (left) and InAs/$Ga_{1-x}In_xSb$ (right) superlattices at 77 K with the same energy gap. The bandgap in both cases is 130 meV, however heavy-light hole splitting is increased by 87 meV for the binary-ternary case.

1.3 Other Efforts in Infrared Emitters

The development of useful infrared emitters poses many challenges related to both design and material growth. Semiconductor emitters operating in the MWIR and LWIR are more susceptible than their shorter-wavelength analogs to processes such as Auger recombination and intersubband absorption, and care should be taken to minimize these effects. Band engineered structures, such as InAs/Ga(In)Sb SLs may be designed to suppress Auger processes, and growth conditions optimized to reduce Shockley-Read-Hall (SRH) recombination centers. Structures operating at longer wavelengths are also less favorably suited to emit photons via spontaneous emission, as the coefficient of such an event is expressed as

$$A = \frac{\omega_0^3 |\boldsymbol{r_{fi}}|^2}{3\pi\epsilon_0 \hbar c^3} \tag{1.1}$$

where A is the rate of spontaneous emission or Einstein A coefficient, ω_0 is the frequency of the optical emission, and $|\boldsymbol{r_{fi}}|$ is proportional to the Hamiltonian matrix element

overlap between the final and initial states. Along with MCT and InAs/Ga(In)Sb, several other semiconductor materials have been employed for use in the infrared. Most obviously, bulk materials may be employed for infrared emitters and detectors. Such bulk compounds as InAs, GaSb [26], and InSb [27] have been used successfully as MWIR emitters and detectors. Significant work on quantum structures with cascaded active regions for infrared emission has been done by Yang and coworkers [28, 29, 30] as well as by Meyer [31]. Various tradeoffs exist between the competing material systems and growth techniques. In the remainder of this chapter some of the milestones of other researchers are highlighted.

1.3.1 Lancaster University

Infrared emitters based on InAs have been studied extensively by Krier and coworkers, who have produced some of the most powerful MWIR LEDs yet demonstrated. Liquid phase epitaxy (LPE) has been employed to produce crystals with high material quality as the crystal growth occurs in thermodynamic equilibrium. LPE is an attractive approach for producing bulk materials, alloys, and certain heterostructures, however this technique does not offer precise control over layer thickness and as such is not well suited to applications requiring thin layers. Krier *et al.* have demonstrated the production of high quality crystals by gettering with rare earth elements in LPE grown material [32]. Rare earth elements such as Yb and Gd are able to form compounds with impurities such as oxygen and carbon, but are not soluble in the LPE melt and are thus not incorporated into the crystal. The gettering effect has been reported to improve photoluminescence emission by factors of 10-100 by reducing the background carrier density and removing impurities [33]. It is believed that the reduction of impurities by this technique reduces SRH recombination, and the reduction of the background carrier density suppresses Auger recombination. Heterostructures based on InAsSbP/InAs and InAsSbP/InAsSb have been demonstrated as effective materials for MWIR emitters as well. Barrier layers

of InAsSbP are used to clad InAs or InAsSb active regions in order to improve carrier confinement in the active region and provide a near lattice-matched transition layer to the InAs substrate in the case of InAsSb active regions. Using this technique, output powers in excess of 3.5 mW have been reported for LEDs with an emission wavelength of 3.2 μm operated at room temperature. In this case, devices were 450×450 μm^2 in size and operated under pulsed excitation (1 kHz, 1 μs pulse width, 1.3 A peak current) and light collection aided with a parabolic reflector [34]. Using similar procedures, output power exceeding 2 mW was demonstrated at 3.8 μm (300 μm diameter mesa in a parabolic reflector, 200 Hz, 10 μs pulse width, 1.3 A peak current) [35] and 1 mW at 4.6 μm (300 μm diameter mesas, 1 kHz, 2 μs pulse width, 2 A peak current) [32].

1.3.2 Ioffe Institute

Substantial work on MWIR optical emitters has been done by researchers at the Ioffe Physico-Technical Institute [36]. Heterostructures based on the AlGaAsSb/GaInAsSb material system have been employed in high efficiency LED devices. Output powers as high as 3.2 mW were demonstrated by Danilova *et al.* [37] from a device emitting at 3.8 μm wavelength with anisotropically etched sidewalls in a parabolic reflector under pulsed operating conditions (0.5×0.5 mm^2 mesa with 0.1 mm etch depth, 1 kHz, 20 μs pulse width, 1 A peak current). Liquid phase epitaxy was employed to grow GaInAsSb active regions lattice matched to GaSb substrates and cladded by AlGaAsSb barrier layers for devices operating in the MWIR. A particularly interesting device fabrication method demonstrated at Ioffe employed a wet etching technique to fabricate angled sidewalls for mesa LEDs [38]. This technique allows better extraction of light from the device, as Fresnel reflections from the angled sidewalls direct a greater fraction of the photons towards the output surface at angles less than the critical angle for total internal reflection. The use of a near IR LED to optically excite a MWIR LED was also demonstrated at the Ioffe Institute [39, 40]. In this scheme a short wavelength, high efficiency

device operating at λ_1 was optically coupled by an intermediate layer to an active region designed to emit at a longer wavelength λ_2. Photons at wavelength λ_1 were absorbed in the subsequent active region, creating a carrier population which emitted light at λ_2. It was also proposed that additional active regions may be employed as needed, thus allowing added flexibility in frequency conversion of the emission of the overall device. Two color emission by the coupling of LPE grown active regions has been demonstrated in a device with emission wavelengths of 1.9 μm and 3.1 μm at 77 K [36]. Such a design presents possibilities for multispectral applications such as thermal imaging and spectroscopy.

1.3.3 Army Research Labs and Maxion Technologies

Interband quantum cascade (IQC) devices based on a multiple quantum well structure have been demonstrated as an effective material system for MWIR and LWIR LEDs [41, 42]. Interband cascade LEDs emitting at 3.8 μm have been shown to reach output powers in excess of 400 μW at room temperature with substrate thinning and surface texturing (100×100 μm^2 mesa) [41]. A principal advantage of the IQC structure is the step-like density of states associated with quantum wells, allowing the devices to operate more effectively at room temperature than a bulk or superlattice active region. Interband cascade devices have also been demonstrated in small format arrays [43] with apparent temperatures in excess of 1000 K for a 200×200 μm^2 mesa operating at 77 K.

CHAPTER 2
BACKGROUND

2.1 Crystallography and Solids

Materials in the solid state exist in either the crystalline or amorphous form; the former is structured as a periodic array of atoms and the latter lacks such spatial uniformity. Crystalline solids are of interest here, as the periodic and highly structured arrangement of atoms is what imparts the electronic and optical properties of semiconductors. Due to symmetry considerations in the lattice, there exist fourteen different crystal classes known as Bravais lattices in which the lattice appears identical from any one lattice site. Semiconductor crystals in the III-V family crystallize in the zincblende structure, which is itself not a Bravais lattice, but a face centered cubic (FCC) Bravais lattice with a two-atom basis. Here only binary semiconductors are treated mathematically, as the zincblende lattice with a two-atom basis lends easily to description. A lattice can be constructed mathematically by its lattice vectors, which allow construction of the lattice from any one lattice site due to symmetry. The lattice translation vector is described by

$$\mathbf{R} = n_1\vec{a_1} + n_2\vec{a_2} + n_3\vec{a_3} \tag{2.1}$$

where $\vec{a_i}$ are the vectors directed from one lattice site to another and n_i are integers. In the zincblende lattice the primitive set of vectors used to describe the lattice are

$$\vec{a_1} = \tfrac{a}{2}\hat{y} + \tfrac{a}{2}\hat{z} \tag{2.2}$$

$$\vec{a_2} = \tfrac{a}{2}\hat{x} + \tfrac{a}{2}\hat{z} \tag{2.3}$$

$$\vec{a_3} = \tfrac{a}{2}\hat{x} + \tfrac{a}{2}\hat{y}, \tag{2.4}$$

where a is the lattice constant; this set of vectors describes a FCC lattice. Such an arrangement of atoms is depicted by the dark spheres of the zincblende structure in Figure 2.1(a). The basis vector is then given by

$$\vec{b_1} = \frac{a}{4}\hat{x} + \frac{a}{4}\hat{y} + \frac{a}{4}\hat{z}, \tag{2.5}$$

which describes the positions of the light colored spheres in Figure 2.1(a). Bonding in a III-V compound is shown in Figure 2.1(b) with the (110) direction normal to the page. Visualization of the bonding arrangement becomes especially useful when considering the interfaces between different compounds in an epitaxially grown layer structure.

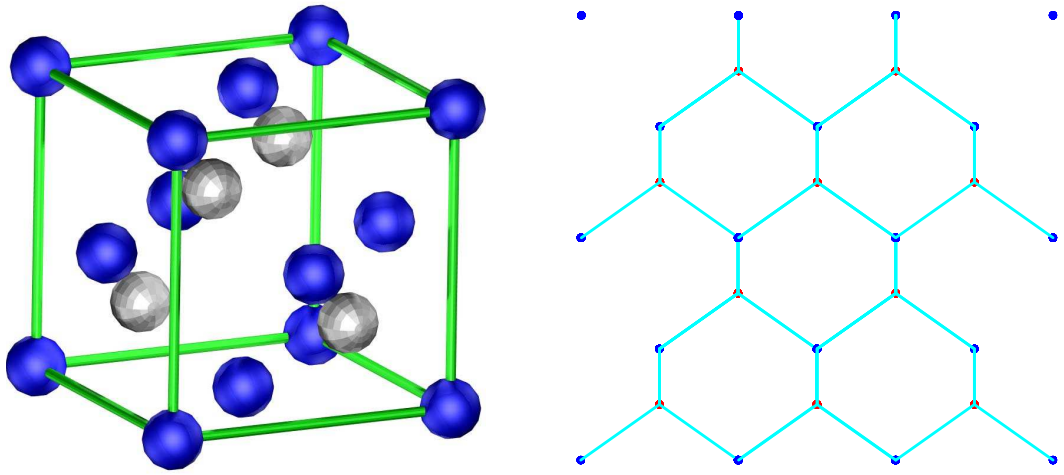

(a) (b)

Figure 2.1: (a) A unit cell of the zincblende lattice. (b) Bonding between group V and III atoms in the zincblende lattice; the (110) direction is facing into the page.

2.2 Band Structure

Of the three phases in which matter exists, the solid state is the only one which exhibits long range structural order. In the gaseous state where interatomic distances are large, electron energy levels are quantized as in the case of a single atom. The simplest example of this behavior is the hydrogen atom, where energy levels are determined by the principal quantum number n and have the values

$$E_n = -\frac{13.6\ eV}{n^2}, \tag{2.6}$$

neglecting higher order perturbation correction terms. However, if a second identical atom is introduced to the system, the energy levels of the two-atom system will split. This owes to the creation of bonding and anti-bonding molecular orbitals from interaction of the Coulomb well potentials of the atoms. Extrapolating to a macroscopic size crystal where the number of atoms is on the order of 10^{23} cm^{-3} and can be considered infinite, energy level splitting produces bands of allowed energy values. Charge carrier energies are no longer strictly quantized, and are free to assume an energy value within a given range of energies dictated by the band structure. Carriers, however, cannot occupy energy levels between the bands as there are no states available; these regions are referred to as forbidden gaps or band gaps.

2.2.1 Charge Carrier Behavior in the Lattice

Description of the energy bands requires consideration of the quantum mechanical nature of charge carriers. A carrier in a lattice can be viewed as a wave which obeys the Schrödinger equation, which in its general form is given by

$$\imath\hbar\frac{\partial}{\partial t}\psi(\mathbf{r},t) = \left[-\frac{\hbar^2}{2m}\nabla^2 + V(\mathbf{r})\right]\psi(\mathbf{r},t), \tag{2.7}$$

where $\hbar$ is Planck's constant divided by 2π, $\psi(\mathbf{r},t)$ is the wave function, and $V(\mathbf{r})$ is the potential acting on the electron. In a crystal lattice, $V(\mathbf{r})$ is periodic with the lattice spacing and gives rise to the band structure of the material. Assuming the time dependence of the Schrödinger equation to be of the form $e^{\imath Et/\hbar}$, the equation may be rewritten as

$$\left[-\frac{\hbar^2}{2m}\nabla^2 + V(\mathbf{r})\right]\psi(\mathbf{r}) = E\psi(\mathbf{r}) \tag{2.8}$$

which describes only the spatial character of the wavefunction and is referred to as the time independent Schrödinger equation (TISE). The crystal potential $V(\mathbf{r})$ determines the nature of electron behavior in the solid, and dictates that the wavefunction of the electron be periodic with the lattice. The solution to the TISE with a periodic potential is a plane wave solution, thus the electron behaves as a plane wave which is not localized around any particular lattice site. Specifically, this is the Bloch function solution and is described by the equation

$$\psi_k(\mathbf{r}) = e^{\imath\mathbf{k}\cdot\mathbf{r}}u_k(\mathbf{r}) \tag{2.9}$$

where $u_k(\mathbf{r})$ is the Bloch eigenfunction which is periodic with the lattice, that is $u_k(\mathbf{r}) = u_k(\mathbf{r}+\mathbf{R})$, and $\mathbf{R}$ is the lattice vector given in Equation 2.4. Solving for $u_k(\mathbf{r})$ in the TISE with the constraint of lattice symmetry gives the energy bands (or dispersion relations) of the solid as a function of $\mathbf{k}$.

The effect of the crystal potential perturbation on the behavior of carriers can be described by the so-called effective mass. A nonrelativistic free carrier propagating through space which experiences no perturbation simply has the rest mass of an electron, $m = m_e$ which is approximately 9.1×10^{-31} kg. Carrier transport in a crystal leads to a situation where the perturbation of the crystal potential modifies the behavior of the

carrier from that of a free particle. An electron in the free electron model obeys the relation

$$E(k) = \frac{\hbar^2 k^2}{2m_e} \tag{2.10}$$

which is parabolic in k-space. Real energy bands, however, are not necessarily parabolic, but may be assumed parabolic near zone center provided that the carrier mass is modified accordingly. If the carrier mass is taken as

$$m^* = \frac{\hbar^2}{\frac{\partial^2 E_n}{\partial k^2}} \tag{2.11}$$

the simple parabolic dispersion relation may be employed and the carriers behave as with the free carrier model. This formalism essentially takes the complicated interaction of carriers with the crystal potential and simplifies it to the parabolic-band model. Given the inverse relationship of the effective mass to the dispersion curves, one can easily see that narrow bands with large second derivatives yield light effective masses. In the case of InAs, for example, the effective mass in the conduction band is only 0.023 m_e. On the other hand, materials with large energy gaps where energy level repulsion is low, yielding broad bands, give rise to large effective masses. For instance gallium nitride (GaN), a wide gap semiconductor, exhibits an electron effective mass of 0.20 m_e.

2.2.2 Reciprocal Lattice and Symmetry

In Section 2.1 the spatial representation of a crystal lattice, which is useful for visualizing the physical lattice and its bonding geometry, was described. Here the reciprocal lattice is introduced to aid the description of the electronic structure of a material. The reciprocal lattice allows one to work more easily in terms of crystal momentum, as the electron momentum is given by $\mathbf{p} = \hbar\mathbf{k}$, and the wavevector $\mathbf{k}$ has units of $\frac{1}{length}$,

given in scalar form as $k = 2\pi/\lambda$. Construction of the reciprocal lattice stems from a Fourier analysis of the lattice. Taking some periodic function with periodicity of the lattice, $f(\mathbf{r})$, and applying the Fourier transform yields

$$f(\mathbf{k}) = \int f(\mathbf{r}) e^{-\imath \mathbf{k}\cdot\mathbf{r}} d^3\mathbf{r}. \tag{2.12}$$

Performing the same calculation at any other point in the lattice $\mathbf{r} + \mathbf{R}$ is equivalent, and can be written as

$$f(\mathbf{k}) = \int f(\mathbf{r}) e^{-\imath \mathbf{k}\cdot(\mathbf{r}+\mathbf{R})} d^3\mathbf{r}. \tag{2.13}$$

The functions will be equivalent only if $e^{\imath \mathbf{k}\cdot\mathbf{R}} = 1$, implying that the condition $\mathbf{k}\cdot\mathbf{R} = 2\pi n$ holds. Following from this, the reciprocal lattice vector, denoted by $\mathbf{G}$ is given by

$$\mathbf{G} = n_1 \vec{a^*}_1 + n_2 \vec{a^*}_2 + n_3 \vec{a^*}_3 \tag{2.14}$$

and the $\vec{a^*}_i$ are of the form

$$\vec{a_1^*} = \frac{2\pi}{V_c} (\vec{a}_2 \times \vec{a}_3) \tag{2.15}$$

$$\vec{a_2^*} = \frac{2\pi}{V_c} (\vec{a}_3 \times \vec{a}_1) \tag{2.16}$$

$$\vec{a_3^*} = \frac{2\pi}{V_c} (\vec{a}_1 \times \vec{a}_2) \tag{2.17}$$

where V_c is the unit cell volume. From the reciprocal lattice vectors, the Brillouin zones of the lattice can be constructed. Brillouin zones (BZs) are unit cells of the reciprocal lattice, and are formed by bisecting the reciprocal lattice vectors with planes normal to the vectors. The first BZ is formed by bisecting the reciprocal lattice vectors at their

midpoints, this zone contains all information about the wavefunction due to periodicity. As the reciprocal lattice of a FCC lattice is a body-centered cubic (BCC) lattice, the first BZ for the FCC lattice is formed by bisecting the lattice vectors of a BCC lattice at their midpoints. From symmetry considerations in the BZ, it follows that the energy bands $E_n(\mathbf{k})$ have mirror symmetry, are periodic with the reciprocal lattice, and have the rotational symmetry of the real-space lattice [44].

Although the number of bands is essentially infinite, only the bands nearest the Fermi level (E_F) are typically of interest. The energy level at which the probability of electron occupation at thermal equilibrium is $\frac{1}{2}$ is defined as the Fermi level, and for intrinsic material, this is typically near the middle of the energy gap. The four most important bulk bands in studying optical and electronic properties of semiconductors are the conduction, heavy hole (HH), light hole (LH), and split-off (SO) bands. Typically the HH and LH bands are degenerate at $\mathbf{k} = 0$, and the separation between these bands and the conduction band determine the energy gap of the material as seen in Figure 2.2. In this figure, the bands represent a direct gap semiconductor, in which the conduction band minimum E_c and valence band maximum E_v both lie at zone center. Indirect gap semiconductors present a situation where E_c and E_v are displaced in k-space, thus requiring not only a transfer of energy, but a transfer of momentum for carrier transport across the band gap. To first order, the magnitude of the energy gap determines a materials ability to conduct. Metals have no energy gap, and are thus very conductive, while insulators have an energy gap of several electron volts, making conduction difficult as the valence band is completely full and a large amount of energy is required to excite an electron to the conduction band. Semiconductors, with energy gaps typically ≤ 2 eV, present a more interesting case, which will be examined further in the following.

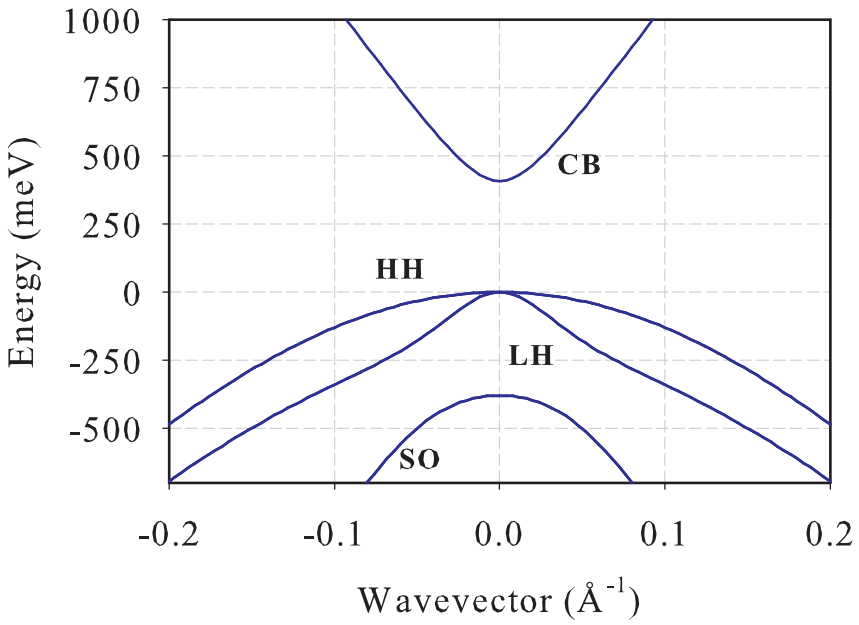

Figure 2.2: Band structure of InAs at 77 K, showing the four energy bands most commonly considered in studies of optical and electronic properties of semiconductors.

2.2.3 Density of States

Optical and electronic properties of semiconductors depend heavily on the distribution of carriers in the bands near zone center. Calculation of the carrier distributions requires knowledge of the density of available electronic states in the relevant regions of the bands. The density of states is the number of electronic states per unit volume in a material for a given energy value. In a bulk semiconductor, the density of states $g(E)$ is expressed

$$g(E) = \frac{1}{2\pi^2}\left(\frac{2m^*}{\hbar^2}\right)^{3/2}\sqrt{E} \tag{2.18}$$

where E is the energy. As $g(E) \propto \sqrt{E}$, the density of states increases with a square law characteristic in energy. For a two-dimensional system such as a quantum well, the density of states becomes step-like and is given by

$$g(E) = \frac{m^*}{\pi\hbar^2} \sum \phi(E - E_i) \tag{2.19}$$

and ϕ is the Heaviside step function. Employing such a 2-D structure may offer benefits to device performance, as the density of states increases sharply, thus providing a potentially large number of states near the band edges.

2.3 Charge Carriers

2.3.1 Carrier Concentration

Semiconductor devices typically rely on the transfer of charge carriers through the device and the interaction of those carriers with other charge carriers, the lattice, and impurities to produce the desired device characteristics. More exotic semiconductor devices exist in which device operation is based on the transfer of spin angular momentum, however such devices are by and large in their infancy and will not concern the present discussion.

In order to calculate the carrier concentration, the density of states and carrier distribution function must be known. The distribution function follows Fermi-Dirac statistics and is given by

$$f(E) = \frac{1}{1 + e^{(E-E_F)/k_B T}} \tag{2.20}$$

where E_F is the Fermi energy and k_B is Boltzman's constant [45]. For intrinsic semiconductors (those with few impurities), E_F is typically near the center of the energy gap, however this is modified when the material is doped with impurities. Doping with donors (atomic species which contribute free electrons to the material) moves E_F closer to the conduction band. Similarly, doping with acceptors (species which contribute holes) moves E_F towards the valence band. Typically, the intrinsic Fermi level near the

center of the energy gap is labeled E_i for clarity. Calculation of the electron concentration can be performed by integrating the product of the density of states and Fermi functions over the region in energy where conduction electrons may exist;

$$n = \int_0^{E_{max}} g(E)f(E)dE \tag{2.21}$$

and E_{max} is the highest level in the conduction band that is considered. The concentration of holes p, or empty electron states, can be calculated in a similar fashion by integrating over energies occupied by the valence band.

2.3.2 Generation and Recombination

Of upmost importance in optoelectronic devices is the manner in which charge carriers interact with themselves, the lattice, defects, and external perturbations. At typical device operating temperatures, thermally excited electrons occupy states in the conduction band at some equilibrium concentration. Disruption of the equilibrium population by carrier injection from, e.g., electrical or optical excitation will evolve towards equilibrium by carrier recombination processes. The three recombination processes of interest are Shockley-Read-Hall (SRH), radiative, and Auger recombination. Optoelectronic devices rely on radiative transitions to produce optical output, however SRH and Auger recombination are nonradiative processes which degrade device performance by providing alternative routes for carriers to equilibrate. These recombination mechanisms should be suppressed using optimized growth techniques and band structure engineering when possible.

Recombination via the SRH mechanism occurs when a carrier is trapped by an impurity or defect in the crystal structure. The change in carrier density due to SRH recombination is proportional to the carrier density N as the process involves a single carrier at a time. Defect mediated recombination, in an over-simplified form, can be

expressed in terms of the SRH coefficient:

$$A = N_t \sigma v_{th}, \tag{2.22}$$

where N_t is the density of trap states, σ is the capture cross section, and v_{th} is the thermal velocity [46, 47]. Also of interest in single carrier trap assisted recombination is surface recombination. Dangling bonds at the surface or layer interface of the semiconductor act as traps, which further exacerbates nonradiative recombination. The effects of surface recombination are typically expressed in terms of the surface recombination velocity S:

$$S = N_s \sigma_p v_{th}, \tag{2.23}$$

where N_s is density of active centers at the surface, v_{th} is the thermal velocity, and σ_p is the capture cross section [45]. SRH recombination is intrinsic to the material quality of the device, and cannot by minimized by creative engineering of the device. Material quality can be improved by optimizing growth conditions to reduce interface roughness, strain, and impurity concentration. The SRH lifetime thus gives a useful measure of material quality, and can be used to gauge material optimization.

Radiative recombination occurs when an electron enters a lower energy state and the energy loss mechanism is the release of a photon. Two types of radiative recombination are typically considered in semiconductor devices: interband transitions whereby an electron in the conduction band recombines with a hole in the valence band [Figure 2.3(a)], and intersubband transitions [Figure 2.3(b)] which are of interest in quantum well structures [28]. Both radiative recombination mechanisms find applications in various infrared emitter systems. These spontaneous emission processes generate the optical output of optoelectronic devices such as LEDs. As radiative recombination requires two carriers, the radiative rate scales as N^2.

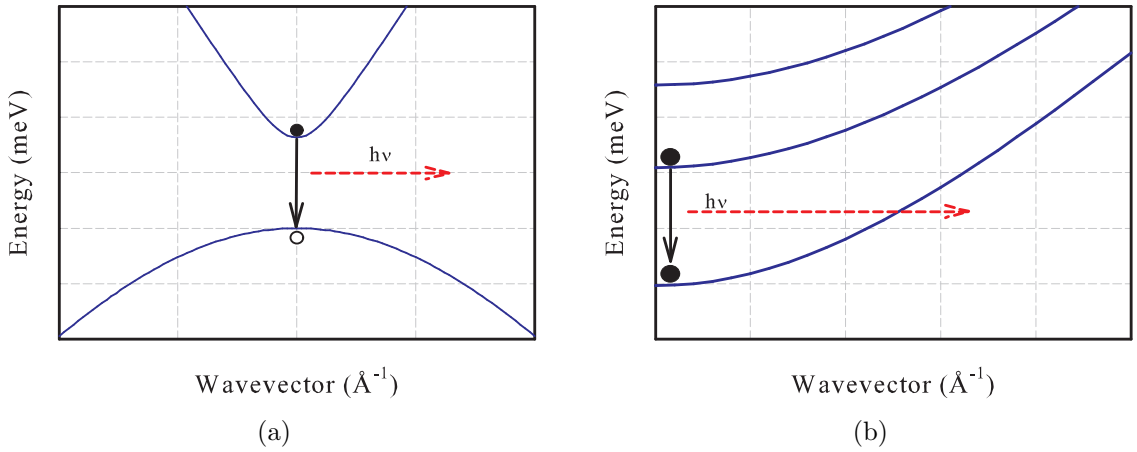

Figure 2.3: Radiative transitions in semiconductor devices. (a) Band-to-band (or interband) transitions, and (b) conduction subband (intersubband) transitions shown between quantum well subbands.

Auger scattering is a process which occurs when two carriers recombine, transferring energy and momentum to a third carrier. In the simplest picture, Auger recombination is a three carrier process and scales as N^3. Auger processes are especially important at high carrier densities due to this scaling, and often pose a limit to device performance. The third carrier which is excited to a higher energy state relaxes to equilibrium by phonon emission, which further increases the local temperature of the device and aggravates nonradiative recombination. Auger processes can be classified as either band-to-band, trap-assisted, or phonon-assisted, depending on how energy and momentum transfer occurs.

Combining the contributions from the three recombination processes, the overall volumetric recombination rate can be expressed as:

$$R = AN + BN^2 + CN^3 = -\frac{dN}{dt} \tag{2.24}$$

where B is the radiative coefficient and C is the Auger coefficient; units are cm^{-3}/s [48].

2.4 Semiconductor Junctions

By and large, the interesting phenomena in heterostructure devices occur at the interfaces. Electronic and optical properties of semiconductor devices are determined in large part by the manner in which the energy bands line up at the interfaces between different materials. This line up is determined by the materials at the junction, and the doping characteristics of the materials. Interface charges and material gradients also play a significant role in heterostructure interfaces, as does the deposition technique used to grow the materials. The properties and behavior of semiconductor devices due to semiconductor-semiconductor and semiconductor-metal junctions are briefly examined in the following.

2.4.1 Semiconductor-Semiconductor Junctions

Junctions between two regions of a semiconductor can differ in material composition, doping profile, or both. Both of these parameters determine how the energy bands of the two regions line up with respect to each other and the rest of the device, and thus how the device will behave in equilibrium and under external bias. The band alignment for a simple p-n homojunction is shown in Figure 2.4, where band bending that leads to the internal field is shown.

When two bulk semiconductor materials are placed in atomic contact, the Fermi levels of the separate materials at equilibrium must align such that the Fermi level of the system is constant. First the case of the homojunction is treated, whereby the two materials are of the same composition, but have different doping levels as in the case of the p-n junction. Due to the initially high number of electrons in the n-region and holes in the p-region, diffusion occurs to reduce the concentration gradients. The diffusion of electrons into the p-region leaves positive ions behind in the n-region, and similarly hole diffusion leaves negative ions in the p-region. A space charge field is thus established at the junction, which acts to prevent further carrier diffusion in equilibrium and is given

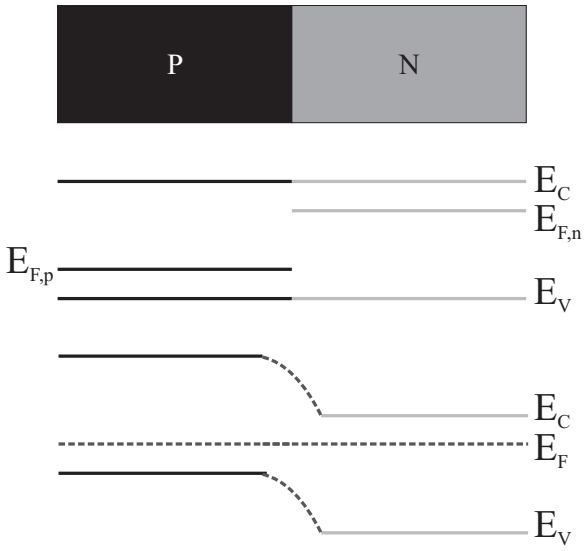

Figure 2.4: Diagram of a p-n homojunction shown before (top) and after (bottom) the materials are brought into contact.

by

$$\Phi_j = \frac{k_B T}{q_E} \ln\left(\frac{N_A N_D}{n_i^2}\right) \tag{2.25}$$

where N_A and N_D are the donor and acceptor doping densities. The region where electrons and holes are depleted and the space-charge field develops is called the depletion region; here it is assumed that $n = p = 0$. Knowledge of the width of the depletion region is required to determine such characteristics as device capacitance and is given as

$$W = \sqrt{\frac{2\varepsilon_s}{q_e}\left(\frac{N_A + N_D}{N_A N_D}\right)\Phi_j} \tag{2.26}$$

where ε_s is the dielectric constant. In contrast, for a p-i-n structure, the width of the depletion region is dictated by the width of the intrinsic material. The junction capacitance can thus be calculated as

$$C_j = \frac{\varepsilon_s A_j}{W} \tag{2.27}$$

where A_j is the junction area. This capacitance term constrains the operating speed of the diode. Of consequence in forward biased devices is the diffusion capacitance which arises due to minority carrier diffusion in the neutral material. This is given as

$$C_d = \frac{A q_e^2 L_p p_n}{k_B T} e^{\frac{qV}{k_B T}}, \tag{2.28}$$

where L_p is the hole diffusion length and p_n is the equilibrium hole density in the n-type material.

While commercial diodes fabricated from bulk materials may exhibit nearly ideal device characteristics, the infrared diodes considered here, which were fabricated from antimonide based materials, do not have such ideal diode characteristics (i.e. the I-V characteristic shows comparatively soft rectification behavior). The Schockley diode equation is written

$$I = I_0 \left(e^{q_e V / n k_B T} - 1 \right) \tag{2.29}$$

where n is the diode ideality factor for which an ideal diode has $n = 1$. The ideality factor can then be determined by taking the natural log of both sides and rearranging to give

$$n = \frac{q_e}{k_B T} \frac{V}{\ln I - \ln I_0}, \tag{2.30}$$

which is often a useful reference that can be fit to a diode I-V characteristic curve to allow comparison between devices [49].

Heterojunctions exist when two materials of different composition are placed in

atomic contact. This type of junction is employed extensively in this work, as alternating layers of V/III materials comprise the entire device. Again in these structures, the bands must align such that the Fermi levels at equilibrium are constant throughout the device as seen in Figure 2.5. As the band alignments in heterostructures may have significant offsets, band bending at the interfaces may cause potential spikes to form. This situation may present barriers which carriers must tunnel through to traverse the device, thus increasing device resistance and possibly causing unexpected behavior if ignored.

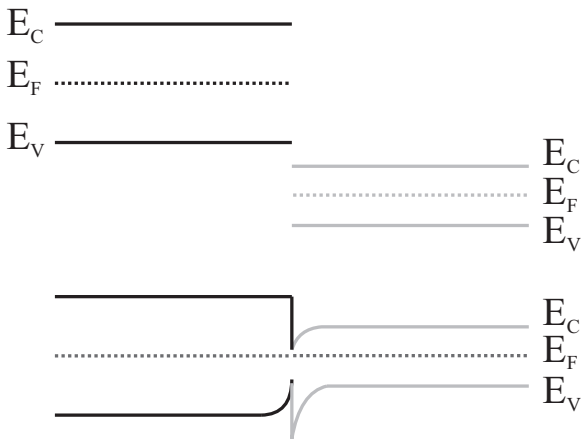

Figure 2.5: Representation of a heterojunction in which the band alignment causes interfacial potential spikes.

2.4.2 Semiconductor-Metal Junctions

Interfaces between semiconductor and metal layers form electrical junctions which exhibit behavior that is either Schottky (rectifying) or Ohmic in nature. Schottky contacts are characterized by the high barrier that forms at the metal-semiconductor junction. As in the case of semiconductor-semiconductor junctions, the Fermi levels of the metal and semiconductor must align. Thus if a large difference exists between the Fermi levels causing significant potential spikes at the interface, a Schottky contact is formed. In order to traverse the device carriers must overcome the potential either by tunneling through it, or via thermionic emission by thermal energy. The thermionic emission

process is described by

$$J = A^* T^2 e^{-q_e \phi / k_B T} \left(e^{q_e V / k_B T} \right) \tag{2.31}$$

where A^* is the Richardson constant, ϕ is the barrier height, and V is the bias across the junction. Values of the Richardson constant are given in Table 2.1 which are calculated by the equation

$$A^* = \frac{q_e m^* k_B^2}{2\pi^2 \hbar^2} \tag{2.32}$$

or determined experimentally and given with corresponding references [50].

Material	A^* (A/cm^2·K^2)	Reference
n-GaAs	8	[45]
p-GaAs	74	[45]
n-GaSb	5.1	[51]
p-GaSb	48	

Table 2.1: Richardson constants.

Generally in LED devices, it is desirable to avoid Schottky barriers, and Ohmic contacts are preferred. This type of contact exhibits a low contact resistance, which is ideally less than the series resistance of the LED. Low contact resistance helps keep device heating to a minimum by reducing the voltage drop across the device. In the case of highly doped semiconductor material, the contact resistance goes as

$$R_c \propto \exp\left(\frac{4\sqrt{m^* \varepsilon_s}\phi}{\hbar \sqrt{N_D}} \right). \tag{2.33}$$

2.5 Light Emitting Diodes

Photonic devices which can be designed to emit over a large range of wavelengths can be fabricated by simple p-n junctions or by placing an active region between the p and n regions of a diode, forming a p-i-n junction. In such a device, the depletion region is essentially governed by the width of the intrinsic region, thus recombination may occur throughout the intrinsic region. Simple p-n homojunction LEDs can be fabricated from bulk materials, and the operating wavelength is dictated by the energy gap of the bulk material. Alternatively in p-i-n heterostructures the emission spectrum is determined by the intrinsic region, which is of differing material composition than the cladding p and n regions. In this work the intrinsic region was composed of InAs/GaSb superlattice material, allowing for a widely adjustable emission wavelength.

2.5.1 Power Limitations

Due to the high index of refraction of semiconductor materials, $n = 3.8$ for GaSb, extraction of light from devices presents difficulties. Light rays incident on the semiconductor/air interface must propagate with small angles to the surface normal so as to not be totally internally reflected. In GaSb based devices, the critical angle for total internal reflection (TIR) is only 15.3°. Calculation of the solid angle of emission by $2\pi(1 - \cos\theta)$, where θ is the half angle, yields a solid angle of 0.22 sr, the solid angle subtended by a sphere being 4π sr. Assuming that the LED active region emits isotropically, the collected upper hemisphere emission of a LED is limited to about 1.8% of the total emission. This calculation assumes that no reflective surfaces are present to assist light extraction, or extraneous optics used to increase output. Further reducing the useful output power is the Fresnel reflection occurring at the semiconductor/air interface which in GaSb is calculated to be $R = 34\%$, reducing the useful emission to ∼1.2% of the optical power generated in the active region.

Several schemes exist to help overcome some of the aforementioned limitations to

output power, however the wallplug (power) efficiency of LEDs generally remains low. Antireflection coatings may be applied to the LED surface to help reduce the Fresnel reflection, however improvement from this technique is limited to about 30%. Another scheme involves chemical etching of deep trenches with angled sidewalls around mesa diodes. This technique, shown in Figure 2.6(b), directs more light towards the output

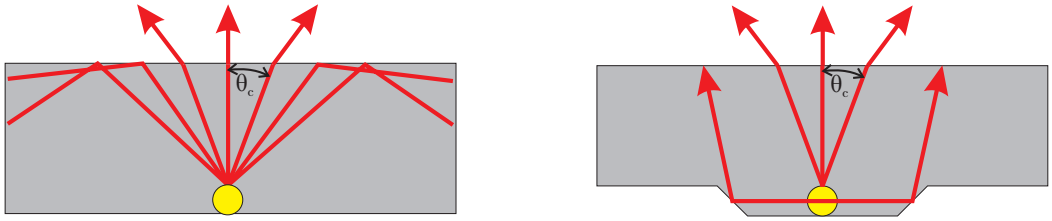

(a) (b)

Figure 2.6: (a) Geometrical limitations on light extraction from a LED due to total internal reflection. (b) Angled facets improve light extraction by directing more photons toward the surface normal at angles less than the critical angle.

surface by Fresnel reflection from the facets [38]. In the case of LEDs which emit through the substrate, the metal contact on the active region side of the wafer may be made large in order to act as a reflector and redirect light to the output surface. Other techniques such as substrate thinning to reduce absorption and etching gratings on the output surface have also been demonstrated to enhance light extraction.

2.6 Thermal Imaging

2.6.1 Black Body Radiation

Thermal radiation is emitted by all objects in the form of a broad band spectrum, the spectral characteristics of which depend on the temperature of the object and the physical properties of the emitting surface. By definition, an object which absorbs all radiation incident on it is considered a black body. The closest physical approximation to a true black body is a cavity with absorbing walls and an aperture on one wall

to allow the transfer of radiation into and out of the cavity. Planck was the first to correctly describe the spectrum of the radiation emanating from a black body source; this distribution is known as the Planck distribution and gives the spectral radiance

$$I(\lambda, T) = \frac{2hc^2}{\lambda^5} \frac{1}{e^{\frac{hc}{\lambda k_B T}} - 1}, \tag{2.34}$$

where λ is the wavelength, T is the temperature in kelvin, h is Planck's constant, c is the speed of light, and k_B is Boltzmann's constant. This spectral radiance is given in units of $\mathrm{W{\cdot}cm^{-2}{\cdot}sr^{-1} \cdot \mu m^{-1}}$. Spectra of black bodies operating at 1000 K and 700 K are shown in Figure 2.7, indicating the dependence of both intensity and peak emission wavelength on temperature. Wein's displacement law, which is given by

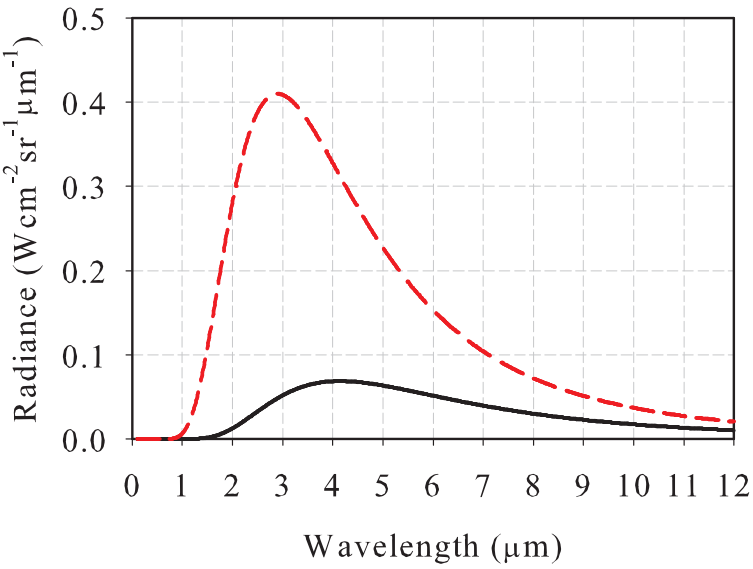

Figure 2.7: Spectra of black body radiation at 1000 K (dashed curve) and 700 K (solid curve).

$$2.898 \times 10^3 \ \mu m \cdot K = T \times \lambda_{peak}, \tag{2.35}$$

may be used to calculate the peak emission wavelength. Real objects, however, behave as grey bodies, and have an associated emissivity value. The emissivity describes the fraction of the radiation emitted by the object to the radiation emitted by a true black body at the same temperature. Non-ideal emitters of thermal radiation (i.e. those with emissivity $\varepsilon < 1.0$) are often assumed to have a constant emissivity despite dependencies on wavelength and emission angle.

2.6.2 Apparent Temperature

Many technologies rely upon the detection of infrared radiation to gather information about the surrounding environment. A particularly significant application of IR detection is imaging, whereby a suitable detector array captures the radiation emitted from a scene within a given spectral range. Observation of a scene with an appropriate IR detector may give information not only about the physical nature of the scene, but also about the thermal characteristics. Objects may then be identified and tracked in a scene by the thermal signature that emanates from the object due to its temperature, emissivity, and physical characteristics. One may then speak of the apparent temperature of an object in a thermal scene, or the temperature of an object as perceived by the detector.

Calibration of IR detector arrays for thermal imaging may be carried out either by observing a live scene with the detector, or simulating the thermal scene with an array of IR emitter elements much as a television screen simulates a scene with visible light. Direct observation of a thermal scene for calibration is not always a viable option, as this may require the expenditure of costly resources. Such is the case in many military applications, where the simulation of interactions involving munitions may be prohibitively expensive and dangerous. To this end, it is advantageous to simulate thermal scenes with appropriate IR emitters.

In order to use an optoelectronic device such as a LED for simulating an object

at a given temperature, the device must generate enough optical output within the spectral band observed by the detector to equal the output of a black body at that temperature. By integrating the Planck distribution over the spectral window of interest and multiplying by the area of the optical emitter, the requisite axial power to simulate an object at a given temperature may be calculated:

$$\int_{\lambda_{low}}^{\lambda_{high}} I(\lambda, T) d\lambda = \frac{P_{axial}}{A}. \tag{2.36}$$

For operation in the MWIR, a typical detector material is InSb, for which a suitable spectral window is 3-5 μm. Using these values, the power necessary to simulate an object at 2000 K with a 120×120 μm^2 emitter is 0.73 mW/sr. This requirement is shown in Figure 2.8, where the integrated intensity of the LED spectrum matches the intensity of the black body spectrum integrated from 3-5 μm. Performing the calculation

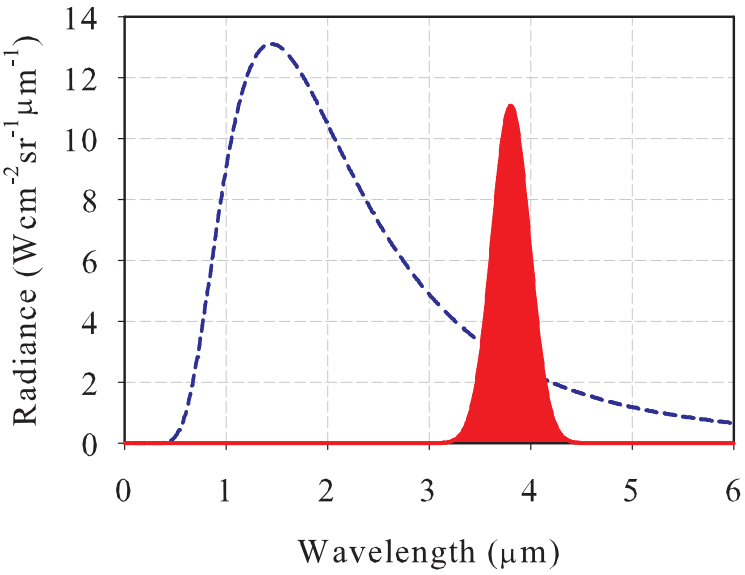

Figure 2.8: Black body spectrum for an object at 2000 K (dashed curve), and the requisite radiance of an LED emitting at 3.8 μm (solid curve) which is shown as a Gaussian distribution.

for apparent temperature over a range of device output powers while holding constant the emitter area and window of detection yields the result shown in Figure 2.9. The dependence of apparent temperature on optical emission exhibits power-law-like behavior, becoming nearly linear over a wide range of power values.

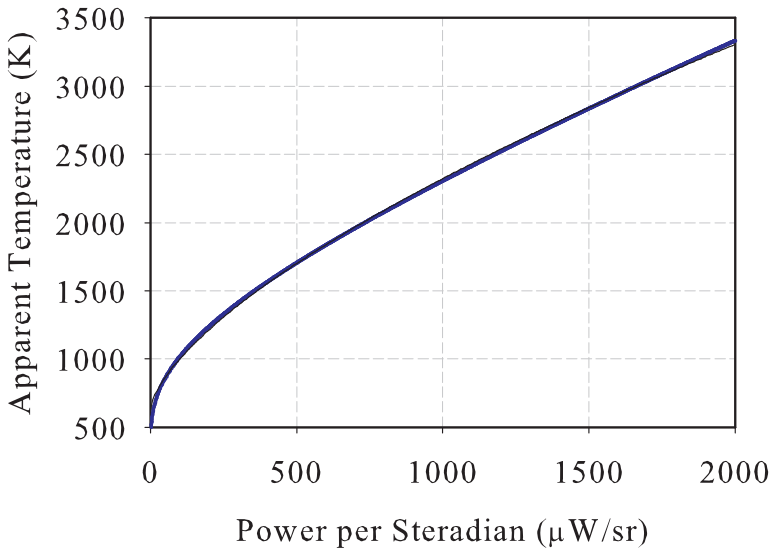

Figure 2.9: Dependence of apparent temperature on device output power for a given emitter pitch. The spectral window was taken to be 3-5 μm, and the entire LED spectrum assumed to fall within this window. The pitch of the emitter was held constant at 120 μm.

2.6.3 Array Considerations

Fabrication of LED devices into arrays for scene generation involves further considerations to the apparent temperature calculation in order to accurately model the thermal characteristics of the array. The parameters which describe the physical characteristics of an emitter array are the pitch, fill factor, and resolution. Pitch is simply the length of an entire pixel cell, or the overall length of the array divided by the number of pixels. The fraction of surface area on the array occupied by actual emitting material a describes the fill factor,

$$ff = \frac{A_{mesa}}{A_{pixel}}, \tag{2.37}$$

where A_{mesa} is the emitter area and A_{pixel} is the area of the entire pixel (pitch squared). In order for the scene emitted by the array to appear as a contiguous thermal image, the entire pixel area must be assumed to emit, despite the smaller size of the actual emitter. Dependencies of apparent temperature on output power and fill factor are illustrated in Figure 2.10, where the effect of fill factor can be seen by choosing a reference point, and moving toward a higher value of pitch.

Devices emitting in the LWIR are also of interest. Suitable cameras such as HgCdTe-based and quantum well infrared photodetectors are available, with detection bands extending well past 12 μm. Here, emitters are expected to be paired with detectors operating in the 8-12 μm range, and as such this interval was incorporated into the apparent temperature calculation. Figure 2.11 shows the effect of device size and output power on apparent temperature. From the figure it is apparent that much lower output powers are necessary to simulate a given apparent temperature in the LWIR; this is due to the decreased intensity of the black body spectrum for a given temperature at longer wavelengths. Although the requisite output powers are lower than for the MWIR case, LWIR emitters are typically much less efficient than MWIR emitters.

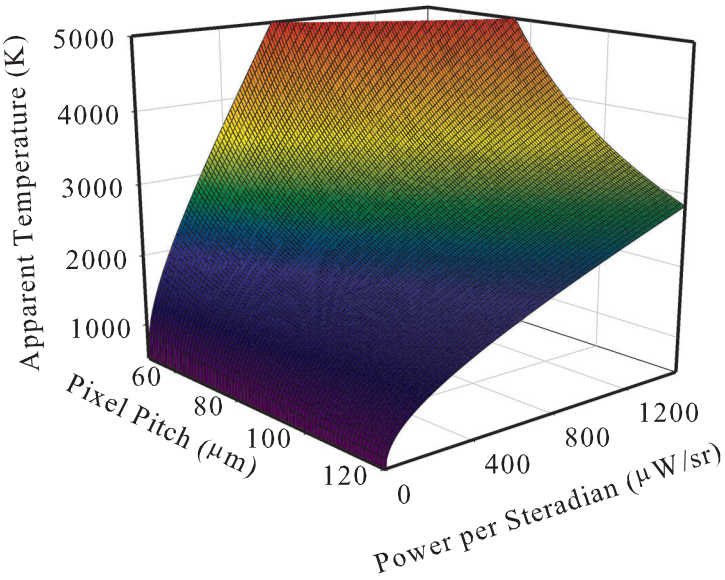

Figure 2.10: Plot of the dependence of apparent temperature on both LED power output and device size for MWIR emitters operating in the 3-5 μm band. Clearly, small devices with high output powers are most suitable for simulating hot objects.

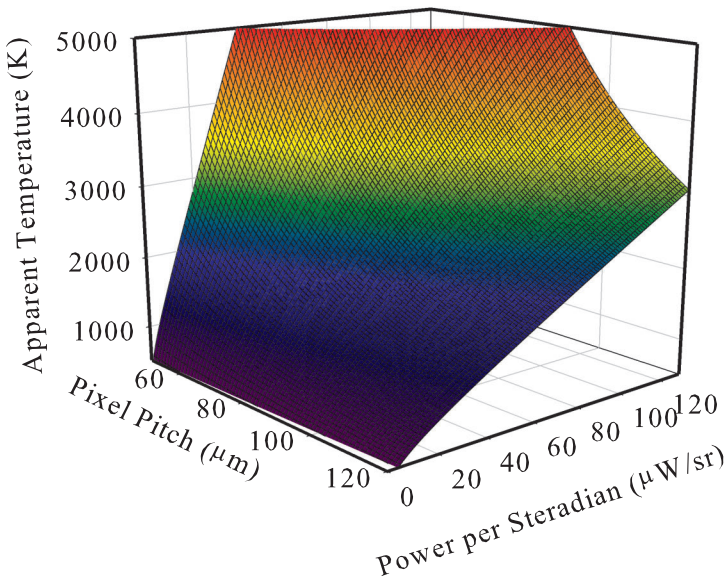

Figure 2.11: Plot of the dependence of apparent temperature on both LED power output and device size for LWIR emitters. In this calculation, the entire emission spectrum of the LED was assumed to lie within the 8-12 μm band.

CHAPTER 3
FUNDAMENTALS OF MOLECULAR BEAM EPITAXY

Superlattices are synthetic semiconductor crystals composed of layers of alternating material or doping concentration, with the layer thickness being shorter than the electron de Broglie wavelength to impose conditions of quantum confinement [22]. Producing abrupt alternating layers of semiconductor materials requires precision deposition techniques, capable of quickly changing material composition and/or doping concentration. Epitaxial deposition systems such as metal organic vapor phase epitaxy and molecular beam epitaxy are well suited to this task. The following discusses the rudiments of MBE deposition as applicable to superlattice growth.

In order to obtain the high precision layers required for InAs/GaSb superlattices, MBE is the growth technique of choice. A typical MBE reactor consists of several effusion cells containing high purity materials with corresponding mechanical shutters, directed at a heated substrate in an ultrahigh vacuum (UHV) environment. Deposition is controlled by evaporating selected materials at an appropriate temperature, and actuating the mechanical shutters to commence or halt growth of a given material.

The ultrahigh vacuum environment allows the atoms and molecules emerging from the effusion cells to propagate with a very large mean free path, and travel nearly unimpeded to the substrate. Central to the operation of the system is extensive shielding of the substrate from impurities by cryogenic panels, whereby shrouds surrounding the substrate are cooled to cryogenic temperatures by a continuous flow of liquid nitrogen (LN_2). Cryo panels serve as a pumping mechanism by trapping stray gas molecules, thereby minimizing contamination to the substrate manipulator area.

Semiconductor crystal growth by MBE presents the grower with a large array of variables that can be adjusted to optimize growth of a particular material. The grower

must choose not only appropriate parameters for material deposition, but also pre-treatment of the substrate. Wafers can be ordered in a wide variety of configurations as well, with variations in cut, doping, and resistivity to name a few. A principal goal of this work was to optimize various growth parameters and techniques with the intent of optimizing the optical, electronic, and structural properties of superlattice-based devices. Correlations between the various properties will be made in order to provide added insight into design tradeoffs.

3.1 MBE System

The MBE growth process is made possible by careful design and layout of the UHV growth chamber and associated processing chambers. A typical MBE system consists of three chambers: an introduction chamber where wafers are load-locked into the machine, a preparation chamber for wafer cleaning, and the main growth chamber. Chambers preceding the growth chamber are used to isolate the growth chamber so as to maintain a base pressure in the range of 10^{-10} torr. Such a low pressure is necessary to ensure an adequately clean growth environment and allow the various components operating at large thermal differentials from their surroundings to be thermally isolated. The beam nature of molecules and atoms refers to the ability of these constituents to travel from the effusion cell to the substrate unimpeded, a situation allowed by the UHV conditions. Growth rates in MBE tend to be relatively slow in comparison to other deposition techniques and as such require the stringent vacuum conditions to produce epitaxial layers of sufficient purity. Creating such a high vacuum environment requires several pumping techniques to be utilized. Typically, a combination of compressed helium cryo-pumps, ionization pumps, and LN_2 cryo panels provide the high capacity pumping needed to maintain low base pressures.

A generic layout of a MBE reactor is shown in Figure 3.1. Shuttered effusion cells are directed at the substrate in a manner such that the molecular beams are as isotropic across the wafer surface as possible. Ordinarily, effusion sources produce a

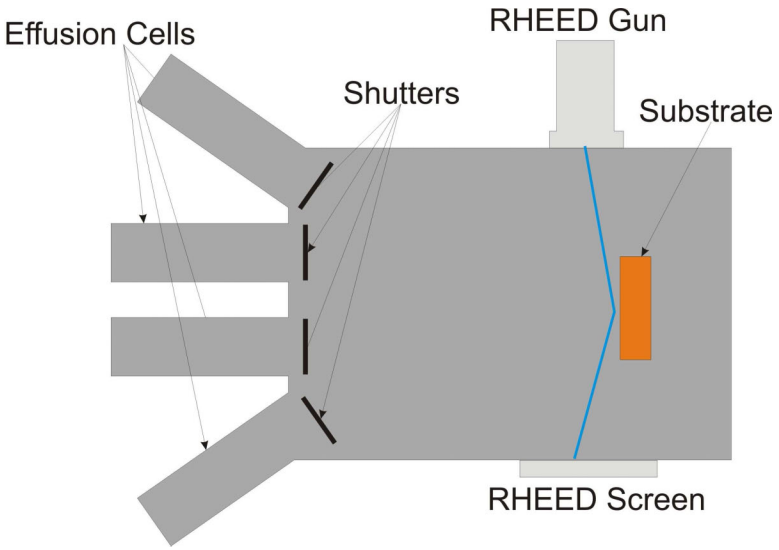

Figure 3.1: Layout of a typical MBE system.

flux distribution in the plane of the substrate that closely resembles the cosine law of effusion;

$$d\Gamma_\vartheta = \frac{\Gamma_e}{\pi}\cos(\vartheta)d\omega \tag{3.1}$$

where ϑ is the half angle of the cone subtended by the region of interest on the substrate with respect to the effusion cell, $d\omega$ is the solid angle differential, $d\Gamma_\vartheta$ is the differential effusion rate, and Γ_e is the total rate of effusion generated by the cell and able to escape the cell orifice. As a result of the cosine law of effusion, the flux distribution at some point b on the substrate is given by

$$I_b = I_c\cos^4(\vartheta) \tag{3.2}$$

where I_b is the impingement rate at point b radially displaced from the center, and I_c is the impingement rate at the center of the substrate [52]. The distribution of flux is thus determined by the distance between the substrate and crucible, angle of incidence of

the molecular beam, and geometry of the effusion cell. Given a substrate of sufficiently small diameter, the flux is assumed to be nearly isotropic, here this is often assumed to be the case. When considering growth on two-inch or three-inch substrates, corrections accounting for the cosine distribution may be required to produce a desired flux or flux ratio at the edges of the wafer. Short period superlattice device characteristics are particularly sensitive to layer thickness, and as such care must be taken to ensure layer uniformity across a large substrate. Substrate rotation is often employed to enhance uniformity across the wafer, with rotation speeds necessarily being on the order of the monolayer growth rate to ensure even deposition [53]. For example, a growth rate of 0.5 ML/sec corresponds to 30 ML/min, which equates to a substrate rotation speed of 30 RPM.

This work made use of a Veeco Epi930 MBE reactor equipped with gallium, indium, aluminum, arsenic, and antimony effusion cells. Dopants were beryllium and tellurium for p-type and n-type doping, respectively. The group V cells were also equipped with valved thermal cracking zones, allowing for the generation of dimeric arsenic and monomeric or dimeric antimony by thermal dissociation of the tetramer species. Use of cracked species allows flexibility in device design and further control over the growing epilayer, or near surface transition layer (NSTL). For instance the sticking coefficient of an impinging atomic species, defined as the ratio of atoms per unit area which are incorporated into the crystal to the total number of atoms incident on that region, is dependent on the species of the incident beam.

In the case of arsenic, As_4 has a sticking coefficient to the substrate of $C_s \leq 0.5$, while the sticking coefficient of As_2 can approach unity. Use of As_2 thus allows a lower beam flux of arsenic to sustain a given growth rate, reducing arsenic contamination in non arsenic-containing layers which arises due to the comparatively low sticking coefficient of As to the chamber surfaces [54]. The valved cracker cell also allows control over the arsenic pressure in the chamber and hence reduced arsenic background pressure during

the growth of non arsenic-containing layers [55]. While other species have a relatively high sticking coefficient to the cryo panels and chamber surfaces, this is not the case for arsenic, and high arsenic background levels may remain after closing the shutter. This gives rise to the so-called memory effect, where arsenic may still incorporate into layers which nominally contain no arsenic, despite closing the shutter and cracking zone valve.

3.2 MBE Deposition Process

Crystal growth by MBE is a process that occurs far from equilibrium, as the substrate and deposited epilayers are in the solid phase while the constituent beams incident on the substrate are in the vapor phase. The system is also far from thermal equilibrium, as the temperature of the substrate is different from that of the impinging beams which are assumed to be at the temperature of the source cell. The dynamics of the crystallization process occurring on the surface provide key insights into the MBE process, and will be briefly considered here in the context of binary III-V materials.

3.2.1 Lattice Incorporation

The thin film growth process by MBE is generally broken into three regions: substrate, near surface transition layer, and impinging beams as shown in Figure 3.2. An immense number of variables come into play which determine the growth dynamics in the NSTL. Substrate temperature plays a major role in the growing film, as this partially determines and often limits the sticking coefficients and surface mobilities of the impinging atoms. The surface mobility of a given species describes its ability to migrate on the growth surface before incorporation into the lattice. Lower substrate temperatures correspond to reduced surface mobility, and often lead to increased spiral mound formation as migrating atoms are quickly incorporated into the material.

Stoichiometric growth refers to the condition by which an equal fraction of group III and V atoms constitute the material. An excess or deficiency of group III atoms leads

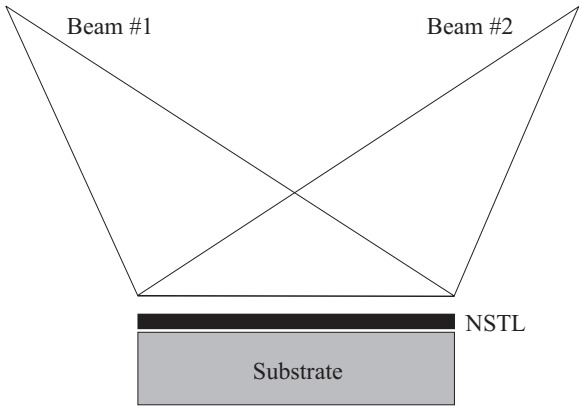

Figure 3.2: Primary regions of interest in the process of MBE deposition. The NSTL region is where the impinging beams intersect and crystallization occurs.

to metal rich or metal deficient conditions, respectively. Under typical growth conditions, the group III sticking coefficient is taken as unity, and the group III deposition rate controls the growth rate. Sufficient group V flux is applied to produce stoichiometric growth, and often an excess group V flux is used as only an adequate fraction of the impinging beam will be incorporated to sustain stoichiometry. Excess group V flux desorbs from the surface, however using high V/III flux ratios may leave residual group V material present in the chamber which may incorporate into subsequent layers. This situation warrants particular attention in short period superlattice materials as the time to deposit a single layer tends to be rather short, and residual material in the chamber can produce unexpected compositional variation in the interfaces and SL layers. Optimization of V/III flux ratios often needs to be carried out in order to ascertain the best growth conditions for a given material system.

While for low temperatures the group III sticking coefficient is assumed to be unity and sufficient group V flux is applied to sustain the group III incorporation rate, increased desorption of atoms from the surface occurs at higher growth temperatures. The congruent sublimation temperature T_{cs} defines the temperature above which a given compound loses stability and higher rates of desorption occur [56]. Values of T_{cs} for MBE-grown GaSb and InAs are 455°C and 387°C, respectively [57]. Desorption of

group III material may also occur at temperatures in excess of T_{cs}, causing layers to have reduced thickness if growth rate calibrations are performed at a lower temperature. In ternary compounds, this may lead to variation in the composition, as desorption conditions are material and species specific.

3.3 Strain

Heteroepitaxial growth is the process of depositing epitaxial layers with different material compositions, and often different lattice constants on a substrate. In the situation where materials with different lattice constants are deposited, forces generated by the interatomic potentials generate strain in the epilayer. When a material with a larger lattice constant than the substrate is grown, compressive forces act on the epilayer. Similarly, if the epilayer lattice constant is smaller than that of the substrate, tensile forces are present. This is due to the fact that the lattice constant of the epilayer is strained to that of the substrate, as the substrate can be considered infinitely thick with respect to the epilayer. This difference in spacing of the atoms in the crystal layers is known as misfit, and it can be described by the relation

$$f_m = \frac{a_{subs} - a_{epi}}{a_{epi}}, \tag{3.3}$$

where a_{subs} denotes the substrate lattice constant and a_{epi} the epilayer lattice constant [58]. The misfit is assumed to be in the $\hat{x} - \hat{y}$ plane which is perpendicular to the growth direction, $\hat{z}$. In this case, the strain in the $\hat{x}$ or $\hat{y}$ direction is equal to the misfit, and denoted by ε_{xx} or ε_{yy}. Two layers are said to be coherently strained if the lattices of the two materials are commensurate at the interface between them. In contrast a relaxed layer is one in which disturbances in the lattice form to accommodate the strain, and the lattice sites are no longer coterminous at the interface.

To calculate the strain and lattice constant in the growth direction, the elastic

properties of the material must be taken into account. When a material is put under compression or tension in one axis, it deforms in other axes to accommodate the force. In the case of an epilayer with a larger lattice constant than the substrate (compressive strain), the lattice constant in the growth direction increases due to the strain, and conversely for an epilayer with smaller lattice constant. To calculate the lattice constant in the growth direction for a single epilayer, one first needs to ascertain the strain in the growth direction which can be written as

$$\varepsilon_{zz} = -2 \cdot \frac{C_{12,epi}}{C_{11,epi}} \cdot \varepsilon_{xx}, \tag{3.4}$$

where C_{12} and C_{11} are the elastic constants of the epilayer. Elastic constants for the III-V semiconductors employed here are given in Table 3.1. For ternary materials which

Material	$C_{11} \cdot 10^{11}$ dyn·cm^2	$C_{12} \cdot 10^{11}$ dyn·cm^2	$C_{44} \cdot 10^{11}$ dyn·cm^2
GaSb	8.83	4.02	4.32
InAs	8.34	4.54	3.95
GaAs	11.9	5.34	5.96
InSb	6.67	3.65	3.02

Table 3.1: Elastic constants of III-V materials.

may be used in the device, the elastic constant can be expressed as a weighted average of the elastic constants of the constituent materials. For example, the elastic constants for ternary material $Ga_{1-x}In_xSb$ can be expressed as a combination of elastic constants of GaSb and InSb in the following manner:

$$C_{11,Ga_{1-x}In_xSb} = x \cdot C_{11,InSb} + (1-x) \cdot C_{11,GaSb}. \tag{3.5}$$

Once the strain in the growth direction is established, the growth direction lattice constant can be determined by calculating

$$a_z = a_{equilibrium} \cdot (1 + \varepsilon_{zz}). \tag{3.6}$$

This process can be repeated to calculate the strain for each individual epilayer in a given period of a structure. Once all individual strain components are obtained for a given period, the overall strain is calculated by treating a given layer set as a linear superposition of strain components. The in-plane strain components are multiplied by their respective layer thicknesses, then all of these components are summed and divided by the total layer thickness,

$$\varepsilon_{total} = \frac{\sum_i d_i \cdot \varepsilon_i}{\sum_i d_i}, \text{ i=0,1,2} \ldots \tag{3.7}$$

where d_i are the individual layer thicknesses.

3.3.1 Effects of Strain on Band Structure

Strain in mismatched heteroepitaxy alters the crystal potential in the strained layers, causing modification of the band structure. This effect can be exploited in band structure engineered materials and used as a design parameter to, for instance, suppress Auger recombination. Modification of the bands by strain can also lead to unexpected material properties if not accounted for. Perturbations to the bulk crystal structure have the effect of adding off-diagonal terms to the Hamiltonian matrix, thus causing the band structure in the strained epitaxial layer to change. Strain energy lifts the degeneracy of the HH and LH states at $k = 0$ as shown in Figure 3.3. Tensile strain displaces the LH state toward the conduction band, thus causing the LH state to determine the energy

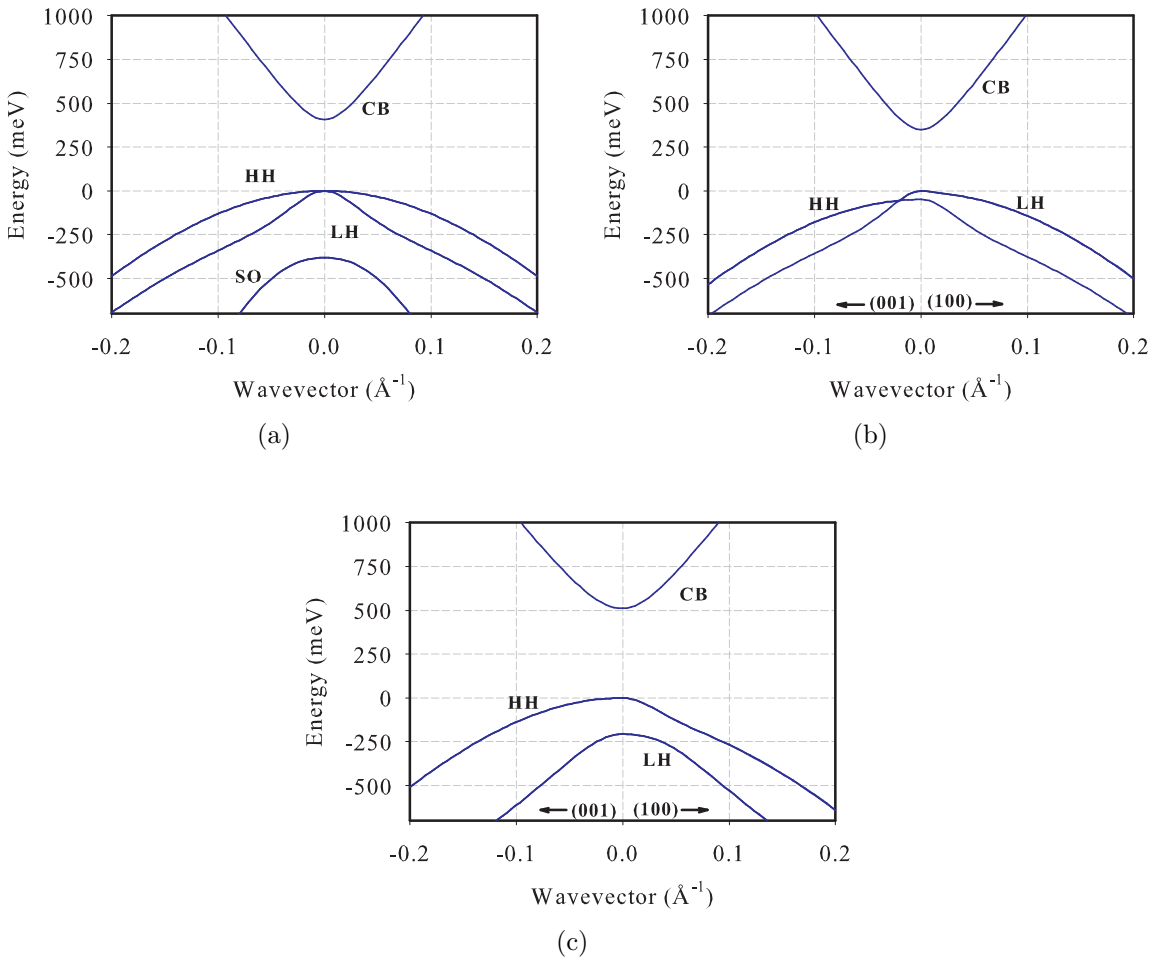

Figure 3.3: Effects of strain on the energy bands in semiconductors. The equilibrium band structure of InAs is shown in (a). Tensile strain shown in (b) has the effect of reducing the energy gap by lifting the HH-LH degeneracy and displacing the LH band towards the CB. Compressive strain (c) increases the energy gap by shifting the conduction band upwards.

gap, which is reduced in this case [58]. The HH state determines the energy gap in compressively strained layers, but the energy gap is increased as the conduction state is displaced higher in electron energy. While these tendencies hold for single strained layers treated as bulk material, more rigorous band structure calculations are required to adequately assess the effects of strain in complex heterostructures. In the case of InAs on a GaSb substrate, the epitaxial layer is in tension and the shift in the energy

gap can be quantified as follows:

$$\Delta E_g = A_2 \varepsilon, \tag{3.8}$$

$$A_2 = -2a\frac{C_{11} - C_{12}}{C_{11}} - b\frac{C_{11} + 2C_{12}}{C_{11}}. \tag{3.9}$$

Here a is the hydrostatic deformation potential, b is the shear deformation potential, ε is the mismatch, and C_{ij} are the elastic constants [58].

Lifting of the valence band degeneracy by strain can be employed as a design tool for Auger suppression. Auger recombination processes require conservation of both energy and momentum, thus selectively shifting the bands can forbid such transitions from occurring. Deliberate band engineering can suppress Auger rates by orders of magnitude [59], however such optimizations often lack generality and are specific to a given structure and set of operating conditions. For example, optimizations are often only valid for a narrow range of temperatures, as the band gap and carrier distributions at the band edges are temperature sensitive.

3.4 Critical Thickness and Misfit

For sufficiently thin heteroepitaxial layers, the misfit strain can be totally accommodated and the layer will be pseudomorphic with the substrate. In this case, the in-plane lattice constant of the epilayer will be coherently strained to that of the substrate as seen in Figure 3.4(a). The strain in the epilayer can be accommodated up to a certain thickness, referred to as the critical thickness h_c, beyond which it becomes energetically favorable to form dislocations. In the context of crystallography, dislocations are defined as a perturbation of the crystal structure in an otherwise highly ordered lattice. The formation of dislocations to relieve the energy due to strain is referred to as lattice relaxation, and in general part of the mismatch is accommodated by strain and

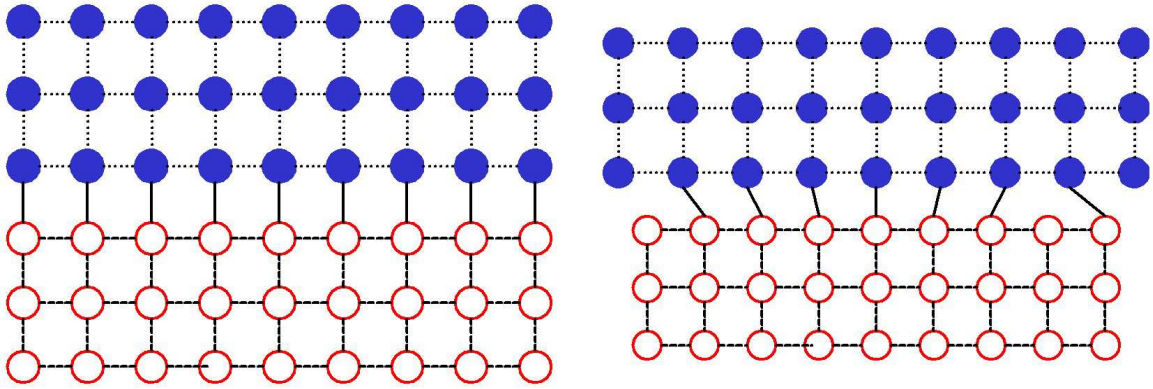

(a) (b)

Figure 3.4: Compressively strained epilayer where substrate atoms are represented by hollow circles and epilayer atoms by solid circles, interface bonds are solid lines. (a) The epilayer is pseudomorphic with the substrate and no dislocations are present. (b) Dislocations form to lower the energy state of the epilayer.

part by dislocation formation. Dislocation formation is shown in Figure 3.4(b), where it can be seen that the epilayer is no longer commensurate with the substrate lattice. Such dislocations in sufficient quantity degrade the quality of heterostructure devices. Dislocations break the crystal translational symmetry, which can introduce deep level defects into the device and provide nonradiative recombination centers [60]. Current paths can also be created by such dislocations, which can increase dark currents in detector devices and leakage currents in LED structures.

Several formalisms exist for calculating the critical thickness. The force balance method developed by Matthews and Blakeslee [17] is a generally accepted method of calculating a lower bound on the critical layer thickness (CLT). In this method the driving force for the motion of a threading dislocation is equated to zero and solved to give

$$h_c = \frac{b^2[1 - \nu\cos^2(\beta)]}{8\pi f_m(1+\nu)b_1}\ln\left(\frac{\rho_c h_c}{q}\right) \tag{3.10}$$

where b is the magnitude of the Burgers vector defined in Equation 3.12, ν is Poisson's ratio given in Table 3.3, β is the angle between the dislocation and Burgers vector, $b_1 = b\cos(\beta)$, and f_m is the misfit [58]. The Burgers vector used to describe dislocations is given by

$$\overrightarrow{\boldsymbol{b}} = \frac{a_o}{2}[h\ k\ l], \tag{3.11}$$

where a_0 is the lattice constant and h, k and l are the Miller indices. The magnitude of the Burgers vector is given as

$$b = \frac{a_0}{2}\sqrt{h^2 + k^2 + l^2}, \tag{3.12}$$

which reduces to $a_0\sqrt{2}/2$ for the general case of the (110) crystal axis. The value of β is generally taken to be 60° in cases of small ($\leq 1\%$) misfit. For growth in the (001) direction, the Burgers vectors are taken to have an inclination to the dislocation of 45° [17]. Values of the critical thickness for various material combinations are given in Table 3.2, where it can be seen that only very thin layers can be grown when the mismatch is large.

Substrate	Epilayer	f_m	CLT (Å)	CLT (ML)
GaSb	InAs	-6.2×10^{-3}	194	64.1
GaSb	InSb	5.9×10^{-2}	7.2	2.2
GaSb	$Ga_{0.75}In_{0.25}Sb$	1.5×10^{-2}	62.5	20.2
GaAs	GaSb	7.3×10^{-2}	4.2	1.4
GaAs	InAs	6.7×10^{-2}	4.9	1.6

Table 3.2: Mismatch and critical layer thickness.

Material	Bulk Modulus $B_s \cdot 10^{11}$ dyn·cm^2	Shear Modulus C'·10^{11} dyn·cm^2	Young's Modulus $Y_o \cdot 10^{11}$ dyn·cm^2	Poisson Ratio ν
GaSb	5.62	2.4	6.31	0.31
InAs	5.8	1.90	5.14	0.35
GaAs	7.53	3.285	8.59	0.31
InSb	4.66	1.51	4.09	0.35

Table 3.3: Mechanical constants of III-V materials used in strain calculations.

CHAPTER 4
OPTIMIZATION OF BULK GALLIUM ANTIMONIDE

Epitaxial growth of semiconductor crystals requires a high quality, atomically smooth surface on which to commence growth. This surface provides a seed surface, as the epilayer quality will be affected by that of the surface on which it is grown. Imperfections present at the seed surface tend to migrate through the overlying epilayer, and as such should be minimized to produce high quality epitaxial material. Often the most accommodating substrate for growth of 6.1 Å heterostructures is GaSb due to availability and the ease of lattice-matching. While MBE growth of arsenide compounds has been honed to the point that only few oval defects per square centimeter are obtainable [61, 62], growth of GaSb is comparatively immature and defect densities are generally much higher. Suppression of surface roughness and defects (both microstructural and oval) is necessary to produce high quality optoelectronic devices with high yield across the wafer and good device consistency. While for thin layers oval defect formation may be of little consequence, these defects tend to become larger and more numerous as device thickness is increased, a situation which is problematic for a variety of reasons.

In order to provide the best possible surface for growth, a buffer layer of the same material of the substrate is most commonly grown prior to growth of the desired structure. The buffer layer not only smooths the growth surface, but also buries any residual oxide and impurities which were not removed during the various stages of chemical and thermal cleaning. In addition to requiring a high quality seed surface, terminating devices with a high quality layer is also often necessary for carrier confinement, making electrical contacts, and protection of the active material from atmospheric contamination. Measurement of contaminant concentrations in MBE-grown material may be made by secondary ion mass spectroscopy (SIMS), whereby a depth profile is created as ion

bombardment removes material from the surface and the removed material is analyzed for composition and concentration. Carbon and oxygen are the primary contaminants in MBE-grown material; Figure 4.1 highlights the levels of these substances in a cascaded LED structure. This result emphasizes the need to minimize impurity incorporation in epitaxially-grown semiconductors at multiple stages in device development. The oxygen and carbon background levels of approximately 1×10^{17} cm^{-3} represent the noise floor for the SIMS measurements and do not represent actual levels of contamination in the active region. Roughening of antimonides during cesium ion sputtering for material removal likely impacts the measurement sensitivity.

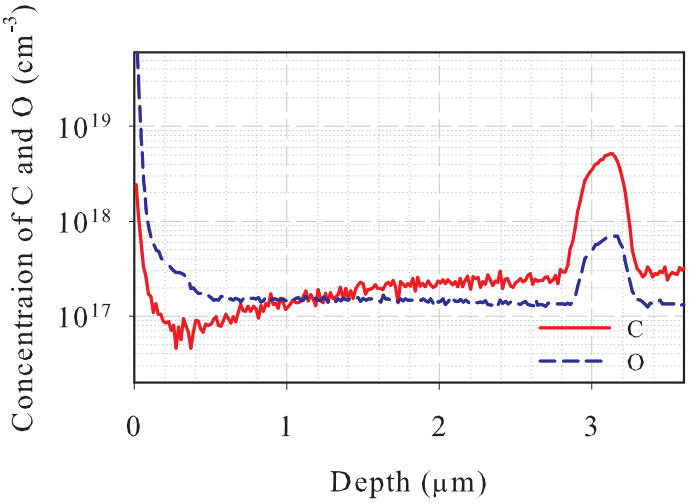

Figure 4.1: Measurement of oxygen (dashed line) and carbon (solid line) contamination in a MBE-grown cascaded LED structure on a GaSb substrate. Contamination at the substrate/epi interface (3 μm depth) stems from incomplete removal of impurities during etching/desorption and diffusion of the impurities into the substrate. Impurities in the device surface (0-400 nm depth) occur due to exposure to atmosphere post-growth.

Structures considered here are based on the InAs/GaSb superlattice system grown on GaSb substrates. To optimize growth of superlattice material, the growth of GaSb bulk layers was investigated to provide the best possible starting growth surfaces and cap layers. Several growth parameters were varied in order to ascertain the best set of growth conditions for high optical and morphological quality. The effects of oxide

desorption conditions, sample cooling conditions, and growth temperature were investigated and optimized for bulk GaSb layers grown on p-type GaSb substrates. Use of p-type substrates prevented the formation of a p-n junction, as GaSb has a background p-doping level of 10^{16}-10^{17} cm^{-3} due to a native defect. Presence of a p-n junction may lead to anomalous results in photoluminescence measurements as the junction creates a space charge field, thereby causing spatial separation of carriers.

4.1 Oxide Desorption Conditions

Removal of the native oxide and impurities from semiconductor substrates prior to growth is a crucial step in any epitaxial growth technique. A thin oxide layer forms on semiconductor surfaces upon exposure to atmosphere; this layer must be removed to encourage monocrystalline growth at the substrate/buffer interface. Wafers grown by MBE are typically thermally treated in the growth chamber to remove the oxide layer in a process known as thermal oxide desorption. Often pre-treatments such as chemical etching are employed to remove the majority of the oxide prior to in-situ desorption [63, 64]. Removal of the thick oxide layer is beneficial due to the reduced surface roughening that occurs during thermal desorption [65]. Surface atoms are consumed during the desorption process, thus excessively thick oxide layers may cause roughening or leave the surface non-stoichiometric. Treating the substrate with a UV-ozone process prior to growth has been shown to substantially reduce carbon at the surface of the wafer, a major source of contamination in MBE grown material [66, 67]. In this technique contaminants are removed from the wafer surface and oxide re-growth is encouraged by the UV-ozone exposure. Moving carbon from the substrate/oxide interface into the grown oxide layer allows the carbon to be removed during thermal oxide desorption. Atomic hydrogen cleaning may also be applied in-situ to assist in oxide removal or allow the process to occur at a lower temperature [68, 69].

Substrates were purchased "epi-ready" from the vendor, however only GaAs substrates are treated as such and directly loaded into the MBE system. The meaning of "epi-ready" is often vague, and strongly depends on the storage conditions of the wafers, packaging by the manufacturer, and length of storage before use [70]. A cleaning and chemical etching process was used in the case of GaSb substrates in order to assist in removal of the native oxide. Wafers were degreased in trichloroethylene, rinsed in 2-propanol, and etched for 5 min in an undiluted HCl bath to minimize the oxide thickness [71, 72]. Acid etching was intended to reduce the native oxide thickness, while leaving the underlying substrate surface unharmed [73]. Post-etch rinses in 2-propanol removed residual acid, and did not encourage re-growth of oxide, a problem that arises if H_2O rinses are applied. Subsequent to the cleaning and etching process, wafers were either loaded into the MBE reactor or stored in a dry nitrogen atmosphere to reduce the reformation of surface oxide.

Optimization of in-situ oxide desorption conditions of GaSb was performed in order to improve the growth surface morphology, as well as optical and electronic properties of the material. The two parameters of interest here were the antimony stabilization flux present during heating and annealing of the substrate, and the final annealing temperature. All substrates were prepared in the same fashion, and desorption conditions (i.e. temperature ramps and annealing temperatures/times) were held constant and computer controlled for consistency. Growth recipes consisted of only a 1.0 μm GaSb layer, grown at 0.55 ML/sec with a Sb/Ga beam equivalent pressure (BEP) ratio of 2.5 as measured by an ion gauge. All sample preparation was performed in a class-100 cleanroom environment to minimize particulate-generated defects [74, 75].

4.1.1 Desorption Anneal Temperature

Adequate removal of the native oxide layer and impurities at the substrate surface prior to epitaxial growth is crucial in production of high quality optoelectronic devices.

In-situ substrate cleaning began upon introduction to the first chamber of the MBE system. Wafers were thermally cleaned at 175°C under vacuum for two hours, and transferred to a buffer chamber. Further outgassing of the substrate and holder were performed at 250°C in order to keep outgassing in the growth chamber to a minimum. Temperatures higher than 250°C were avoided in the first two chambers to prevent potential surface damage, as no antimony stabilization flux was present during the heating process. Flux of group V material is necessary to stabilize the wafer surface during heating at elevated temperatures, and failure to apply sufficient flux at high temperature is shown in the following to cause surface roughening and defect formation.

Upon introduction to the growth chamber, wafers were immediately heated to a 200°C base temperature to avoid condensation of residual impurities on the surface. Wafers were then heated by a computer script which controlled the temperature setpoints and ramp rates while the reflection high energy electron diffraction (RHEED) pattern was observed to monitor the progress of oxide removal. The temperature was monitored both by a thermocouple located behind the substrate holder, and by an optical pyrometer facing the substrate at normal incidence. The pyrometer temperature was calibrated by referencing a GaSb surface reconstruction ($1 \times 3 \leftrightarrow 2 \times 5$) at a given antimony stabilization flux [76]. Henceforth, all quoted temperature values are stated as measured by a pyrometer unless otherwise noted. Initially no RHEED pattern was observable, as the surface was covered by several nanometers of oxide. However, the GaSb (1×3) reconstruction pattern began to appear near 480±5°C, and typically cleared to a streaky RHEED pattern by 500°C, indicating a smooth growth surface.

Two primary oxide species exist on GaSb wafers: antimony oxide (Sb_2O_3), and gallium oxide (Ga_2O_3). Antimony oxide has been shown to desorb at relatively low temperatures, beginning at 250°C, however gallium oxide requires higher temperatures for effective removal [77, 78]. To investigate the effect of annealing temperature, three

samples were grown with annealing temperatures of 505°C, 525°C, and 545°C. All annealing times at the specified temperatures were 15 minutes under antimony stabilization pressure of 2.5×10^{-7} torr. Samples were analyzed by optical/interference microscopy, atomic force microscopy, and photoluminescence spectroscopy to determine the defect density, RMS roughness and growth mode, and optical quality, respectively.

Substrate wafers may be purchased either nominally "flat" or "vicinal", flat indicating that the wafer was cut as close as possible to the specified axis (typically within 0.1°), and vicinal cut with a specified angle offset from the specified axis. Wafers used in this work were flat, however the small offset from the specified crystal axis causes epitaxial films to condense in the "step-terraced" form. This may be observed under high resolution microscopy as monolayer high terraces; the described feature manifests in many of the following images. Root-mean-squared (RMS) surface roughness values when this growth mode is observed, as measured by atomic force microscopy, are often only ∼2 Å, indicating high quality epitaxial surfaces.

Initially a control sample was grown which employed an anneal temperature of 505°C, or only $10 - 15$°C above the temperature at which the RHEED pattern became streaky. Its was expected that since the RHEED pattern was acceptable, the majority of the gallium oxide had been removed. Observation of the RHEED pattern of the samples annealed at 525°C and 545°C did not vary noticeably from the first sample, indicating that the bulk of the oxide layer had been removed in all cases. Samples were analyzed by photoluminescence (PL) spectroscopy at 77 K to ascertain the peak wavelength, spectral shape, and relative emission intensities. Photoluminescence spectra were similar for all samples, with FWHM values of approximately 4.5 $k_B T$ and peak emission wavelength of 1.58 μm (785 meV) as shown in Figure 4.2. The intensities varied little, with only a 20% maximum difference, indicating that once the RHEED pattern became streaky and clear the oxide was largely desorbed and further improvements by increasing temperature were minimal.

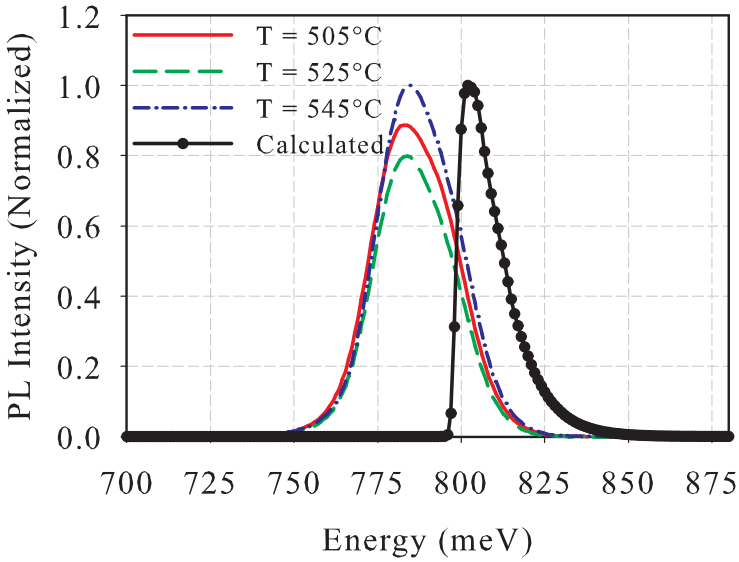

Figure 4.2: Photoluminescence spectra taken at 77 K from samples desorbed at various temperatures. The highest desorption temperature corresponded to the highest peak intensity, however a general trend was not observed. Excitation was by 832 nm diode laser, irradiance at the sample was 15 W/cm^2. Calculated PL from band-to-band transitions is shown (solid circles) for reference.

Also shown in Figure 4.2 is the calculated photoluminescence spectrum of GaSb for low excitation density (injection of 1×10^{16} cm^{-3}). Despite the difference of 18 meV in the peaks of the measured and calculated spectra, the measured spectra are attributed to band-to-band transitions. While the temperature sensor in the cryo-cooler indicated 77 K during measurement, the actual temperature at the sample was likely somewhat higher due to the thermal impedance of the grease used to mount the samples and heating from ambient radiation. Identification of individual emission lines is possible at lower temperature [79], typically 4.2 K, however this capability was not available for the measurements shown here.

Microscopic analysis revealed that, while the PL intensity was highest for the sample desorbed at 545°C, the morphology was clearly the worst. The defect density was a factor of three greater than the other samples, and the RMS roughness was marginally worse. Atomic force microscopy (AFM) showed that the samples desorbed at

lower temperatures had grown in the expected step-terraced mode and surface roughness was ∼2 Å. Desorption at 545°C had also produced a step-like surface, however the appearance was random in nature and significant island formation was present as shown in Figure 4.3(c). Images and analysis of AFM data presented here were generated with software described by Horcas *et al.* [80]. A possible explanation for the increased

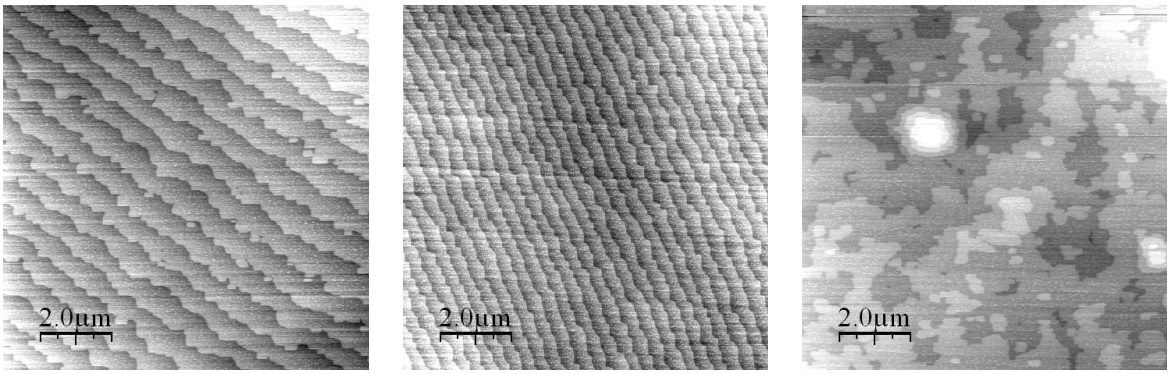

(a) (b) (c)

Figure 4.3: Surface morphologies of GaSb buffer layers, the variable parameter was desorption anneal temperature. Corresponding RMS roughness values and estimated oval defect densities were: (a) 2.02 Å, 7.2×10^3 cm^{-2}; (b) 1.80 Å, 7.6×10^3 cm^{-2}; (c) 2.86 Å, 2.56×10^4 cm^{-2}. The etch pit density of wafers used in this sample series was $\sim10^4$ cm^{-2}. While the surfaces of the samples in (a) and (b) exhibit the typically observed step-terraced characteristic, the surface in (c) shows significant island formation and randomly oriented step terraces.

defect density and roughness is antimony desorption from the surface of the wafer; a situation that may be averted by increasing the antimony stabilization flux during annealing. A comparison of the SIMS data shown in Figure 4.1 and data taken for a sample grown previously with lower oxide desorption anneal temperature (not shown) suggested that oxygen contamination was reduced by increasing the anneal temperature. Photoluminescence response is expected to increase accordingly.

4.1.2 Antimony Stabilization Flux Application

Due to the critical nature of keeping III-V semiconductor surfaces stabilized while at elevated temperature and simultaneously avoiding condensation of group V material on the surface (provided that such condensation is not desired for passivation purposes), a group of samples was grown to examine the effects of stabilization flux application/removal temperature. As antimony is known to condense at wafer temperatures <350°C, the desire was to establish a heating/cooling sequence which yielded a smooth surface with no condensation or thermal pitting. Three samples were grown where the temperature of antimony stabilization flux application/removal temperature was 295°C, 315°C, and 350°C. During substrate cool-down after growth, the ramp rate for substrate temperature was held at 25°C/min; the highest controlled ramp rate sustainable in this MBE system for the wafer mounting blocks used. Roughness analysis and surface images are shown in Figure 4.4; the highest temperature case exhibited broader step-edges which were less ordered than in the lower temperature cases.

Examination of the photoluminescence spectra of these samples suggested that the application/removal temperature of 350°C was detrimental to surface quality. The broad

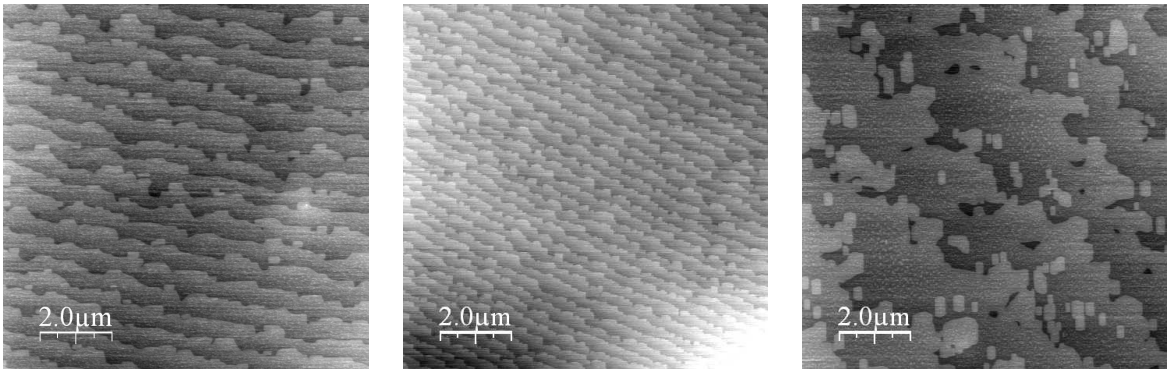

(a) T=295°C (b) T=315°C (c) T=350°C

Figure 4.4: Images of samples where antimony flux was commenced and terminated at increasing temperature during heat-up and cool-down. Corresponding RMS roughness values and estimated oval defect densities were: (a) 2.07 Å, 1.1×10^4 cm^{-2}; (b) 1.98 Å, 9.6×10^3 cm^{-2}; (c) 1.3 Å, 1.4×10^4 cm^{-2}. The etch pit density of wafers used in this sample series was $\sim10^4$ cm^{-2}.

feature at low energy shown in Figure 4.5 has not been identified, however it was likely due to defect states within the energy gap. Such wide-band defect luminescence has been observed in GaN grown by various techniques, and was attributed to both shallow and deep centers in the material [81, 82]. No spectral sub-features could be specifically resolved at 77 K; lower temperature measurement may provide added information as to the source of the luminescence. The decrease in intensity was attributed to an increased level of nonradiative recombination centers at the surface which arose due to the deficiency of antimony, leaving the surface non-stoichiometric.

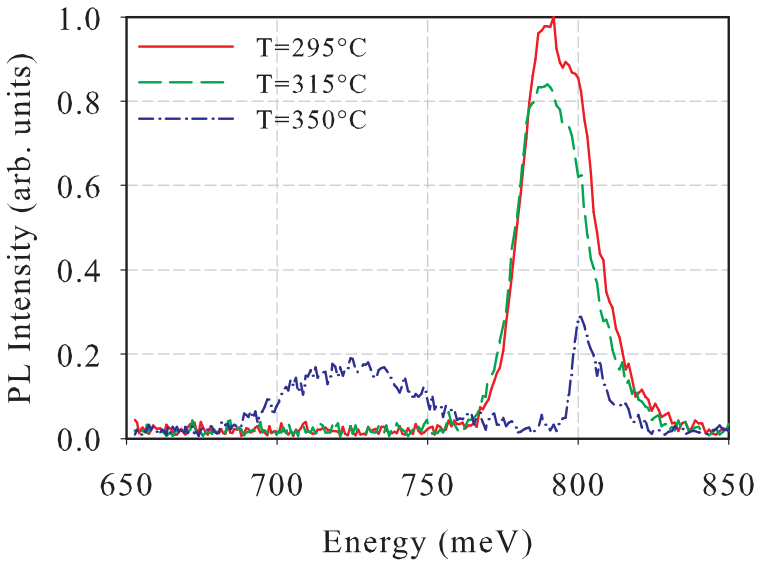

Figure 4.5: Photoluminescence spectra of undoped GaSb layers where the temperature of antimony application/removal temperature was varied. The excitation was provided by a diode laser operating at 832 nm with irradiance at the sample of 5 W/cm^2. The highest temperature case exhibited reduced PL from band-to-band transitions, as well as a broad spectral feature at low energy.

4.1.3 Antimony Stabilization Flux Level

In addition to the temperature of application/removal of antimony stabilization flux, the flux pressure was also of interest for optimization. Clearly as the temperature was increased, the rate of antimony desorption from the surface increased; thereby requiring increased group V stabilization to maintain stoichiometry. Not only must the surface be stabilized, but the wafer conditions during flux application should be such that antimony does not remain on the surface post-growth (again, provided that this is not the intention). Samples were grown under the same conditions as those described previously, with the beam equivalent pressure of antimony stabilization being the only variable investigated. Antimony BEP values of 5×10^{-8} torr, 2.5×10^{-7} torr, and 1×10^{-6} torr were applied while wafers were at elevated temperature; 9×10^{-7} torr being the value which was used for deposition of the nominally undoped GaSb layer. In this sample series, the substrate temperature ramp during cool-down was held at 25°C/min and the temperature at which antimony flux was commenced and terminated was 315°C. The temperature during thermal oxide desorption was 525±3°C and the anneal time was 15 minutes.

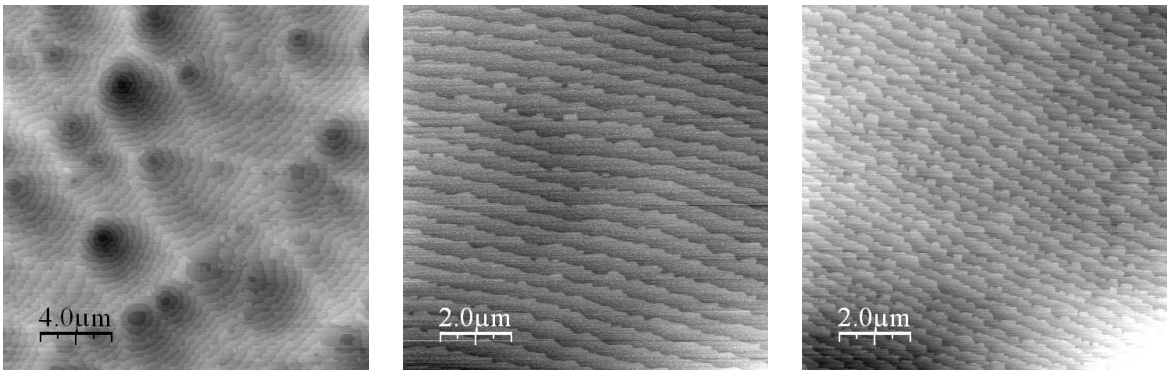

(a) BEP=5×10^{-8} torr (b) BEP=2.5×10^{-7} torr (c) BEP=1×10^{-6} torr

Figure 4.6: Images of samples where the level of antimony stabilization flux was varied while the wafers were at elevated temperature and no deposition was in progress. Corresponding RMS roughness values and estimated oval defect densities were: (a) 3.25 Å, 5.2×10^{4} cm^{-2}; (b) 1.65 Å, 1.1×10^{4} cm^{-2}; (c) 1.98 Å, 9.6×10^{3} cm^{-2}. The etch pit density of wafers used in this sample series was $\sim10^{4}$ cm^{-2}.

From the AFM image of the surface corresponding to the lowest applied flux shown in Figure 4.6(a), pitting of the surface was apparent. Oval defect density was also observed to decrease with increasing antimony stabilization flux; an image of the oval defects is shown in Figure 4.7 for the case of lowest antimony flux. This reduction

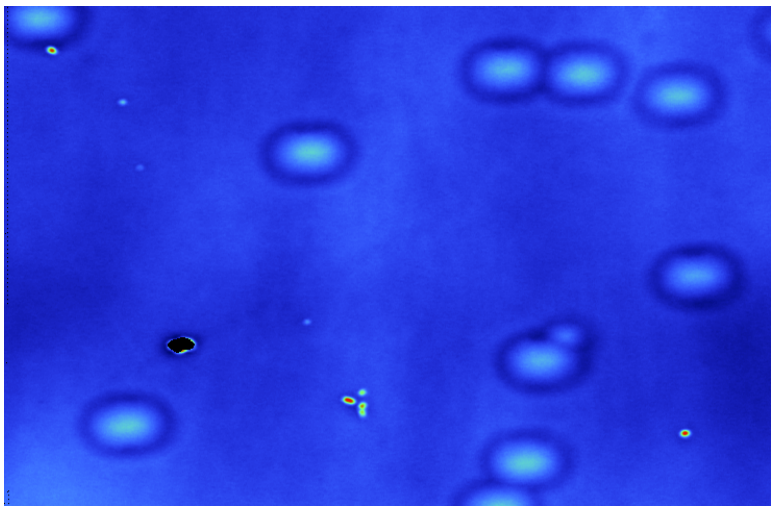

Figure 4.7: Micrograph of oval defects on the sample stabilized with antimony flux of 5×10^{-8} torr, the scan area was 122×93 μm^2. Analysis by interference microscopy measured the defects to be $\sim$10 nm in height.

in morphological quality was attributed to insufficient antimony pressure to ensure a stoichiometric surface. Surface pitting notwithstanding, the optical quality of the sample was not severely degraded as in the case of antimony flux application temperature being excessive [Figure 4.4(c)]. However, the photoluminescence intensity was observed to increase with antimony stabilization pressure as shown in Figure 4.8. At even the highest flux level (1×10^{-6} torr) no antimony condensation was observed when the wafer was cooled to 315°C provided that the flux was immediately terminated upon reaching that temperature.

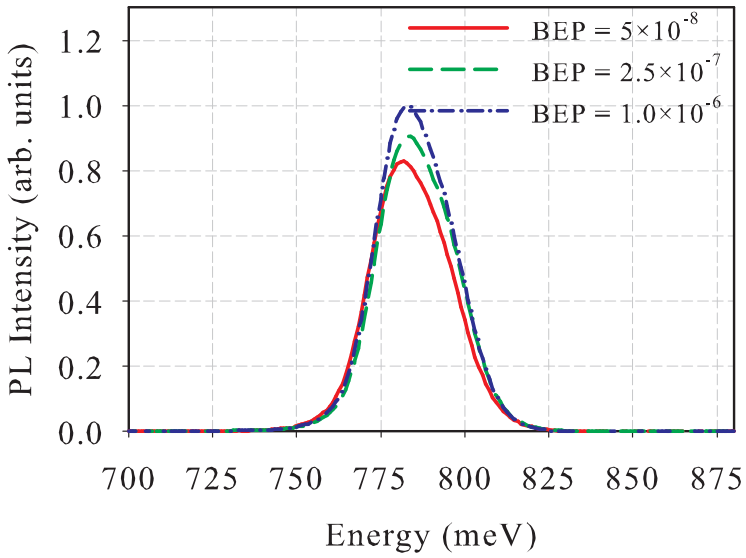

Figure 4.8: Photoluminescence of GaSb samples where the level of antimony flux applied while the wafer was at elevated temperature was varied. Flux values in the legend are given in torr.

4.2 Substrate Cooling and Antimony Capping

Typically for the GaSb based structures considered here, growth temperatures are reported in the range of $420 - 530°C$, clearly above the threshold for surface damage to occur in the absence of a antimony stabilization flux. As such, antimony flux was applied to the wafers after growth until the substrate reached a suitably low temperature during cool down. While the substrate is at elevated temperatures, antimony only stabilizes the surface and prevents material desorption and surface roughening, however antimony condensation on the wafer surface does not occur. This is, however, not the case after the substrate has reached temperatures below 350°C, at which point antimony layers may condense on the surface. Growth of antimony layers may be beneficial for wafer encapsulation or passivation when transferring the wafer to a separate growth or analysis chamber requires exposure to ambient conditions [83, 84]. Here it is demonstrated that antimony layer condensation may pose difficulties in device processing and testing, and thus substrate cooling should be controlled in such a fashion to halt antimony flux

application before condensation occurs.

Condensation of antimony on the wafer surface may be easily assessed by both AFM and x-ray photoelectron spectroscopy (XPS). Surface images of several samples with varying degrees of antimony condensation are shown in Figure 4.9. The antimony

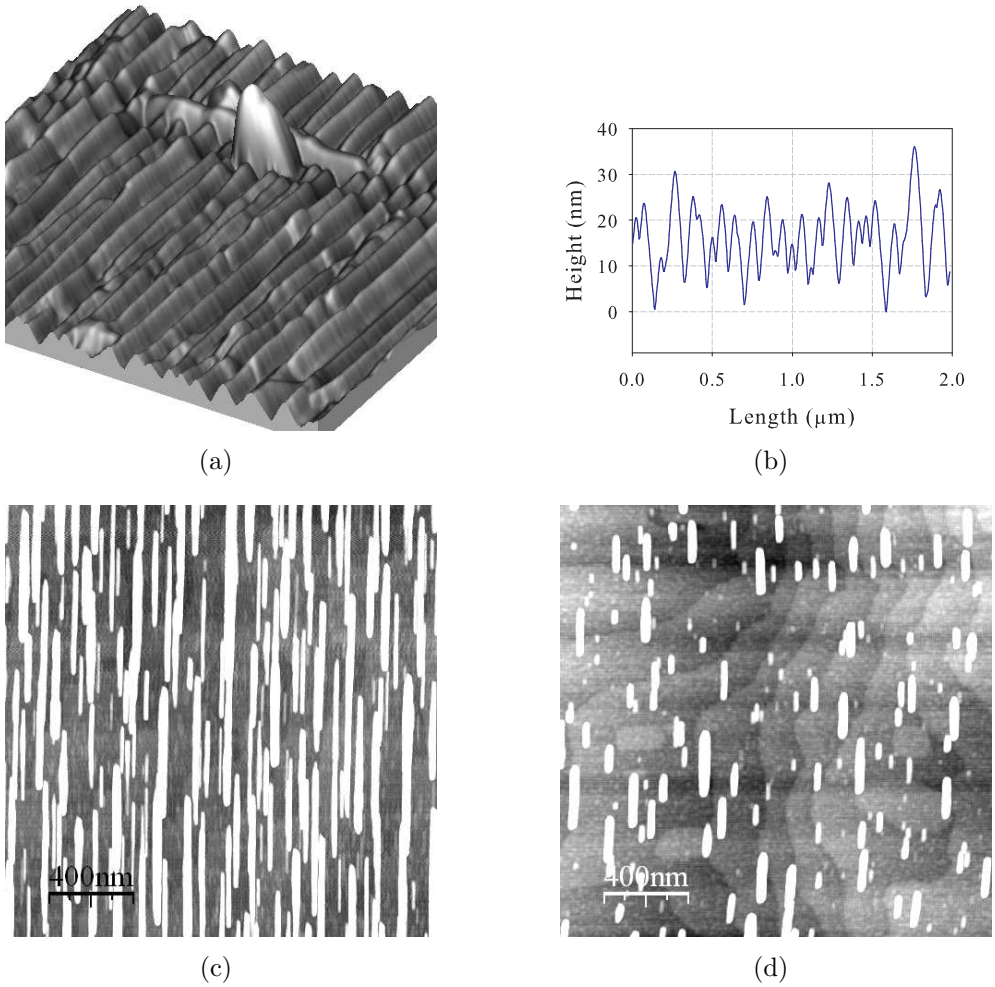

(a) (b)

(c) (d)

Figure 4.9: Images of GaSb buffer layers with varying degrees of antimony coverage. (a) Complete antimony coverage with no detectable Ga Signal by XPS, antimony was observed to condense in a striated pattern. (b) Profile (line scan) of the antimony covered surface. (c) Partial antimony coverage, with the chemical composition measured to be $Ga_{0.34}Sb_{0.66}$. (d) Surface largely clear of antimony, terraced GaSb growth was present below the residual antimony, the composition was $Ga_{0.47}Sb_{0.53}$.

condensation appeared as a striated pattern. Such surfaces with heavy antimony condensation exhibited high RMS roughness values, often on the order of ∼5 nm. Analysis by XPS is shown in Figure 4.10, where it was demonstrated that the wafer with anti-

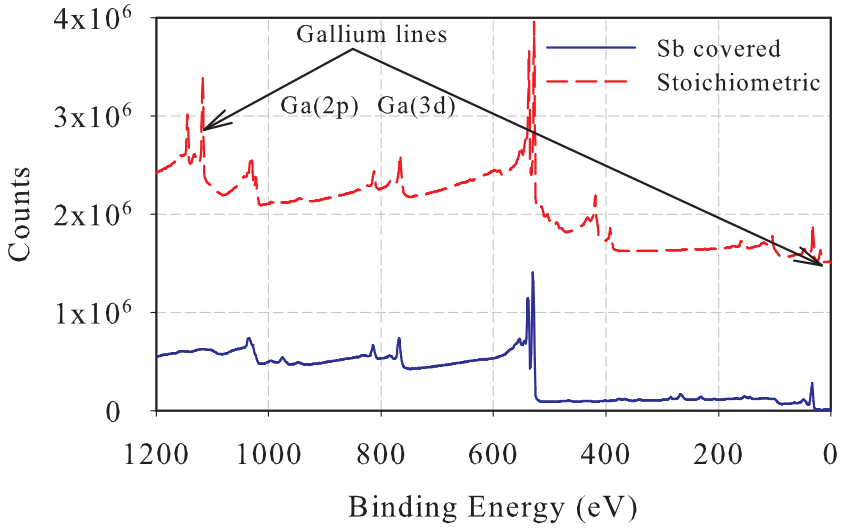

Figure 4.10: XPS spectra of two GaSb buffer samples, one of which is stoichiometric and the other completely covered by a Sb layer. In the bottom plot, the Ga_{2p} and Ga_{3d} lines were absent even after sputtering several nanometers into the surface, indicating heavy Sb coverage.

mony coverage showed no gallium spectral lines, while the wafer with a step-terraced surface was nearly stoichiometric as quantified by the Ga_{3d} and Sb_{4d} lines. Samples with the same structure as those with PL spectra shown in Figure 4.2, but with an antimony layer intentionally grown, were shown to have no measurable PL output. The antimony layer was expected to be absorbing to both the excitation laser and emitted PL, as well as provide trap states at the Sb/GaSb interface. Thus the presence of antimony on the surface may cloud results about material quality or simply eliminate PL output altogether.

Visualization of the progression of antimony condensation is possible by comparing Figures 4.9(a), 4.9(c), and 4.9(d). While complete antimony coverage is present in

Figure 4.9(a), the degree of coverage decreases for the following samples to the point that the terraced GaSb surface is visible below the streaks of antimony in Figure 4.9(d). Corresponding chemical composition analysis is given for each surface in the caption, showing that the antimony cap scarcely formed in the case of Figure 4.9(d).

Presence of antimony on the surface of wafers was also observed to degrade the quality of wet-etched mesa structures. While antimony did not act as an etch-stop for a citric-acid based wet-etch, roughening of the sidewalls was pronounced as shown in Figure 4.11. The striated pattern observed in the antimony layer [Figure 4.9(a))] appeared in the etched surface as well, indicating that the etch was unable to smooth the antimony layer. While clearly defined mesas were formed even with the antimony layer present, the substantial roughening of the sidewalls may pose difficulties in meeting certain design goals. Etching of angled facets in LED structures is expected to enhance output by Fresnel reflections as described in Section 2.5.1; roughening of mesa sidewalls may act to couple light out of the sidewall or scatter it randomly, thus directed such that it cannot contribute to useful output.

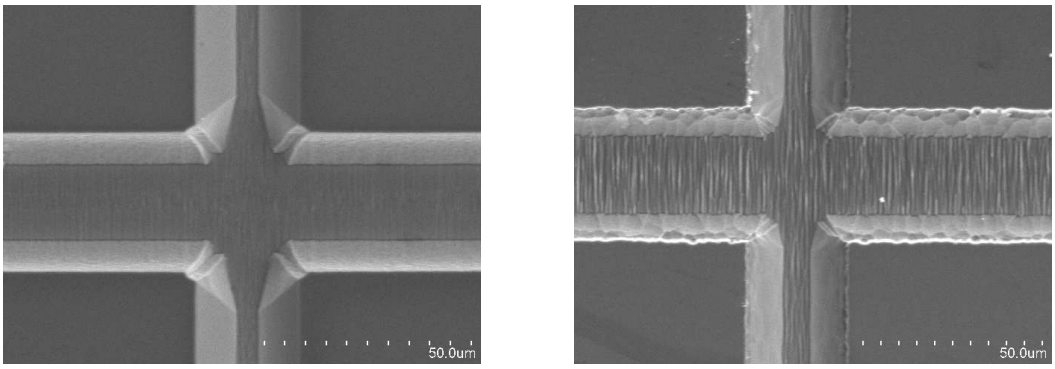

(a) (b)

Figure 4.11: (a) SEM image of anisotropic wet etching of mesas in a sample which has no antimony cap layer. (b) The same etch performed on a sample which has an antimony cap.

4.3 Growth Temperature Optimization

After optimization of antimony stabilization flux level and application temperature, and desorption temperature, a final sample series was grown to investigate the effects of GaSb growth temperature on morphological and optical quality. Growth temperature typically has a substantial impact on properties of epitaxially grown material; some materials only have a narrow temperature range where growth is even possible [85]. Other materials such as GaAs grow over a wide range of temperature, with electronic properties being substantially different at the extremes. Growth temperatures for GaSb from 440°C to 520°C were investigated here. For all samples antimony stabilization flux was applied and removed at 315°C, the flux level was 1×10^{-6} torr while the wafer was at elevated temperature, the thermal oxide desorption anneal temperature was 525°C, and the duration of the anneal was 15 minutes. As noted in the caption of Figure 4.12, the oval defect densities were lower than for the other sample series. While optimized growth conditions likely contributed to this improvement, the reduced etch-pit density of this GaSb wafer set is noted.

Over the range of growth temperatures tested, morphological quality varied little. Surface roughness was similar for all samples, and oval defect density was not observed to increase substantially even for the highest temperature. Optical output increased with increasing growth temperature as shown in Figure 4.13; no change in the spectral shape was observed. Optical quality is suspected to increase with growth temperature due to the increased surface mobility of atoms and molecules on the developing epilayer. Often optical quality increases with growth temperature up to a critical temperature, beyond which structural failure of the device (often due to layer inter-diffusion and interface roughening) ensues [86].

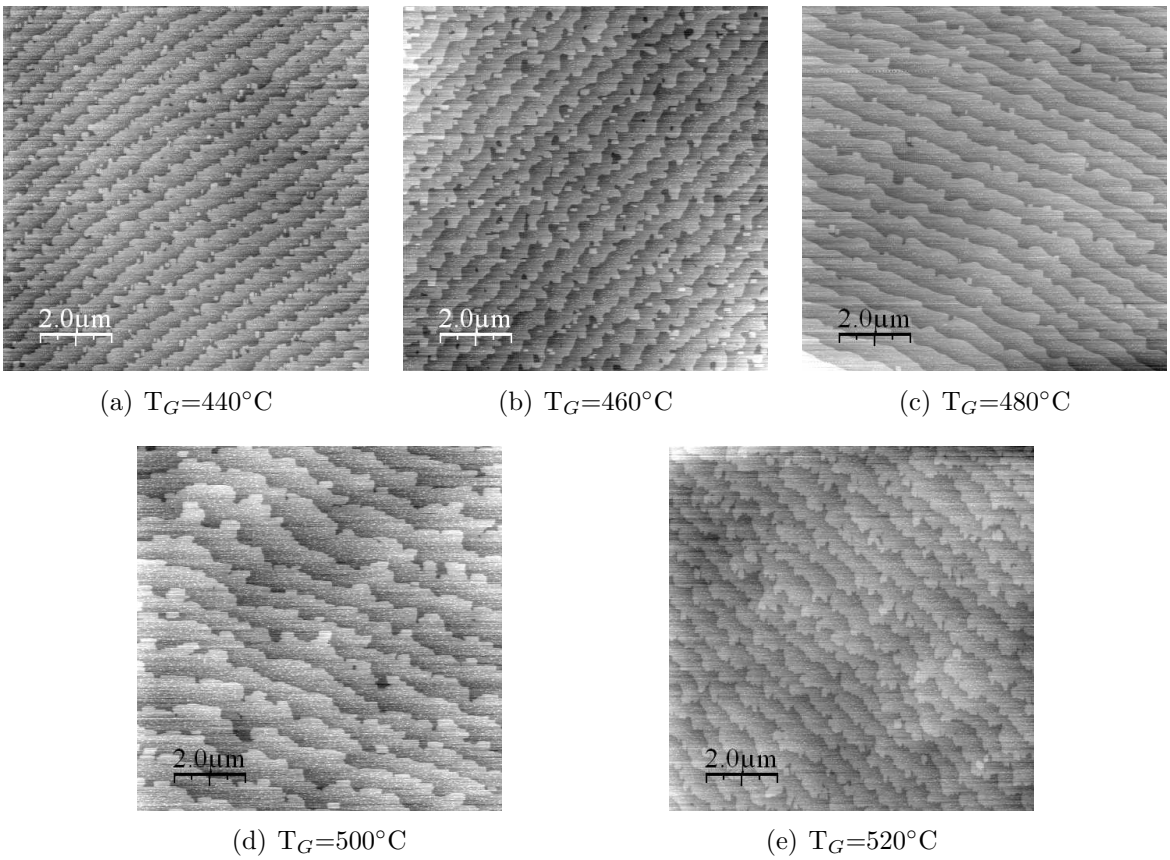

(a) T_G=440°C (b) T_G=460°C (c) T_G=480°C

(d) T_G=500°C (e) T_G=520°C

Figure 4.12: Results from samples where the anneal temperature during thermal oxide desorption was varied. Corresponding RMS roughness values and estimated oval defect densities were: (a) 1.1 Å, 1.65×10^3 cm^{-2}; (b) 1.6 Å, 3.0×10^3 cm^{-2}; (c) 1.4 Å, 3.6×10^3 cm^{-2}; (d) 1.5 Å, 3.0×10^3 cm^{-2}; (e) 1.6 Å, 3.0×10^3 cm^{-2}. The etch pit density of wafers used in this sample series was $\sim10^3$ cm^{-2}.

4.4 Conclusions

Growth of high quality nominally un-doped GaSb has been demonstrated for the application of buffer layer deposition. Oxide desorption at a temperature of 525°C for 15 minutes under antimony stabilization flux of 1.0×10^{-6} torr produced the lowest surface roughness and high optical quality. Application and termination of antimony stabilization flux must be controlled to eliminate surface damage and condensation of antimony on the wafer surface. Commencement of antimony stabilization flux at a level of 1.0×10^{-6} torr at 315°C was effective in preserving stoichiometry of the GaSb surface;

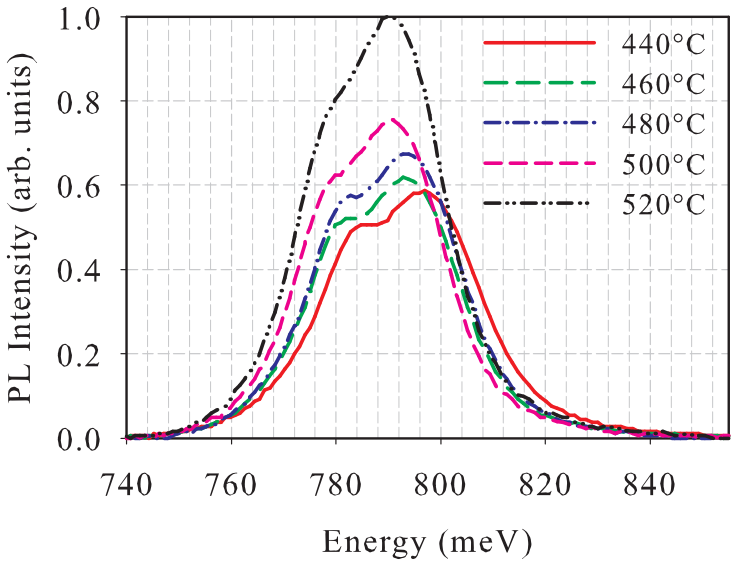

Figure 4.13: Photoluminescence of GaSb samples where the temperature during GaSb deposition was varied. Excitation was provided by a diode laser operating at 832 nm and the irradiance was ~15 W/cm^2.

terminating the stabilization flux at the same temperature resulted in no antimony condensation for a wafer cool-down ramp rate of 25°C/min.

Condensation of antimony on the wafer surface was shown to have negative effects on etching of mesa structures in GaSb. The increased sidewall roughness introduced by the antimony layer not only presents consistency issues, but may lead to a reduction in optical output in applications where smooth sidewalls are necessary. Surface antimony was also shown to eliminate photoluminescence output; a situation which may cloud results about true material quality.

High growth temperature of GaSb was shown to produce the highest optical output in GaSb at 77 K. Over the range of temperatures tested (up to 520°C) little morphological degradation was observed. Surface roughness as measured by AFM remained consistent, and oval defect levels and sizes increased only slightly at the highest temperatures.

CHAPTER 5
MID-WAVE INFRARED SUPERLATTICE LEDS

As the primary goal of this work was to develop alternative solutions for infrared scene generation technology, several criteria define the task at hand: arrays of high resolution are desired, so pixels must be readily scaled to small size; high resolution translates to high pixel density, so current consumption should be as small as possible; high apparent temperature simulation requires high optical output; high consistency is necessary. Translating to LED design, MBE-grown wafers must be of high quality and good consistency, current efficiency must be high (ideally power efficiency as well, to the degree possible), devices must emit high power and provide consistent performance. Device design issues are treated only briefly in the following, the emphasis was MBE growth of high quality material and electrical/optical characterization of test devices.

5.1 Background: Active Region Cascading

Recycling of carriers by coupling multiple active regions permits devices with high current efficiency and high output power to be realized [28, 29, 31]. Ideally, cascading N active regions has the potential to improve device output power for a given drive current by N, as carriers are transported throughout the entire device and may radiatively recombine in each stage. Deleterious effects such as absorption and nonradiative recombination often reduce this improvement factor. To first order, the improvement in output power scales as

$$P_N = P_1 \sum_{n=0}^{N-1} \exp\left[-n(\alpha_p L_p + \alpha_n L_n)\right] \tag{5.1}$$

where P_N is the output power from the N-stage device, P_1 is the single-stage output power, α_p and α_n are the absorption coefficients of the p or n side of the tunnel junction material, and L_p and L_n are the thicknesses of the corresponding sides of the junction.

Tunnel junctions considered here consisted of GaSb on the p-type side of the junction and a graded InAs/GaSb SL on the n-type side. Absorption from the p-GaSb side of the junction was calculated to be 5.5×10^3 cm^{-1} or 140 cm^{-1} for 10 μm and 4 μm radiation, respectively. From the n-type graded side of the junction, absorption was calculated to be 300cm^{-1} or 1000 cm^{-1} for 10 μm and 4 μm radiation. Assuming the p-GaSb side of the tunnel junction is 50 nm thick and the graded n-region is 45 nm thick, 16 stage devices, and employing Equation 5.1, the improvement factor was calculated to be 15.4 for a device emitting at 4 μm and 13 for a device emitting at 10 μm.

5.1.1 Tunnel Junctions

Efficient and robust cascaded active region structures require reliable, low resistance tunnel junctions. Several possibilities exist for tunnel junction design; the choice of junction depends on growth restrictions, the electronic structure of the device, and desired output characteristics. Perhaps the simplest form of tunnel junction from the design point of view is the Esaki junction, or tunnel diode [87]. In this case, both the n-type and p-type material are very heavily doped, creating a very narrow depletion region which carriers can easily tunnel through when the structure is under the appropriate bias. In order for this type of junction to work properly, doping levels must be degenerate or near degenerate (Fermi level positioned within the bands). Doping levels which do not meet this criterion produce depletion regions which are undesirably wide, thereby increasing device resistance. Unfortunately in the case where the tunnel junction layers need to be very thin, doping control becomes problematic. Structures in this study employed beryllium as the p-type dopant; this material is known to diffuse quite readily, making accurate spatial doping profiles and high doping levels difficult to achieve in thin layers [88, 89].

Tunnel junctions may also be grown with quantum structures which may lower the tunneling resistance. Quantum wells (QWs) have been effectively used in cascade

lasers, as the QW allows the designer to tailor the barrier height which carriers must pass through [90, 91]. Such structures relax the requirements on doping levels, making the performance of the device less sensitive to doping level and dopant diffusion. Tunnel junctions employed here were designed to have semi-metallic behavior at the interface, whereby the conduction band is pulled below the valence band. Compositional grading, seen in Figure 5.1(a), was used to create this effect. Use of thick InAs layers after the

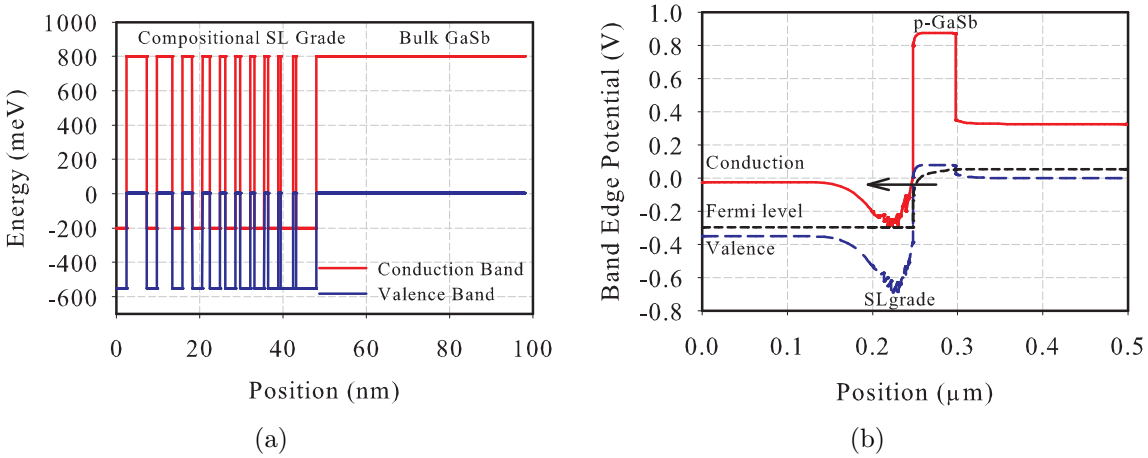

Figure 5.1: (a) Physical layout of a tunnel junction design used in MWIR cascaded structures, bulk equilibrium bands are shown. The bulk band edges are displayed for 77 K operation, showing how the compositional grade following the p-GaSb layer is implemented. (b) Simulation of the band lineup under bias, tunneling through the barrier is indicated by the arrow.

p-GaSb side of the junction facilitated pulling the conduction band below the valence band, allowing electrons to easily tunnel through the barrier. Doping at relatively high levels also helped create a thin barrier, however as in the case of QW tunnel junctions, the performance of the junction is less sensitive to doping levels than an Esaki type junction.

5.1.2 Device Efficiency Considerations

Cascaded active region LEDs have the potential to greatly increase current efficiency, and offer a straightforward approach to mating LED devices to available drive electronics. Current efficiency and quantum efficiency in such devices may improve by a factor of N, however the total power efficiency (known as wall plug efficiency) is in theory not enhanced. In practice, the effects of contact resistance on a given emission region are reduced by a factor of N; this situation may in fact increase wall plug efficiency. As one energy gap worth of bias per stage is needed in voltage overhead, the voltage drop across the device is approximately $N \times E_g$ for a cascaded active region structure. The current requirement for a given optical output power decreases by N, however the voltage requirement increases by the same factor and the power consumption remains unchanged. Although no benefit in power consumption is afforded, LEDs grown with this technology are easily driven by electronics which support large voltage swings (and voltage offsets) but have low current supply capabilities. This is often the case for high-power CMOS VLSI drive electronics supporting large format device arrays; high per-pixel current draw presents an impractical current load to the system when even a moderate fraction of pixels are illuminated. In addition to supplying power to LEDs, CMOS drivers also easily incorporate on-chip logic for pixel addressing and testing.

5.1.3 Strain and Relaxation

In order to realize an appreciable improvement in output power for MWIR and LWIR LEDs employing a cascaded active region design, several active region stages are often necessary. Ultimately, the characteristics of the drive electronics and the output power requirements dictate the number of stages which are desired in a device; in the structures considered here the number of stages for optimized devices often exceeded eight. From a material growth perspective, this presents a potential complication, as structures with large numbers of stages become exceedingly thick and epilayer strain

may become problematic. Oval defects also become larger and more numerous with increasing epilayer thickness. Typical per-stage active region thickness for LEDs considered here was 100-200 nm, combined with the tunnel junction layers this equated to devices exceeding 2.8 μm total thickness for 16 stages.

Minimization of strain in cascaded structures is best approached by considering the strain components arising in both the active region and tunnel junction. Structures employing a strictly binary-binary InAs/GaSb design may often be strain balanced by simply encouraging InSb-like interfaces and properly controlling the shutter sequence in the interface region. Such a technique remains acceptable in the limit that interface thickness values remain roughly sub-monolayer; thicker interfaces are undesirable as three-dimensional growth may occur, degrading layer morphology. Interface control may be accomplished by appropriate group V soaks at the interfaces [92, 93, 94], migration enhanced epitaxy [95, 96, 97], or conventional MBE deposition of interface material [98]. The technique used is often dictated by the requisite interface thickness, and experimental evidence as to which technique produces the highest quality material. Binary-binary InAs/GaSb SL tunnel junctions may often be strain balanced by the same technique, however interface parameters must be adjusted according to the layer stack of the junction. Depending on layer thicknesses, alternating interfaces may also be necessary.

Often in LWIR structures a binary-ternary InAs/$Ga_{1-x}In_xSb$ superlattice with x being on the order of 0.25 is used as the active material in order to help reduce the effects of Auger recombination, as well as allow the SL layers to be thinned. When incorporating such a design, the increase in lattice constant in the GaSb layer due to the indium content may overcompensate for the overall decrease in lattice constant from the InAs, leaving the epilayer with a lattice constant greater than that of the GaSb substrate. Strain may often be minimized in this case by using alternating GaAs-like and InSb-like interfaces, adjusting the interface content as required to minimize overall

strain.

5.2 Active Region Specifics

Mid-wave infrared LEDs were designed to have peak emission at 3.8 μm and a cutoff wavelength of 4.1 μm. This located the emission spectrum in the middle of the 3-5 μm band, and avoided strong carbon dioxide absorption at 4.2 μm. While there are many layer combinations of InAs and GaSb which produce a cutoff wavelength of $\sim$4 μm as shown in Table 5.1, the (nominal) InAs/GaSb 9/16ML combination was used for all

GaSb (ML)	8	9	10	11	12	13	14	15	16
InAs 7 ML	3.57	3.54	3.51	3.49	3.47	3.44	3.43	3.42	3.42
InAs 8 ML	3.99	3.96	3.94	3.93	3.93	3.90	3.90	3.90	3.87
InAs 9 ML	4.44	4.47	4.46	4.47	4.43	4.41	4.42	4.43	4.41

Table 5.1: Calculated cutoff wavelength values, given in micrometers.

MWIR samples in this work. From Table 5.1 it appears that this combination yields a cutoff wavelength of 4.4 μm, however in reality this was reduced somewhat due to some of the indium content being taken up by the interfaces. The band structure and carrier distribution of this superlattice are shown in Figure 5.2; the band structure shown was calculated at 77 K. Carrier distributions for both 77 K and room temperature are shown for comparison.

The carrier distribution comparison in Figure 5.2 immediately illustrates two important points: Auger recombination should be reduced at low temperature due to the compact carrier distribution (fewer states are available one bandgap away from the band edges); and optical emission should be enhanced at 77 K due to the large number of carriers at the band edges. Indeed the latter point is observed, as will be discussed in

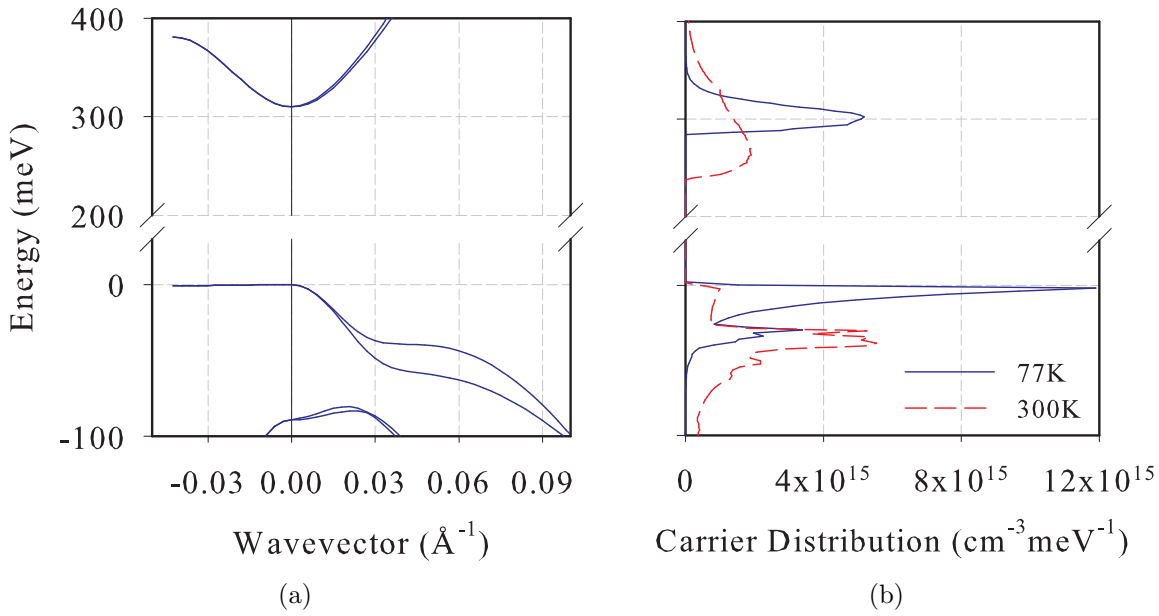

Figure 5.2: (a) Band structure for the InAs/GaSb 9/16 ML superlattice at 77 K, and (b) carrier distribution for 77 K and room temperature.

Section 5.5. Direct characterization of Auger recombination suppression is less straightforward, requiring a sample to be characterized by ultrafast optical techniques. In the absence of ultrafast measurements, some cursory observations will be made about Auger limitations on MWIR devices in Section 5.5.

5.3 MBE Growth and Optimization

Epitaxy of cascaded LED structures began in a similar fashion to the GaSb material described in Chapter 4, as the first layer grown was always a GaSb buffer layer. All growths were on quarter-2" n-GaSb wafers. Substrates were desorbed under antimony flux of $\sim 2.5\times10^{-7}$ torr, and the anneal temperature was 525°C. Heating and cooling steps were controlled in a manner to avoid antimony condensation on the wafers. The doping of the n-type substrates was as low as could be obtained from the vendor (Te $\approx 7\times10^{16}$ - 2×10^{17} cm^{-3}) in order to keep absorption to a minimum as all devices were configured

in a back-emission geometry. Due to the low doping in the substrates, the n-GaSb buffer layer was grown 1-2 μm thick and Te-doped at 1×10^{18} cm^{-3} in order to have a sufficiently thick layer with low contact resistance in which to terminate the wet etching process. Etching through the buffer layer was avoided as the lightly n-doped substrate would create a poor n-contact. For the MWIR samples considered, the GaSb growth rate was 0.55 ML/sec and V/III BEP ratio was 2.8 as measured by an ion gauge. The diagram of the overall layer structure is given in Figure 5.3.

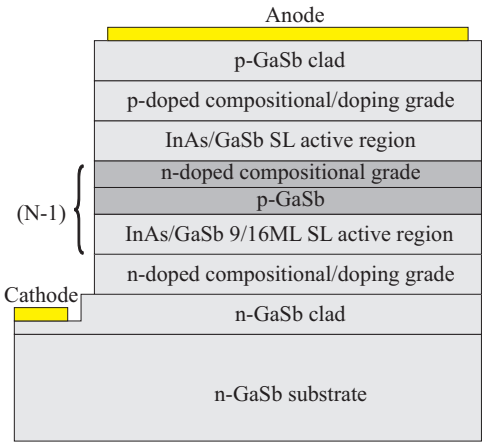

Figure 5.3: Layer stack for the MWIR cascaded LEDs.

Growth of a graded n-doped SL region followed the buffer layer. The compositional and doping grading was intended to smooth the conduction band and reduce interfacial energy spikes at the n-clad/SL interface which cause parasitic resistance. Dopant grading was performed by a linear temperature ramp of the tellurium effusion cell. The linear temperature ramp translated to an exponential change in dopant flux, as the growth control software used did not offer the capability to perform nonlinear temperature ramps. Tellurium doping was graded from 1×10^{18} cm^{-3} to 1×10^{17} cm^{-3}. Progressing from the n-clad to the SL cascade, the compositional grade was InAs/GaSb 2/16/3/16/4/16/5/16/6/16/7/16/8/16 ML; interfaces in the grade were InSb-like to compensate for strain in the InAs layers.

The emitter stack followed the n-type graded region. Active regions were nominally 27 periods of 9/16 ML InAs/GaSb yielding 200 nm thickness, with InSb-like interfaces to strain balance the structure. Light p-doping (1×10^{17} cm^{-3}) of the active region was employed for two primary reasons: improvement of the hole distribution, which suffers from the heavy effective mass and consequently lower mobility of holes; and to increase the radiative rate [99, 100]. The additional hole population was intended to reduce the lifetime of injected electrons by providing holes with which to radiatively recombine. Indium arsenide was grown at 0.17 ML/sec in order to keep the arsenic pressure in the chamber as low as possible; the valve to the arsenic cracking zone was also closed in conjunction with the shutter during growth of GaSb layers to minimize cross-contamination from the arsenic memory effect. To provide the roughly 0.8 ML of InSb-like content per period which was needed to quasi-lattice match the structures, migration enhanced epitaxy was used at the normal (InAs on GaSb) interface and antimony soaking used at the inverted interface. The timing diagram in Figure 5.4 shows how the layers were grown and interfaces formed. One monolayer of indium was deposited in migration enhanced epitaxy in conjunction with a soak of antimony to force the normal interface to be InSb-like.

Tunnel junctions were formed with a 50 nm p-GaSb layer with Be-doping of 5×10^{18} cm^{-3} and a n-type graded superlattice stack. Doping of the n-type SL stack was at 5×10^{17} cm^{-3}; the layers (going from p-GaSb to the next SL active region) were InAs/GaSb 16/2/10/2/8/3/8/3/8/4/8/4/8/6/8/8/8/12/8/16 ML. As indicated in Figure 5.3, this sequence of active layers and tunnel junctions was repeated $N-1$ times, and followed by the final active region. Strain in the tunnel junctions was again compensated with InSb-like bonds at the interfaces, using the same interface sequences as in the active regions.

To transition from the SL active regions to the p-type GaSb clad/anode, another SL graded region was used. The layer sequence going from the SL to the p-clad was

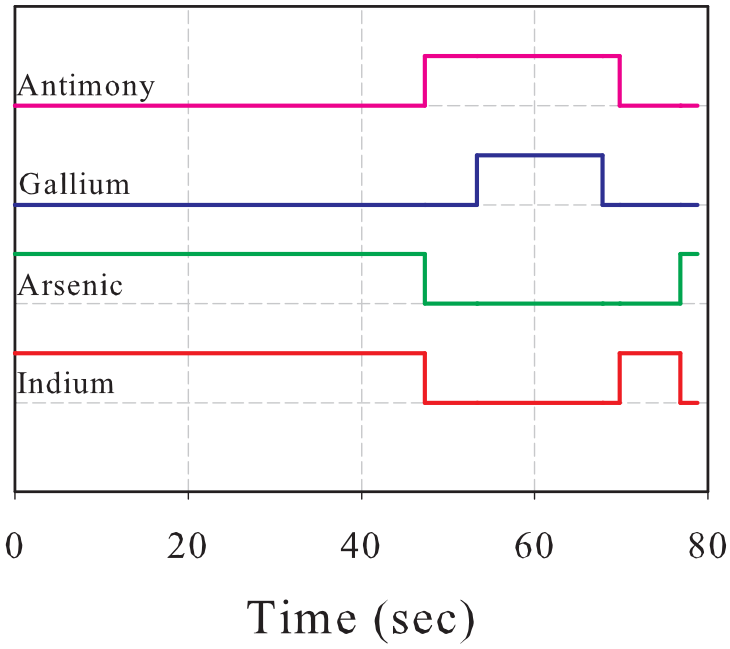

Figure 5.4: Timing diagram for one period of the InAs/GaSb 9/16 ML superlattice. Migration enhanced epitaxy formed the normal interface; antimony soaking encouraged InSb-like bonds at the inverted interface.

InAs/GaSb 8/16/8/17/8/20/5/24/2/33/2 ML; doping was graded in this region as well. Grading of the doping level from 1×10^{17} cm^{-3} to 5×10^{18} cm^{-3} in the SL stack was intended to, in conjunction with compositional grading, smooth the valence band and suppress energy spikes at the SL/p-clad interface. A 250 nm p-GaSb layer (5×10^{18} cm^{-3}) completed the devices. One detail of the device layer structure presented in this section is quite significant, especially for mesa-processed devices: the epilayers were completely aluminum-free. Since aluminum-containing compounds oxidize quite readily, it is desirable to reduce or eliminate aluminum content in semiconductor material when technologically possible.

5.3.1 Structural Characterization

The discussion of mid-wave LEDs in this work focuses on a series of four samples grown to examine the tradeoffs in active region cascading. Samples with one, four, eight, and 16 stages were grown; allowing examination and comparison of a variety of structural, morphological, electrical, and optical properties and the effects of cascading on those properties. All active regions were 200 nm thick and tunnel junctions were approximately 100 nm thick, yielding 300 nm per-stage thickness. Neglecting layers which were common to all devices, the four samples had thicknesses of 200 nm, 1.2 μm, 2.4 μm, and 4.8 μm for one, four, eight, and 16 stages, respectively. X-ray diffraction measurements for all four samples are shown in Figure 5.5; from the x-ray data several observations may be made.

Due to growth conditions for this sample series, even the single stage device showed a peak-splitting of 575 arc seconds between the substrate and zeroth order superlattice peak. After modeling the x-ray diffraction data with a dynamical fitting software package (BEDE Rads), the layer strain in the superlattice was calculated with elastic theory as described in Section 3.3. Calculation of strain for all four samples as well as the peak width (full width at half-maximum) is given in Table 5.2. As the recipe for the

Device	Strain	SL_0 Peak FWHM (arcsec)
Single	2.2×10^{-3}	73.3
Four	2.1×10^{-3}	86.3
Eight	2.2×10^{-3}	109.4
16	2.5×10^{-3}	323.2

Table 5.2: Epilayer strain and width of the zeroth order superlattice diffraction peak.

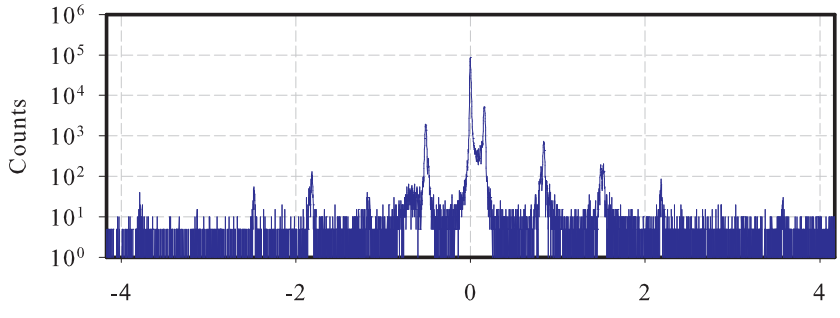

(a) Single-stage

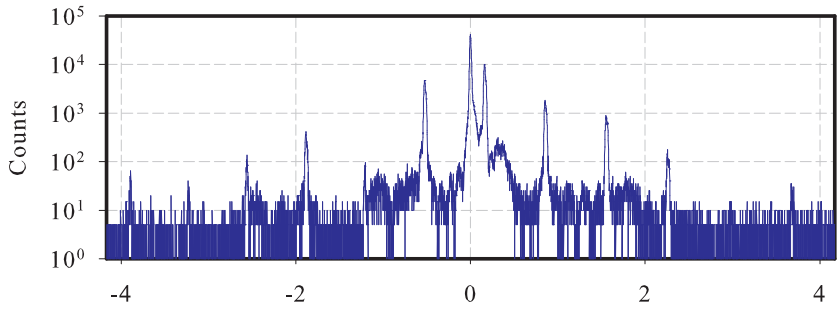

(b) 4-stage

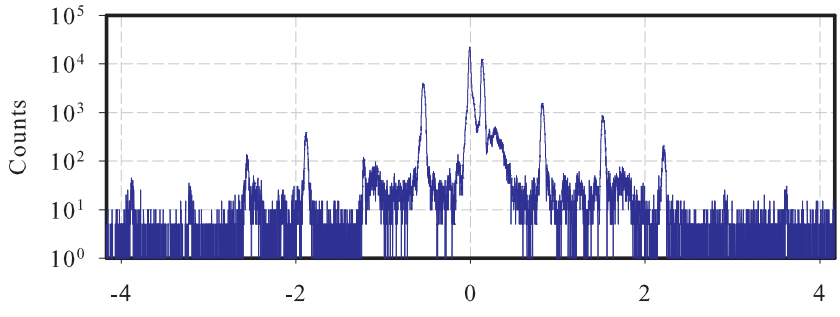

(c) 8-stage

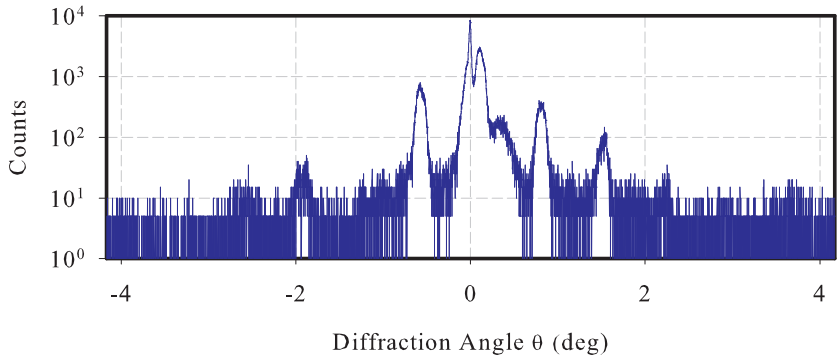

(d) 16-stage

Figure 5.5: High resolution x-ray diffraction for four LED samples with varying numbers of active region stages.

active region was the same in all cases, the strain varied little. The width of the zeroth order superlattice peak was observed to increase, as expected, with the number of stages. Broadening of the x-ray peaks indicated interfacial roughness and variations in superlattice layer thicknesses [101].

From Figure 5.5 it is apparent that the superlattice layers were in tensile strain as the superlattice zero order peak was to the right of the substrate peak. This indicated insufficient InSb-like bond content at the interfaces, which may be resolved by correcting soak times and the thickness of the layer deposited in migration enhanced epitaxy. Adjusting V/III BEP ratios also provides a potential route for modifying strain in the epilayer.

5.3.2 Defects and Morphology

Surface morphology was examined by interference microscopy and atomic force microscopy. Interference micrographs of the sample surfaces are shown in Figure 5.6; oval defects were observed on all samples with increasing size and frequency as the number of stages (device thickness) was increased. Small oval defects were 25 nm in height; large defects measured up to 160 nm in height. Large defects often appeared with "eyes" as shown in Figure 5.6(e), with the eye extending well below the sample surface. In the cases of the single, four, and eight-stage LEDs, oval defects appeared primarily as stand-alone structures. The 16-stage device, in addition to single defects, presented numerous defect clusters. Defect clusters like those shown in Figure 5.7 were attributed to the increased strain energy in the thick epilayer of the 16-stage device.

Surface roughness measurements of the cascaded LED material were made with AFM. Images of the single, four, eight, and 16-stage material are presented in Figure 5.8; the single stage device showed slight antimony condensation on the surface, which explained the high value of RMS roughness. The four and eight-stage material

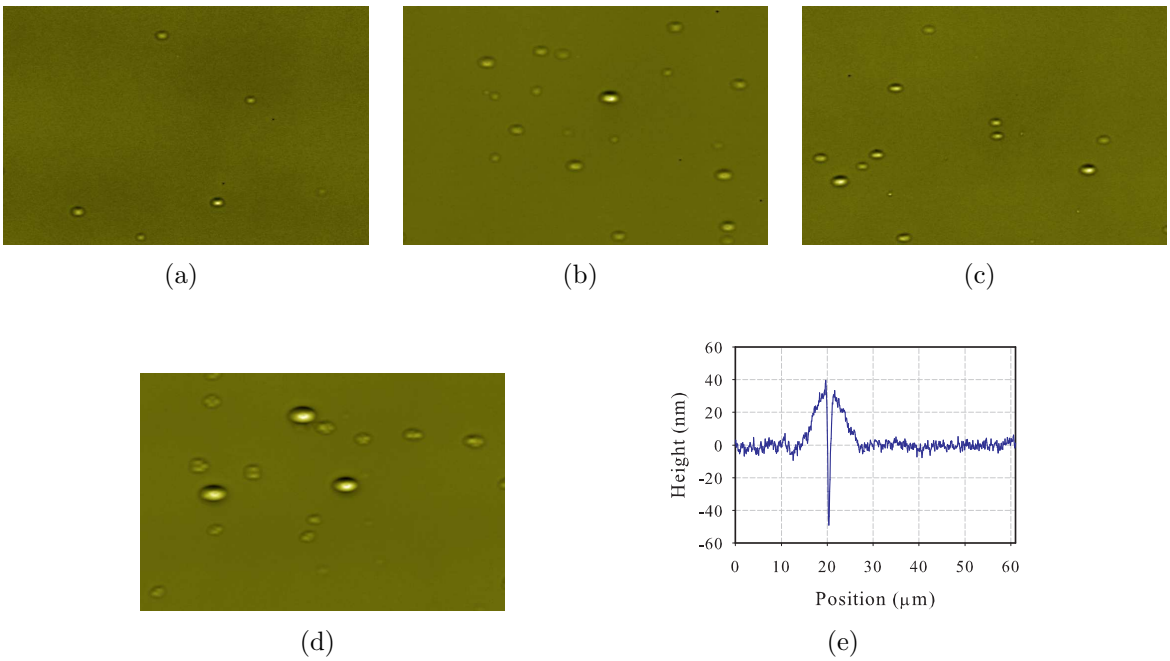

Figure 5.6: Interference micrographs of the surfaces of the cascaded LEDs: (a) single stage; (b) four stage; (c) eight stage; (d) 16 stage. Image sizes were 306×233 μm^2. (e) A line scan of an oval defect with an "eye" feature.

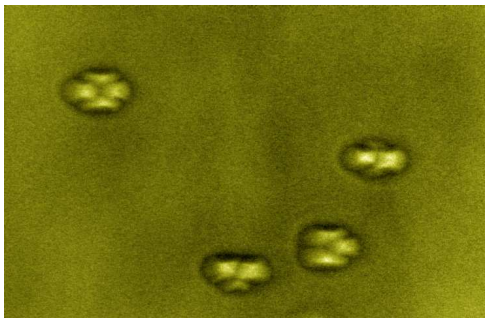

Figure 5.7: Defect clusters appearing on the 16-stage LED surface. The image area is 122×93 μm^2.

exhibited high-quality step terraced surfaces with sub-monolayer RMS roughness. Increased roughness in the 16-stage material may be attributed to the additional strain energy present in the thick epilayer. Additionally, surface degradation may arise due to increasing substrate temperature during growth of thick narrow-bandgap epilayers. Growth of narrow-bandgap materials increases absorption of radiation from the heater

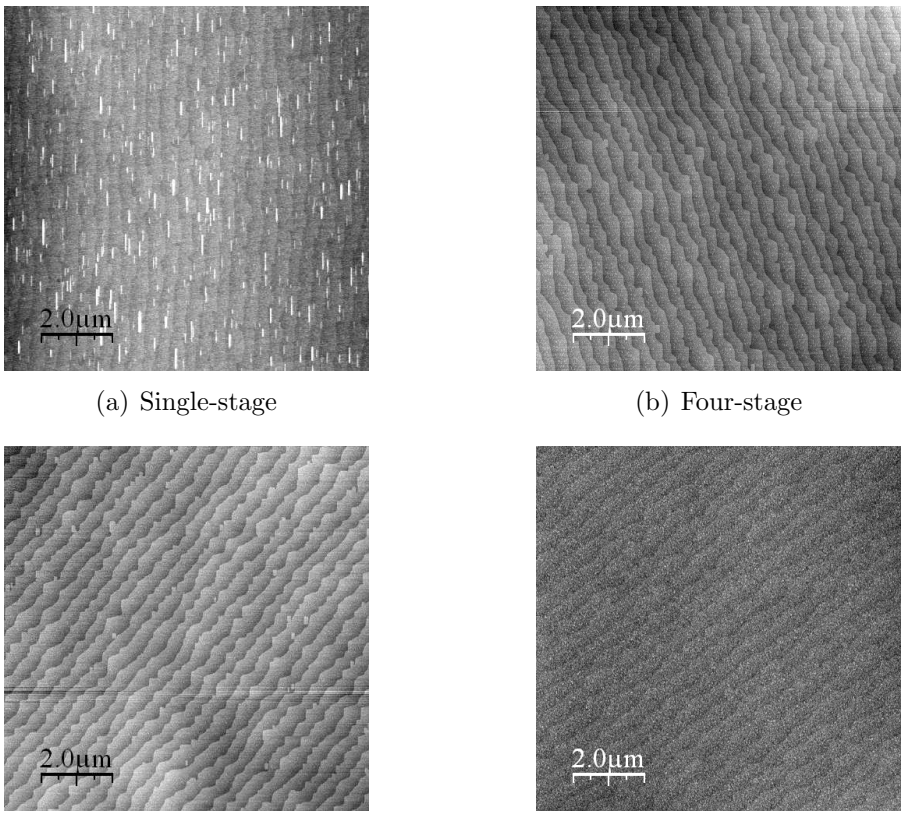

(a) Single-stage (b) Four-stage

(c) Eight-stage (d) 16-stage

Figure 5.8: Atomic force micrographs of the cascaded LED surfaces. Surface roughness values measured over a 10 μm×10 μm scan were 3.7 Å, 1.4 Å, 1.14 Å, and 3.3 Å for the single, four, eight, and 16-stage devices, respectively.

assembly; this, in conjunction with changing surface emissivity, makes measurement of the true temperature of the wafer by optical pyrometry (or transmission thermometry) difficult.

5.4 Device Fabrication

The fabrication of semiconductor wafers into useful electronic devices presents many technological hurdles and opportunities which must be assessed. As the physical and chemical properties of different material systems vary widely, device fabrication techniques often do not transfer well between material systems. Although processes and techniques can often be adapted from successful demonstrations in other materials,

substantial development is often required to duplicate a result in a novel material or device geometry. While fabrication techniques are rather mature in silicon, germanium, and gallium arsenide based devices, antimonide based devices such as those presented in this work have received comparatively little attention. For this reason it is often necessary to put forth considerable effort in developing standard processing techniques such as etching, metallization, and passivation to produce high quality devices.

Two main fabrication techniques exist for processing of LED devices: mesa processing and planar processing. Mesa diode fabrication is the process of etching a pattern in a semiconductor wafer containing an active region, thus defining the emitter area and anode and cathode contacts. The resulting LED structure is raised up like a plateau from the etched regions, thus forming the mesa. This is the simplest process; however due to the fact that the etching exposes the device active region on the mesa sidewalls, complications may arise. Having a large sidewall area exposed may give rise to layer contamination and parasitic effects such as sidewall leakage currents.

Planar processing schemes may circumvent some of the problems associated with mesa diode fabrication. In a planar process, LEDs are defined by dopant diffusion and/or ion implantation, and etching is not performed to define the emitter. Devices fabricated by planar processing have been demonstrated to have much longer lifetimes then mesa processed devices, and maintain high performance over the device lifetime [102]. Planar processing, however, requires specialized facilities and equipment, and requires extensive development for a given material system. In this work, mesa fabrication was used exclusively, however various processing methods were employed to improve the device performance and lifetime.

5.4.1 Mesa Diode Fabrication

Wafers may be processed into functional LEDs by UV photolithography and wet chemical etching techniques. All cleaning and lithography steps were carried out in a

laminar flow cleanroom. Initially samples were cleaned in solvent baths to remove as much contamination and dust as possible; this was necessary for reliability purposes, especially in devices with small feature sizes. Any particulate on the surface may lead to defects in the lithography and subsequent metallization, thereby reducing device reliability, performance, and lifetime. Cleaning in oxygen plasma was performed at various points throughout fabrication to assure the surfaces were free of any organic compounds. Photoresist was then spun onto the sample at an appropriate speed to create a given thickness of resist. Chrome-on-glass photomasks were used to define the desired pattern on the sample, and after alignment with the sample, a UV source was used to expose the sample. In this case positive photoresist was used, meaning that exposed resist dissolves in developer solution.

Chemical etching with a citric acid-based etch was then used to define the mesa structure and corresponding contacts to the cathode. Devices fabricated here were designed to emit through the substrate, with the epilayer bonded to a header to make an electrical and thermal contact. This "back emitter" configuration, depicted in Figure 5.9, keeps the epilayer as close as possible to the heat sink and allows for connections to be made by lithographically defined traces rather than individual wire-bonded connections [103]. After etching, samples were re-masked with resist for metallization by

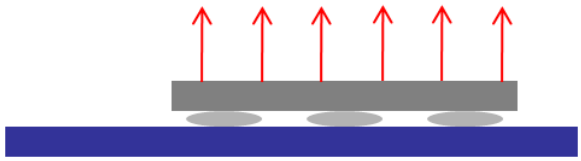

Figure 5.9: Diagram of a LED emitter chip bonded in a back-emitting or "flip-chip" configuration. Ovals represent indium or solder bumps which provide electrical contact between the LED and header/driver, and arrows indicate the direction of light emission.

e-beam evaporation. Devices were etched with HCl, and dipped in ammonium sulfide for passivation before loading into the e-beam evaporator [104, 105]. For all samples in

this work, the metal deposition for both n and p-contacts was Ti/Pt/Au. Titanium was used for adhesion purposes, and platinum provided a diffusion barrier so that gold did not intermix with the underlying GaSb [106]. While this metal recipe is known to have ohmic properties when used on p-GaSb, it does not exhibit ohmic behavior for n-GaSb. The same metal was used for both contacts due to simplicity; as additional materials and photomasks would have been necessary for depositing custom contacts for both n and p-material. The layout of a commonly used test chip is shown in Figure 5.10(a); this is shown during an intermediate stage of processing, indium metal was not deposited at that point.

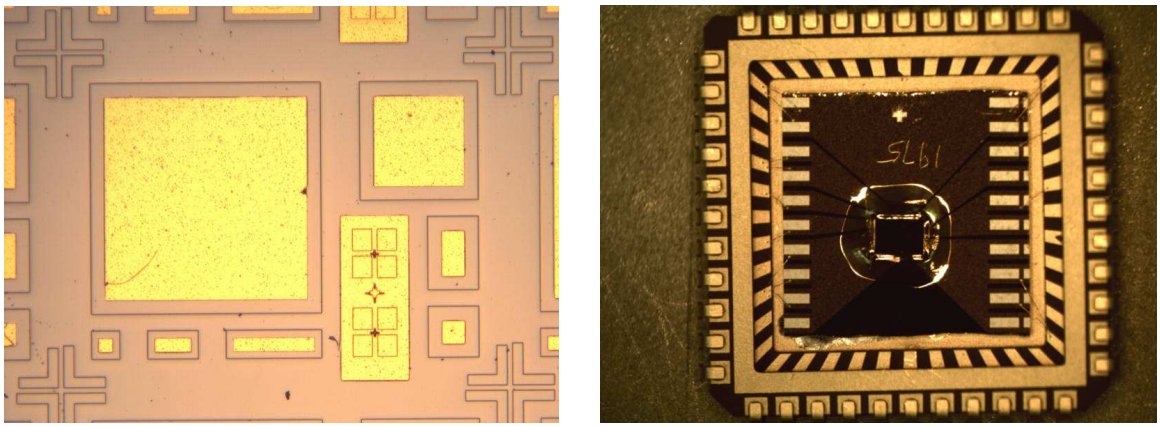

(a) (b)

Figure 5.10: (a) Variable sized mesa LED chip (unbonded); the largest mesa was 1×1 mm^2. (b) Superlattice LED device packaged in a leaded chip carrier.

In order to make contact between the LED sample and header, indium was thermally evaporated onto both pieces to aid the process of flip-chip bonding, or aligning the pieces and pressing them into contact. Flip-chip packaging also allows for fabrication of large-format arrays of devices, as the header may be a VLSI device which allows individual pixel addressing [107]. After flip-chip bonding test devices to headers, devices were indium soldered into a leadless chip carrier (LCC) package and wirebonded, as shown in Figure 5.10(b).

Epitaxially grown layers typically had thicknesses of 3 μm or greater in this work, as several active region stages were required to produce adequate output power for the intended applications. Pixel pitch may approach sizes of 48 μm in the effort to generate megapixel scenes with chip sizes to accommodate current focal plane array (FPA) detectors. Considering that the undercut of the etch in a wet etching scheme is often equal to the actual etch depth, as seen in Figure 5.11, strict limitations are imposed on etch depth in small pitch LED systems.

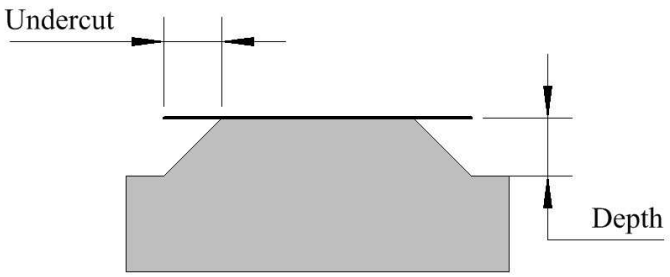

Figure 5.11: Depiction of the undercut that occurs when wet etching angled facets in semiconductor material. The gray region is the etched semiconductor and the black line represents the photoresist which masks the mesa.

5.4.2 Light Extraction Modeling

Enhancing light extraction from LEDs is of primary importance as extraction efficiency is quite low due to total internal reflection. To better understand the potential benefits to light extraction from various mesa sidewall profiles, modeling of various LED geometries was carried out by Monte Carlo ray tracing. The TracePro® software suite from Lambda Research Corporation was used for all raytracing simulations.

First considered was the simplest case of mesa sidewalls: the straight sidewall.

While this sidewall profile would only result from a dry etching process, it serves as a baseline for comparison. Sidewall profiles for straight, angled, and isotropic geometries were modeled for the case of a 44×36 μm^2 mesa; the size anticipated for large-format arrays. The three sidewall profiles are shown in Figure 5.12 in addition to the layout of the emitters within a mesa. All mesas for this set of models were configured to be

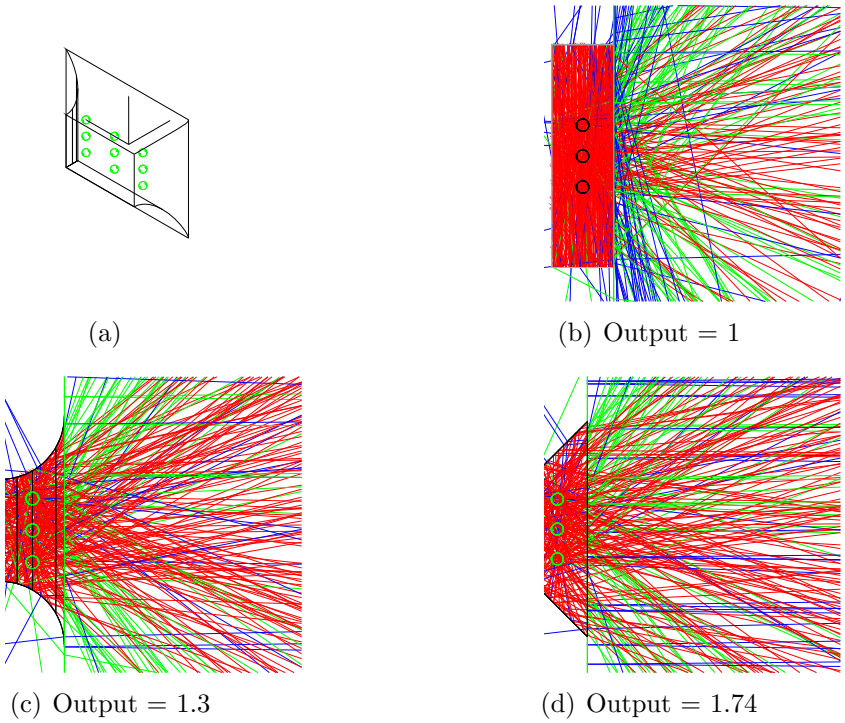

(a) (b) Output = 1

(c) Output = 1.3 (d) Output = 1.74

Figure 5.12: Geometries of various mesa sidewall profiles: (a) the emitter geometry shown in the isotropic sidewall profile; (b) straight sidewall profile; (c) isotropic sidewall profile; (d) 45° angle sidewall profile. Captions show the relative improvement in light extraction normalized to the output of the straight sidewall mesa; with the 45° angled mesa showing the most improvement.

10 μm in height, a 3×3 array of spheres within the mesa provided the ray sources. Sources were set to emit 10,000 rays each in a spherically uniform distribution. The mesas and substrate were given an index of refraction of $n = 3.8$, that of GaSb. Mesas were modeled without absorption; however the 0.5 mm thick substrate which the light propagated through was given an absorption coefficient of 5 cm^{-1}. Aside from the mesa

and substrate, the only other physical object in the model was a perfectly absorbing detection plane. In the figure, it is apparent that more rays were directed in the forward direction for the latter two cases than for the straight sidewall mesa.

The contrast between the straight sidewall mesa and the isotropic/angled sidewall mesas is intuitive: photons impinging on the isotropic or angled surfaces may Fresnel reflect toward the surface and contribute to useful emission. There is no such redirection for the straight sidewall mesa. While the isotropic sidewall profile is simple to create, etching of smooth angled facets with acceptable depth-to-undercut and proper angle is far more challenging and is the topic of future studies. Results for MWIR and LWIR LEDs presented in this work typically made use of the isotropic sidewall profile and a shallow etch; no effort was made to produce angled sidewalls.

In a separate set of models, the impact of etch depth for a 45° angled sidewall mesa with base dimensions of 120×120 μm^2 was investigated. This particular mesa size was chosen due to it's common use in samples tested in this work. Extraction efficiency as a function of etch depth is shown in Figure 5.13; clearly the deeper etch enhances the probability of a photon escaping the device. Absent from this set of models is the impact of reduced emitter volume resulting from the deeper etch. While this loss of emitting material is certainly of consequence for device performance, the goal here was simply to illustrate geometrical advantages for various etch profiles and depths.

5.5 Electrical and Optical Characteristics: Quasi-DC Results

Electronic and optical characterization of packaged LEDs was carried out under two primary excitation conditions: quasi-DC and pulsed. Quasi-DC excitation refers essentially to low-frequency square wave excitation; typically 500 Hz-1 kHz with 50% duty cycle. In regard to output power, quasi-DC excitation is similar to true direct-current excitation in that the average power dissipated in the device remains high and

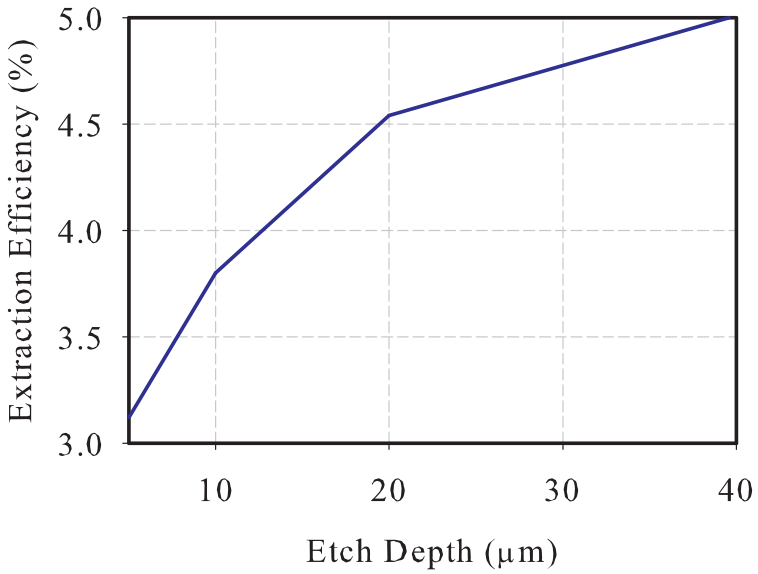

Figure 5.13: Effect of etch depth on light extraction efficiency for a 120×120 μm^2 mesa with 45° angled sidewalls. While clearly more light escaped the device as etch depth increases, the loss of emitter volume was not taken into account in this calculation.

thermal loading is similar to DC. Short-pulsed excitation, on the other hand, presents an operating regime where the average power dissipated in the device is negligible; the duty cycle is low in order to suppress thermal loading and increase peak output power.

Output power was measured with a 4 mm-diameter, LN_2-cooled InSb detector which was positioned 60 mm from the device under test (DUT). Devices were mounted in a pour-fill LN_2 cryostat for variable temperature measurements; no collection optics were used in any of the measurements presented here. From the voltage measured on the InSb detector, the power on the detector was calculated by

$$P_{d,meas} = \frac{V_d}{R_d r_{rel} g_d}, \tag{5.2}$$

where $P_{d,meas}$ is the power measured by the detector, V_d is the detector voltage, R_d is the detector peak responsivity (A/W), r_{rel} is the relative responsivity, and g_d is the detector gain in Ω. Voltage on the detector was measured either directly by an oscilloscope, or

by lock-in detection. When lock-in detection was used, appropriate correction factors to the voltage were included to account for the fact that the lock-in reading yields the RMS value of the first Fourier harmonic of the periodic input signal. Reflections from cryostat windows and any filters may be accounted for by

$$P_d = \frac{P_{d,meas}}{T_{win}T_{filter}} \tag{5.3}$$

where T_{win} and T_{filter} are the transmission coefficients of the cryostat window and filters, respectively. This gives the power incident on the detector element, from which the full upper hemisphere power may be calculated if the emission distribution of the LED is known. For an active region emitting with a uniform distribution and propagating out of a dielectric into a medium with a lower index of refraction, as in the case of a back-emitting LED where light is collected through the substrate, the emission distribution is known to be Lambertian (a $\cos(\theta)$ pattern). Room temperature measurement of the output distribution of a 16-stage LED yielded a near-perfect Lambertian pattern as shown in Figure 5.14. Although measurement of the emission pattern was not possible at low temperature due to limited field of view in the cryostat, the Lambertian distribution was assumed to hold over all temperatures considered. Calculation of the full upper hemisphere power for a device with a Lambertian emission pattern simply takes into account a correction factor for the fraction of light collected on the detector;

$$P_{total} = \frac{P_d}{2[1 - cos(\theta_c)]} \tag{5.4}$$

where θ_c is the collection angle subtended by the detector, or $\theta_c = tan^{-1}(r_d/l_d)$ with r_d the detector radius and l_d the sample-to-detector distance.

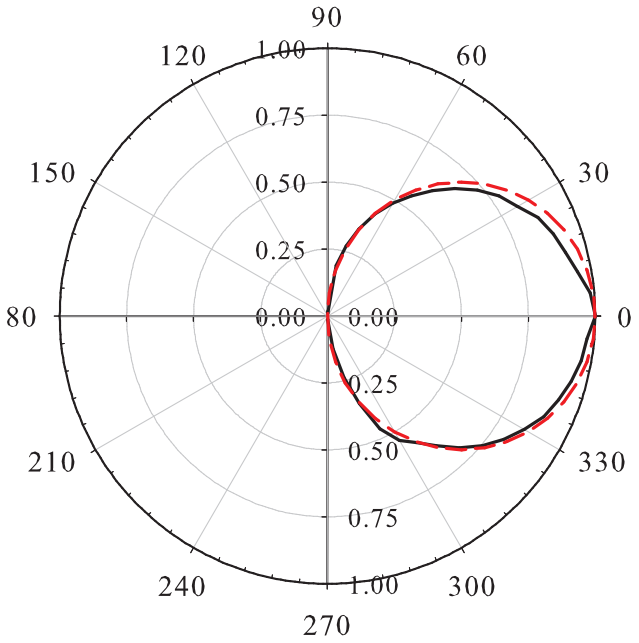

Figure 5.14: Output distribution of a 16-stage LED at room temperature. The emission pattern (solid line) was nearly Lambertian as expected for a mesa LED without additional fabrication for enhanced light extraction. A $\cos(\theta)$ distribution (dashed line) is shown for reference.

5.5.1 Temperature Dependence of MWIR LED Performance

Device performance as a function of temperature was of significant interest for thermal scene generation applications, as achieving high output power is desirable for high apparent temperature generation. Although room temperature operation would be ideal, the power produced from small pixel LEDs in the MWIR and LWIR at room temperature is insufficient for the application. Variable temperature measurements were performed on the eight-stage cascaded LED device to determine output power from room temperature to 77 K. While still lower temperature would have yielded higher power, temperatures lower than 77 K for scene generator technology are unrealistic. Operating at 77 K with large arrays is a technological hurdle in and of itself.

Both light-current-voltage (LIV) characteristics and electroluminescence (EL) emission spectra were collected over a range of temperatures for the eight-stage LED. As shown in Figure 5.15(b), the output power increased by approximately a factor of 15 going from room temperature to 77 K. Over this temperature range, the peak of the emission spectrum shifted by 0.33 μm as indicated in Figure 5.15(a). Similar temperature scaling results have been observed in 16-stage material as well [108]. The quenching of optical output with sample temperature is shown in Figure 5.16; output power and apparent temperature were normalized to the maximum values at 77 K. This is an opportune point to further emphasize the importance of thermal management of LEDs and the impact on output power. Three different interfaces between the ceramic package housing a MWIR LED chip and the cold finger of the cryo cooler were tested to assess the impact on performance. Indium foil, sample on bare gold (no intermediate layer), and 0.1 mm thick paper were used as the interfaces between the sample package and cold finger. The same sample was cooled to 77 K and allowed to thermally equilibrate for 10 min for each of the three tests. As shown in Figure 5.17 the interface had a dramatic impact on LED output. A factor of four decrease in output occurred when the indium foil was replaced with a thin insulator. As indium is a soft metal the indium foil layer easily conformed to the cold finger and sample package, creating a low thermal impedance, high surface area contact and hence was able to quickly remove heat from the LED. The insulating layer, naturally, had a high thermal impedance and the LED had insufficient heat sinking. From these results it was clear that optical output and consistency in device testing were strongly dependent on thermal management.

Apparent temperature, integrated from 3-5 μm, showed a less drastic dependence on sample temperature, as the relationship between output power and apparent temperature is nonlinear. A three-parameter power-law fit to the plot of apparent temperature as a function of axial LED power yields the approximation

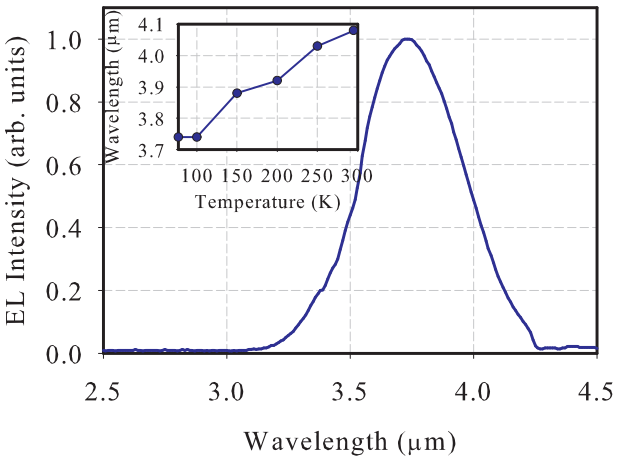

(a)

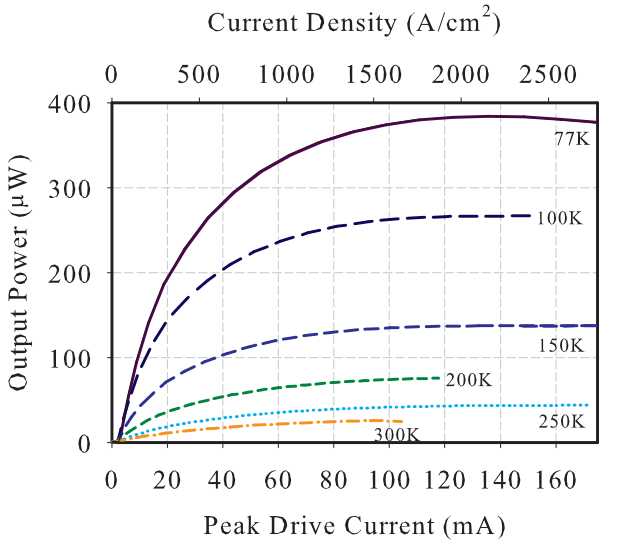

(b)

Figure 5.15: (a) Emission spectrum taken at 77 K and temperature dependence of the emission peak (inset). (b) Light-current curves over a range of temperatures for a 80×80 μm^2 mesa. The improvement factor in optical output from room temperature to 77 K was 15. All measurements were made under quasi-DC biasing conditions.

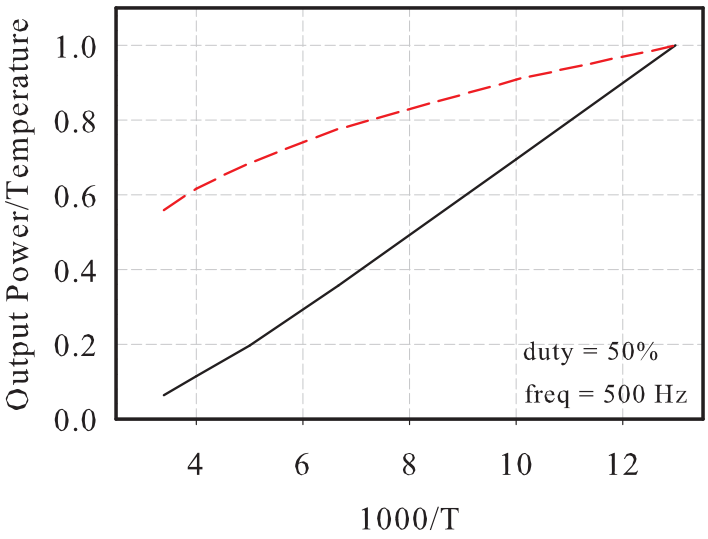

Figure 5.16: Variation in optical output with sample temperature. Measurements were taken under quasi-DC biasing conditions. While output power increased nearly linearly as a function of inverse temperature (solid line), apparent temperature (dashed line) had a less marked dependence on temperature.

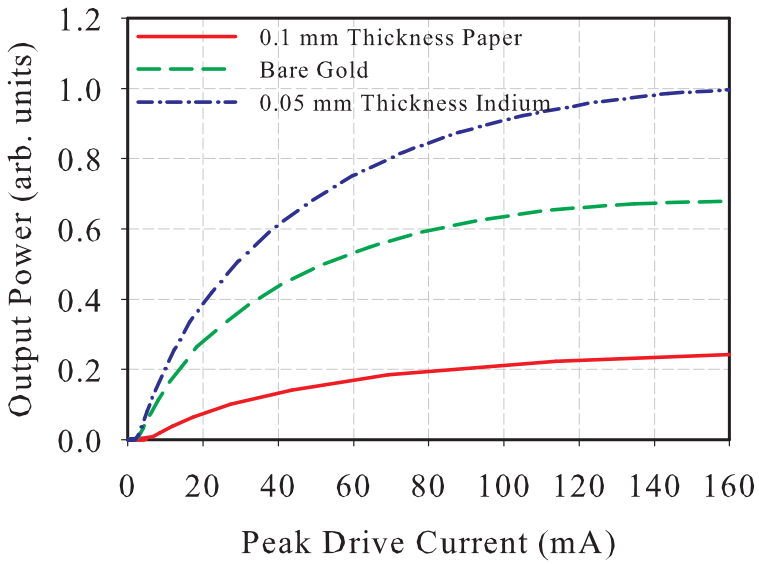

Figure 5.17: Effects of the thermal interface between the ceramic package and cold finger on the cryo cooler. Optical output decreased by approximately a factor of four by replacing the indium foil with a thin insulator.

$$T_{app} = 628.5 + 17.6P^{0.661} \tag{5.5}$$

where T_{app} is the apparent temperature in kelvin and P is the axial LED output power (μW/sr); this approximation loses validity in the very low power regime.

5.5.2 Performance of Cascaded LEDs

Electrical and optical characterization from the series of four cascaded samples is presented in the following. All data were taken under quasi-DC biasing conditions and at 77 K, and all mesas tested were 120×120 μm^2 in size. Output characteristics are shown in Figure 5.18. The turn-on voltages scaled as expected; approximately $N \times E_g$ volts were required for conduction to begin in the diodes. Output power scaling was favorable, especially considering the high degree of strain and x-ray peak broadening in the thicker cascaded samples. The 16-stage sample showed nearly a factor of 14 improvement from the single stage device, however as will be discussed below this was partly attributed to Joule heating in the single stage device [109].

Further investigation of the output characteristics yields two points of interest. First, as seen in Figure 5.19(a), the per-stage output power below 120 mA input current was lowest for the single stage device. On the other hand, the four-stage device had the highest per-stage output power, with eight and 16-stage devices exhibiting decreased per-stage power. Joule heating from the n-GaSb contact was suspected responsible for the low per-stage output of the single-stage device. While the cascaded samples benefited from the effects of contact resistance being effectively reduced by the number of stages, this was not the case for the single stage device. Wallplug efficiency calculations seemed to confirm this explanation. The wallplug efficiencies (ratio of output optical power to input electrical power) for the cascaded samples were nearly identical over the range of drive currents tested, while the wallplug efficiency of the single stage device was approximately a factor of three lower as shown in Figure 5.19(b).

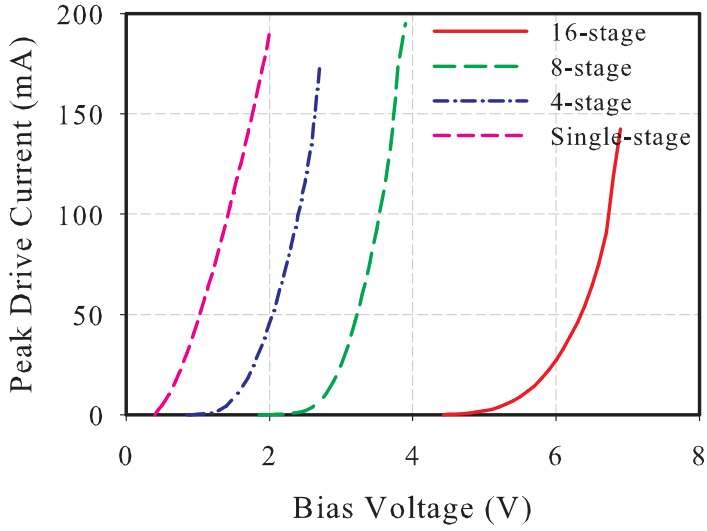

(a)

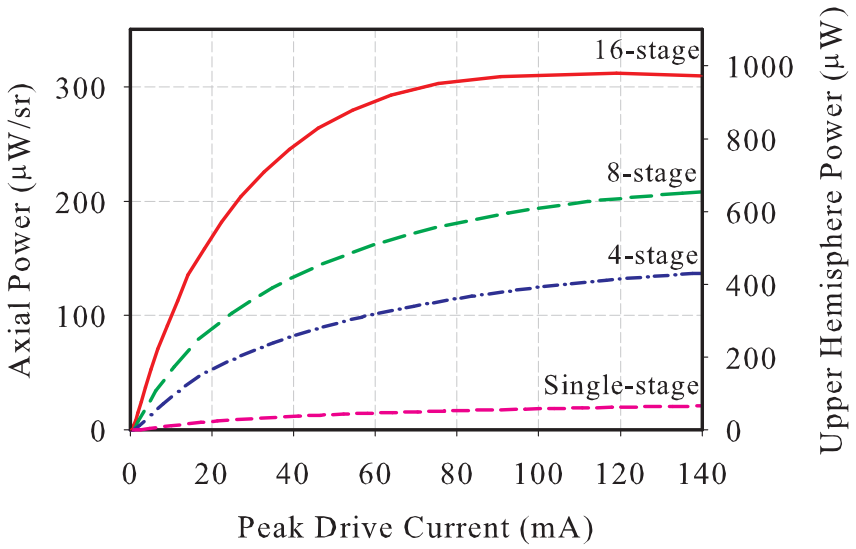

(b)

Figure 5.18: Current-voltage and light-current output characteristics of the series of cascaded LEDs. From the I-V characteristics, the on-resistance of the LEDs was calculated to be ∼7 Ω for all devices.

Second, neglecting the single stage device, per-stage output decreased with number of stages. This was attributed to defect formation and structural degradation as device thickness increased. The high degree of strain (2.5×10^{-3} for the 16-stage device)

was responsible for reduced structural quality with increasing epilayer thickness. This demonstrated a direct correlation of decreasing per-stage power with increasing x-ray peak width, indicating a strong dependence on structural quality. From Figure 5.19(a) one may observe that, if strain were minimized and structural degradation eliminated, the 16-stage device may be expected to emit nearly 1.7 mW if the per-stage output matched that of the four-stage device.

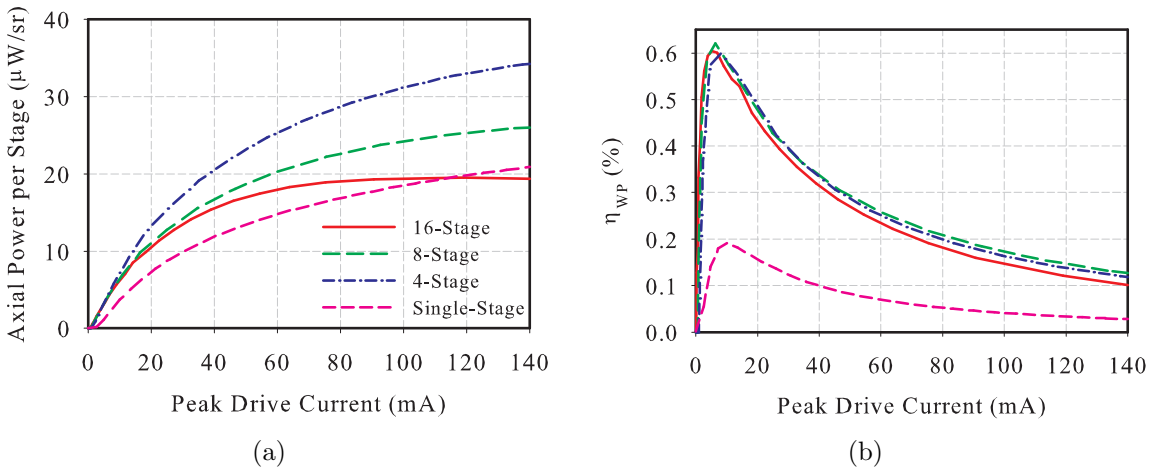

Figure 5.19: (a) Per-stage optical output and (b) wallplug efficiencies of cascaded LEDs. The plot legend in (a) applies to both sub figures.

Despite structural limitations with this sample series, high external quantum efficiency was measured for the cascaded LEDs. External quantum efficiency is the ratio of number of photons measured over number of injected electrons:

$$\eta_{EQ} = \frac{N_p}{N_{e^-}} = \frac{P_{LED} q_{e^-}}{E_p I_i} \tag{5.6}$$

where P_{LED} is the output power of the LED, q_{e^-} is the electron charge, E_p is the photon energy, and I_i is the injected current. Peak quantum efficiency of nearly 10% was measured for the 16-stage LED, in contrast to only 0.4% for the single stage device.

Due to the fact that each injected carrier may generate multiple photons in cascaded devices, the quantum efficiencies increased with the number of stages. Cascaded devices also require roughly a bandgap of bias voltage per active region to operate. This increase in operating voltage typically negates any improvement in wallplug efficiency, save the (potential) improvement from reduced contact resistance as observed here.

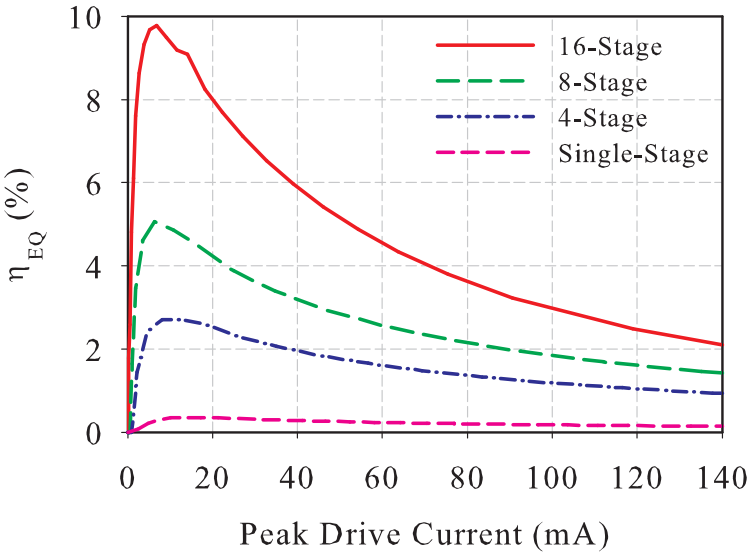

Figure 5.20: External quantum efficiency of cascaded LED samples at 77 K.

A point warranting further consideration for the MWIR LEDs is the roll-over behavior of the LI curves shown in Figure 5.18(b) and Figure 5.15(b). The output power appears to saturate, and in some cases, decrease at high drive current. While simple Auger recombination arguments would explain sublinear behavior of the LI curves (optical output $\propto I^{2/3}$ in the Auger limit), this cannot explain the saturation and subsequent decrease in optical output. Joule heating of the active regions at high current is one likely component of the saturation in optical power. Also likely is carrier leakage out of the structure due to weak confinement in the valence band. Active region heating is likely to blame when a decrease in output is observed, however carrier leakage becomes suspect when the output clamps at a given value over a range of injection current.

Perhaps the most useful figure of merit for the small pixels considered here (as applicable to scene generation) is the apparent temperature. Apparent temperature curves for the MWIR LEDs are shown in Figure 5.21, with values exceeding 1400 K for the 16-stage device. These curves represent the single-pixel apparent temperatures, as no fill factor was taken into account. If a 50% fill factor were taken into account the apparent temperature drop would only be about 20%, despite a 50% reduction in light intensity. These results compared favorably with results demonstrated for interband cascade LEDs of similar size [43].

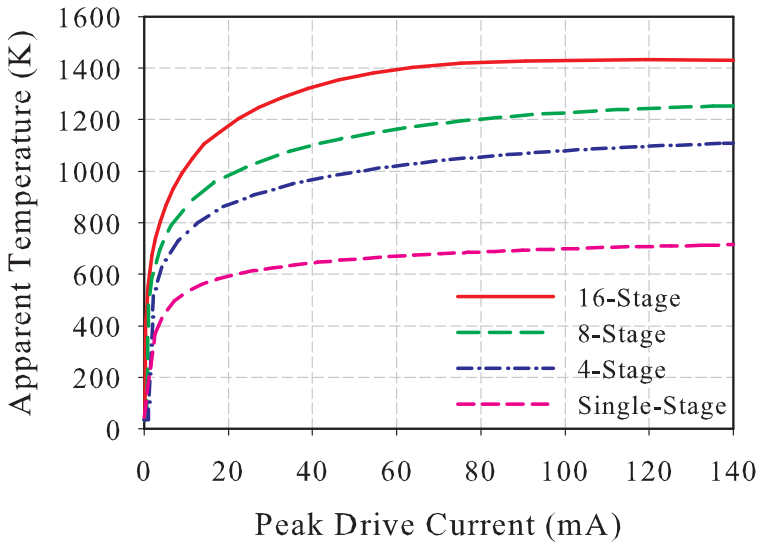

Figure 5.21: Calculated single-pixel apparent temperature as a function of current for the series of cascaded LEDs. The integration limits for the apparent temperature calculation were 3-5 μm and the pixel area was taken as the device area.

Another important figure of merit for arrays is frame rate: the speed at which the emitting array can change the image being displayed. This is governed by the rise and fall times of the pixels, typically defined as the transition times between the 10% and 90% amplitude levels of an optical pulse. Diffusion and junction capacitance, along with capacitance from the metal-semiconductor interface and device package are the

limiting factors of LED speed. Series resistance in the LED and driving system also limit transition times by increasing the RC time constant. Once the rise and fall times are known, the (half-power) bandwidth of the emitter may be determined by

$$f_{-3dB} = \frac{1.2}{(\tau_r + \tau_f)}, \tag{5.7}$$

where τ_r and τ_f are the rise and fall times, respectively. Rise and fall times were measured for several mesa sizes in order to ascertain the LED bandwidth. The optical pulse shown in Figure 5.22 was taken for a 80×80 μm^2 mesa at 77 K; the bandwidth calculated from the listed transition times was 600 kHz. Transition time measurements were also made

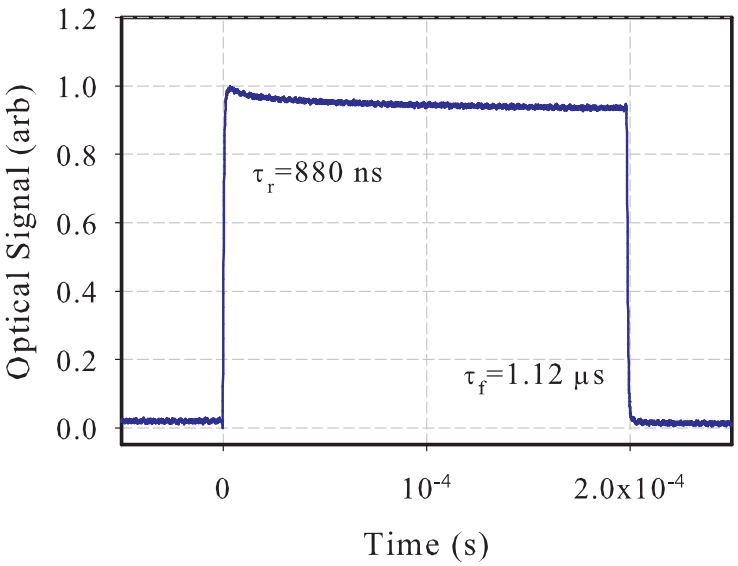

Figure 5.22: Rise and fall time measurements of the optical pulse from a 80×80 μm^2 mesa.

for mesas with sizes up to 520×520 μm^2; neither rise nor fall times increased beyond 1.1 μs, and little variation was observed. Negligible difference in transition times between mesas of greatly differing area indicated that the detector response time was the limiting factor; the LEDs likely operate faster than the measured 600 kHz bandwidth. The InSb

detector used to take the transition time measurements had a 4 mm diameter active area and a high gain transimpedance amplifier; neither of which are accommodating to high speed measurements.

5.5.3 Mesa Size Dependence and High Power Emitters

Cascaded device characteristics were examined further by comparing devices of varying size. The 16-stage device presented in the previous section was tested under quasi-DC conditions, with the same set of assumptions about the output distribution taken into account. Current-voltage and light-current characteristics at 77 K are shown in Figure 5.23; nearly 25 mW of power was measured from the 1×1 mm^2 device [110].

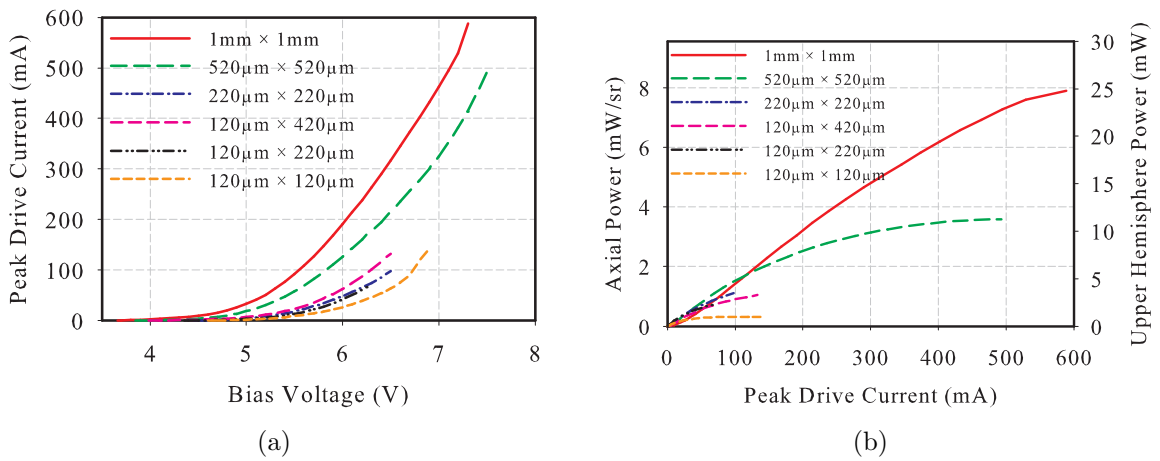

Figure 5.23: Current-voltage and light-current characteristics for various mesa sizes from 120×120 μm^2 to 1×1 mm^2. All data were taken under quasi-DC biasing conditions at 77 K.

To better understand the mesa size dependence of the output power, and the limitations on the devices, light output as a function of mesa length and light density as a function of current density were considered. For this sample, maximum output power scaled linearly with mesa length as shown in Figure 5.24(a); as opposed to the expected linear scaling with mesa *area*. Plots of power density as a function of current

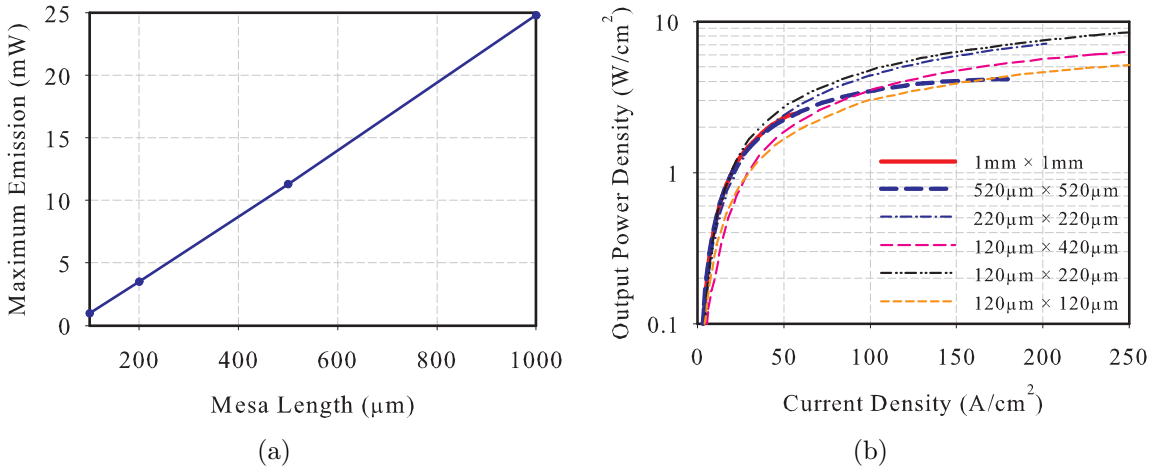

Figure 5.24: Dependence of maximum output power on mesa length (a) and light output density (W/cm^2) as a function of input current density. In (b), two distinct operating regimes were observed for small and large mesas.

density in Figure 5.24(b) offer an explanation of the observed power scaling with mesa length. While the largest mesas (1×1 mm^2 and 520×520 μm^2) were observed to approach saturation by 100 A/cm^2, the power density of the smaller mesas did not fully saturate over the range of drive currents applied. At the highest injection currents, in excess of 4.3 W of power was dissipated in the large mesas. Device heating was likely to blame for the saturation of the large mesas; thermal loading due to packaging of the device, and local heating posed limitations to performance. Joule heating undoubtedly impacted the smaller mesas; however carrier leakage and Auger recombination become important factors due to high current density.

Mid-wave infrared sources are of interest for spectroscopy and process monitoring applications, however operation at 77 K is not practical or economical for the majority of situations. Output power from a 16-stage 520×520 μm^2 mesa was measured at room temperature and 220 K to demonstrate high power at practical operating temperatures. Thermoelectric cooling modules readily achieve 220 K temperature, making packaging and operating devices at that temperature relatively economical. Light-current curves

for 220 K and 295 K are shown in Figure 5.25; 1 mW of upper hemisphere output was produced at 300 mA drive current, and 1.4 mW at 600 mA.

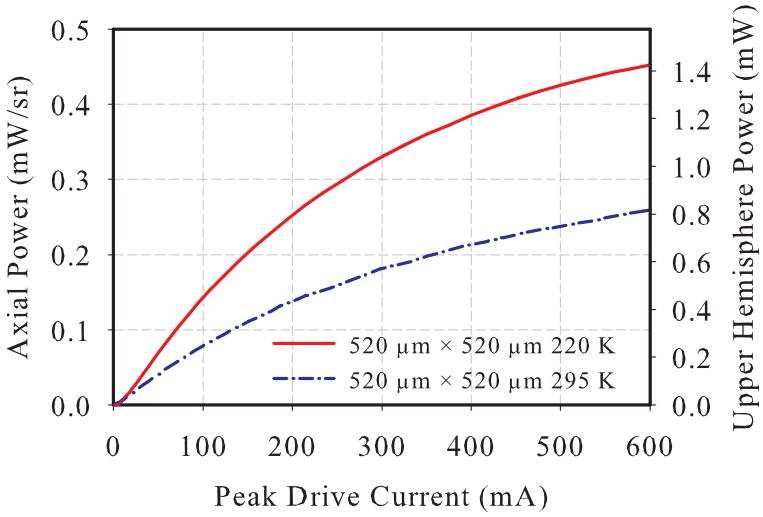

Figure 5.25: Room temperature and 220 K output power of a 520×520 μm^2 mesa under quasi-DC excitation.

Growth optimization and improvements in device packaging yielded improved 16-stage device performance. By reducing strain to 1.4×10^{-3} and thinning the epilayer by reducing per-stage active region thicknesses to 100 nm, improved material quality was obtained. Sample mounting and packaging within the cryostat (coupling all thermal interfaces with indium foil, for instance) also contributed to improved output. Several mesa sizes were tested, and the light-current curves are shown in Figure 5.26. Output power for the 120×120 μm^2 mesa exceeded 2.5 mW at 77 K, corresponding to a single-pixel apparent temperature of nearly 2100 K. Adding a 50% fill factor to the calculation yielded roughly 1600 K. Power yielded from the 1×1 mm^2 mesa increased somewhat, however as discussed previously the high input power likely limited performance at high current.

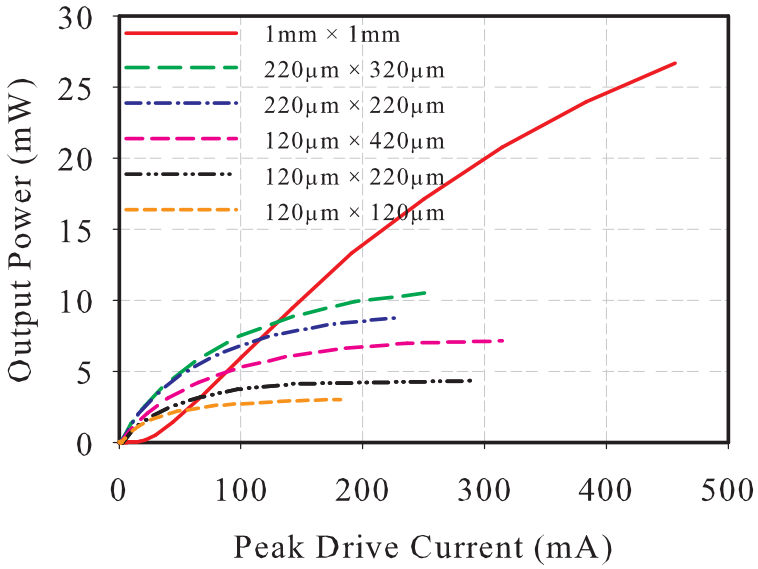

Figure 5.26: Results from a better optimized 16-stage LED. Improved growth conditions and thermal management contributed to higher output power.

5.6 Projection of MWIR Device Performance in Arrays

All LED devices presented in this work have been 80×80 μm^2 in area or larger; of application only to small test arrays or single pixel emitters. While these devices have yielded a great volume of interesting results, substantial interest remains in applying these materials in large format emitter arrays. Although the facilities to fabricate and test such high resolution optical systems were not available for this work, the results presented here can be used to project how the materials might perform in such a system. Taking the scaling of the peak output power as a function of mesa area for the smallest three mesas from the LI curves in Figure 5.26, and projecting from the smallest mesa to zero yields the plot in Figure 5.27. This result allows an estimation of the output power from a mesa 30×30 μm^2 in area, which would be applicable for an array with pitch of 48 μm. The output power from the 30×30 μm^2 mesa was estimated to be approximately 200 μW, corresponding to an apparent temperature of 1600 K if full-band integration is

used (3-5 μm). In the following are two potential routes to increase apparent temperature, one via improving output power and one via consideration of the output spectrum and spectral integration. These potential improvements were treated independently for clarity; no cumulative improvement is shown. Holding the array pitch constant, and assuming an improvement factor of 1.74 from angled sidewalls as calculated in Section 5.4.2 yields an output power of nearly 350 μW, the improvement in apparent temperature is shown in Figure 5.28. Projections thus indicate that apparent temperatures approaching 2000 K should be achievable with MWIR LEDs in high resolution array format, with the integration limits of the apparent temperature calculation extending over the entire 3-5 μm spectral band. Additional improvements from both material growth and device processing are also expected to improve upon the above apparent temperature figure.

Another variable in the apparent temperature calculation which warrants attention is the limit of spectral integration. While integration over the entire MWIR band from 3-5 μm may be appropriate for broadband emitters such as thermal pixels, narrowing the integration limits may be beneficial for systems incorporating LED emitters. The MWIR emitters described in the previous sections have half-maximum bandwidths on the order of only 0.5 μm; integrating over the entire 2 μm wide spectral band does not represent the highest achievable apparent temperature. The peak radiance of the LEDs is typically substantially higher than the radiance of a blackbody in the MWIR, therefore narrowing the integration limits allows observation of higher temperature scenes. The physical analog of narrowing the integration limits is placing a bandpass filter between the emitter array and detector/camera. Narrowing the passband of the filter (centered around the peak emission wavelength of the LED) yields a higher apparent temperature. This effect is depicted in Figure 5.29, where the entire integrated output of the LED was fixed at 200 μW. For this calculation the output spectrum of the LED was approximated by a Gaussian distribution; only the fraction of the output power that fell within the integration limits was applied to the apparent temperature calculation.

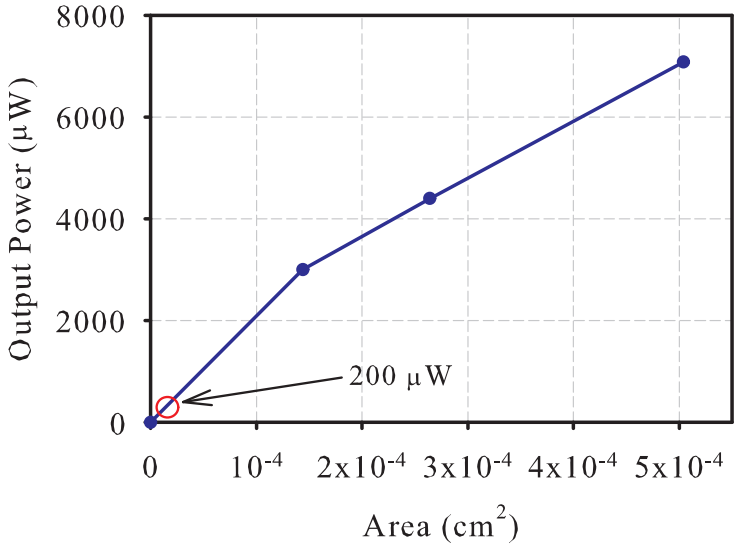

Figure 5.27: Scaling of peak upper hemisphere output power with mesa area. The output power from the smallest tested mesa was projected to zero to allow extrapolation to smaller devices.

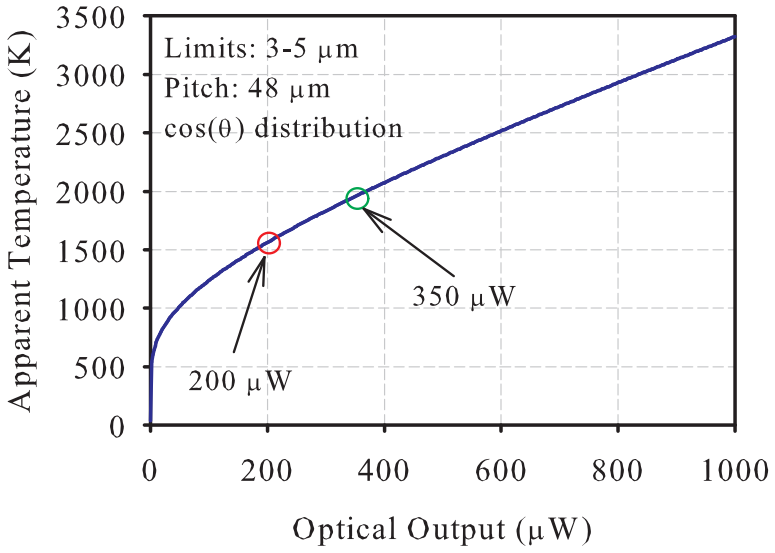

Figure 5.28: Scaling of apparent temperature with potential improvement from angled sidewalls. The improvement factor of 1.74 yields power output of nearly 350 μW, translating to approximately 2000 K.

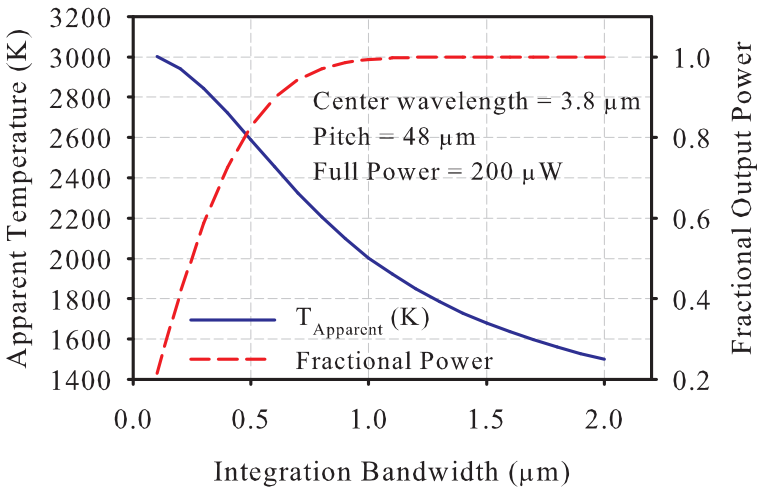

Figure 5.29: The effect of detection bandwidth (spectral integration limits) on apparent temperature.

Clearly, narrowing the spectral window observed by the detector around the peak of the LED spectrum allows for significantly increased apparent temperature.

The results of this section suggest that single-pixel apparent temperatures approaching 3000 K may be achievable with current materials configured in arrays with 48 μm pitch, and yet higher temperatures should be possible with growth and fabrication optimization. Deleterious effects such as heating from adjacent pixels and the thermal impedance of the driver chip were not included in the calculations presented here. This being the case, the actual apparent temperature produced in high resolution arrays with large groups of pixels illuminated will likely decrease from the values in Figure 5.29. Quite likely it will be necessary to incorporate any and all improvements to the LEDs to achieve apparent temperatures of few thousands of kelvin in functional arrays.

5.7 Conclusions

Mid-wave LEDs of various mesa sizes emitting at 3.8 μm at 77 K were grown by molecular beam epitaxy and examined under a variety of conditions. Active region cascading was shown to substantially increase output power and current efficiency, with

the former showing improvement by a factor of nearly 16 and the latter by a factor of 29 when comparing single and 16-stage devices. Wallplug efficiency was improved in the cascaded LEDs due to the decreased impact of contact resistance as compared to the single-stage device; wallplug efficiencies varied only slightly between four, eight, and 16-stage devices. Per-stage output power curves suggest that structural degradation in the thicker material limited device performance; this may be mitigated by minimization of epilayer strain.

Output powers exceeding 25 mW at 77 K from a 1×1 mm^2 mesa were observed under quasi-DC biasing conditions, and 2.5 mW observed under the same conditions for a 120×120 μm^2 mesa. Single pixel apparent temperature of the 120×120 μm^2 mesa exceeded 2000 K, and including a hypothetical fill factor in the calculation yielded 1600 K. These calculations suggest that, in the presence of adequately deep angled sidewalls, full-band apparent temperatures exceeding 2000 K should be possible in MWIR LED arrays, and higher temperatures if the observed spectral window is narrowed..

CHAPTER 6
LONG-WAVE INFRARED SUPERLATTICE LEDS

6.1 Device Design

A favorable atmospheric transmission band from 8-12 μm in the infrared was the emission band target for long-wave infrared devices. Sufficiently red-shifting the superlattice so that the device emitted within the atmospheric transmission band required approximately 16 ML of InAs content; the 77 K band structure for an InAs/GaSb 16/14 ML superlattice is shown in Figure 6.1(a). The carrier distribution for that layer combination is shown for 77 K and room temperature in Figure 6.1(b). When incorporat-

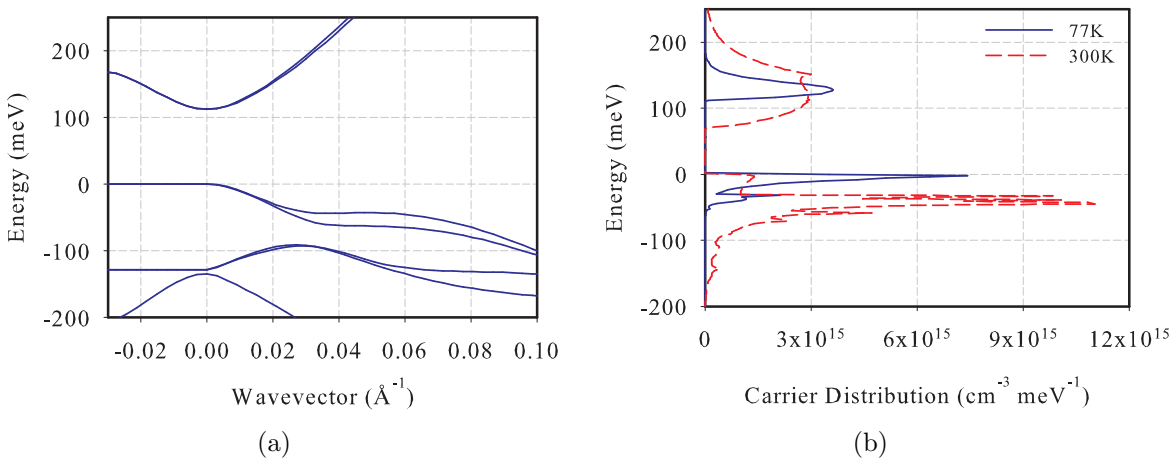

Figure 6.1: (a) Band structure for the InAs/GaSb 16/14 ML superlattice at 77 K and (b) carrier distribution for 77 K and room temperature. The calculated 77 K bandgap was 11 μm, which yielded a peak emission wavelength of ~10 μm.

ing such a device design into a MBE growth recipe, strain balancing must be addressed at the interfaces. Typically this requires some iteration to produce the desired cutoff wavelength while keeping a structure strain balanced. As Figure 6.2 illustrates, approximately 1.6 ML of InSb-like bond content is required per-period to alleviate strain.

Simply adding 1.6 ML of InSb-like content would reduce the energy gap by approximately 14meV; causing a cutoff wavelength shift of 1.6 μm. To avoid errors in the energy gap, which is quite sensitive in the LWIR, interface content must be accounted for in recipe formulation. In the work presented here, a fraction of the indium content

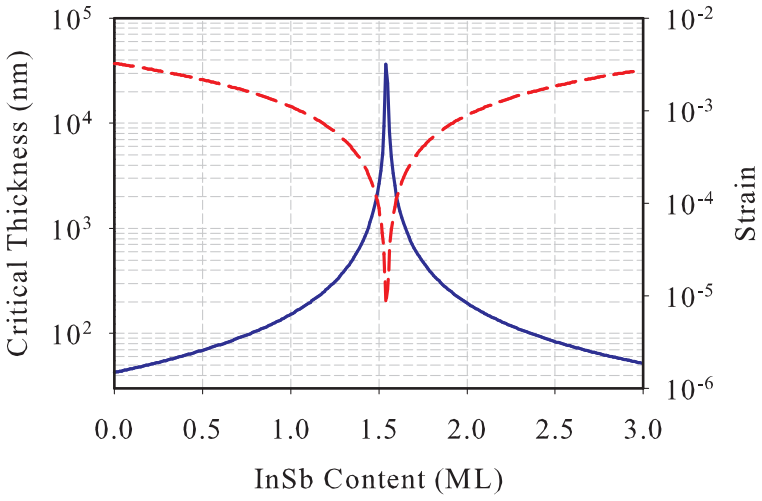

Figure 6.2: Simulation of strain compensation by including InSb-like bonds at the interfaces of an InAs/GaSb 16/14 ML superlattice.

of the SL was removed and added to the interfaces by appropriate shutter sequences in effort to maintain a desired emission spectrum.

6.1.1 Tunnel Junctions and Graded Regions

Growth of graded SL regions was optimized for strain in long-wave devices. Rather than relying on common interface recipes, graded SL interfaces were treated on a per-period basis to minimize local and overall epilayer strain. Grading of the conduction band was employed to transition from the n-GaSb clad layer to the cascaded SL active region. The layer sequence was 2/14/4/14/7/14/10/14...16/14 ML InAs/GaSb, which in Table 6.1 shows grading of the conduction band from approximately 1786 meV to 1214 meV. The calculated conduction band edge energies for bulk GaSb and an

InAs/GaSb 16/14 ML SL are 1958 meV and 1214 meV, respectively. Strain balancing of the n-GaSb to SL grade was accomplished by adjusting interface composition to neutralize strain in each period. Due to the fact that many of the InAs layers in this grade were very thin, and considering that the no-common-atom interfaces have at minimum ∼0.5 ML of bonds, purely InSb-like interfaces would have overcompensated for the InAs-induced strain. Alternating InSb-like and GaAs-like interfaces were thus used in both of the clad/superlattice transition grades. The InAs layers in the tunnel junction grades were sufficiently thick to use the same interface shutter sequence as in the SL active regions.

Similar grading of the valence band was performed for the graded SL tunnel junction layers and the SL to p-GaSb transition grade. Valence band energies for InAs/GaSb SL combinations at 77 K are shown in Table 6.2. As the graded region of the tunnel junction provided hole confinement by lowering the valence band, a thick InAs layer followed immediately after the 30 nm of 5×10^{18} cm^{-3} p-GaSb side of the junction. The graded region consisted of 16/3/14/6/16/10/16/14 ML InAs/GaSb which was n-doped at 3×10^{18} cm^{-3}. This configuration was intended to bring the conduction band of the graded region, calculated to be 1103 meV, below the GaSb valence band at 1160 meV to make the junction region semi-metallic. Low resistance to tunneling is critical for high efficiency cascaded devices; the high doping levels of the n-type and p-type sides of the junction helped to assure that this was the case [111].

6.2 MBE Growth and Optimization

6.2.1 Epitaxy of Interfaces

Optimization of interface shutter sequences is of particular importance in any short-period superlattice structure. In order to briefly examine the parameter space for

InAs (ML)	GaSb (ML)																
	2	3	4	5	6	7	8	9	10	11	12	13	14	15	16	17	18
2	1345	1467	1542	1614	1648	1685	1702	1718	1735	1753	1771	1778	1786	1794	1802	1812	1808
3	1284	1383	1466	1514	1563	1593	1625	1638	1662	1677	1692	1696	1701	1718	1725	1731	1738
4	1237	1329	1389	1448	1477	1520	1548	1568	1589	1600	1612	1625	1639	1641	1656	1660	1665
5	1186	1272	1343	1384	1424	1465	1482	1508	1526	1535	1554	1565	1576	1577	1589	1592	1594
6	1160	1230	1298	1336	1373	1404	1426	1450	1465	1481	1489	1507	1516	1525	1526	1537	1538
7	1135	1201	1252	1302	1332	1359	1381	1402	1416	1430	1445	1452	1460	1467	1476	1486	1486
8	1122	1186	1223	1264	1298	1325	1344	1365	1377	1390	1404	1410	1424	1431	1438	1438	1446
9	1108	1158	1206	1240	1266	1291	1310	1328	1340	1359	1364	1377	1383	1388	1395	1402	1405
10	1094	1144	1184	1216	1241	1265	1283	1301	1312	1323	1334	1346	1351	1356	1362	1368	1371
11	1082	1129	1162	1194	1218	1241	1258	1275	1285	1295	1306	1317	1322	1326	1331	1337	1339
12	1069	1115	1147	1178	1201	1218	1234	1250	1260	1275	1279	1290	1294	1301	1306	1311	1313
13	1062	1101	1133	1162	1180	1201	1216	1232	1241	1250	1260	1264	1271	1277	1282	1283	1288
14	1055	1094	1124	1148	1164	1185	1200	1209	1218	1232	1239	1245	1249	1255	1259	1264	1265
15	1048	1086	1111	1134	1155	1170	1184	1193	1202	1213	1219	1225	1231	1237	1241	1242	1247
16	1041	1074	1103	1125	1141	1155	1169	1178	1188	1196	1202	1208	1214	1217	1221	1225	1229

Table 6.1: Calculated conduction band edge energies (meV) for superlattice layer thickness combinations at 77 K.

InAs	GaSb (ML)																
(ML)	2	3	4	5	6	7	8	9	10	11	12	13	14	15	16	17	18
2	880	943	985	1023	1044	1063	1074	1084	1093	1101	1108	1113	1118	1122	1125	1128	1130
3	833	902	956	990	1020	1041	1059	1071	1083	1092	1100	1105	1110	1116	1120	1123	1126
4	803	879	929	974	1000	1029	1048	1063	1076	1085	1094	1101	1107	1112	1117	1121	1124
5	771	854	918	958	993	1023	1041	1058	1071	1082	1092	1099	1105	1110	1115	1119	1122
6	759	837	908	950	987	1016	1037	1055	1068	1080	1089	1097	1104	1110	1114	1119	1122
7	745	830	894	949	983	1012	1034	1052	1066	1078	1088	1096	1102	1108	1114	1118	1121
8	743	834	889	942	981	1012	1033	1052	1066	1078	1088	1095	1103	1109	1114	1118	1122
9	741	822	894	943	979	1010	1032	1051	1065	1079	1087	1096	1102	1108	1113	1118	1121
10	736	823	891	942	979	1010	1033	1051	1065	1077	1087	1096	1102	1108	1113	1118	1121
11	730	822	886	939	977	1010	1032	1051	1065	1077	1087	1096	1102	1108	1113	1118	1121
12	721	819	886	940	979	1008	1031	1250	1064	1078	1087	1096	1102	1108	1113	1118	1121
13	722	815	885	941	976	1009	1032	1052	1066	1078	1088	1095	1102	1108	1113	1117	1121
14	722	819	890	940	975	1010	1033	1050	1064	1078	1088	1096	1102	1108	1113	1118	1121
15	720	821	885	938	980	1009	1033	1050	1064	1078	1087	1095	1102	1108	1113	1117	1121
16	717	811	889	942	978	1008	1033	1050	1065	1078	1087	1095	1095	1108	1113	1117	1121

Table 6.2: Calculated valence band edge energies (meV) for superlattice layer thickness combinations at 77 K.

interface deposition in LWIR InAs/GaSb emitters, several samples were grown to test the resulting structural properties of various interface shutter sequences. Devices for interface deposition analysis were grown as single-stage emitters with 1.5 μm thick superlattice active regions. Growth rates for both InAs and GaSb were 0.8 ML/s and BEP ratios were 2.8 and 2.0 for GaSb and InAs, respectively. Analysis was performed by high resolution x-ray diffraction measurements, and dynamical fits to the diffraction spectra were performed in order to determine the SL layer thicknesses.

Strain balancing of binary/binary InAs/GaSb SLs requires increasing amounts of InSb-like content at the interfaces as the energy gap is reduced. Compensation of strain in an InAs/GaSb 9/16 ML structure requires less than 0.5 ML of InSb-like content at each interface, equating to a single set of In-Sb bonds per interface. Superlattices with InAs/GaSb 16/14 ML require roughly double the InSb-like interface bonds. In order to test alternative interface shutter sequences in attempt to increase the InSb-like content, four samples were grown with varying recipes for interface deposition.

Interfaces may be deposited with three primary techniques: migration enhanced epitaxy (MEE), codeposition, and soaking. Migration enhanced epitaxy refers to the procedure of depositing a layer of group III material in the absence of group V flux, then terminating the group III flux and applying group V flux to finish the binary layer [112, 95]. So-called "soaking" refers to applying group V material in the absence of group III material. Soaking of the growth surface has multiple potential uses. Arsenic soaking of the normal (InAs on GaSb) interface may be used to remove residual antimony which persists on the growth surface [94, 93], thus reducing layer intermixing. Arsenic-for-antimony exchange may also cause morphological problems if GaSb surfaces are exposed to arsenic for extended periods [113]. Soaking may also be used to form interfaces; antimony-for-arsenic exchange at the inverted interface is a common method for forming InSb-like bonds [92]. Simply using codeposition (simultaneous application of groups III and V flux) for interface formation is also commonly employed [98].

Both soaks and MEE were used in this work; several variations of interface shutter sequences were explored in order to strain balance nominally 15/14 ML and 16/14 ML InAs/GaSb superlattices. Since the InSb-like bond content per-period necessary to strain balance the structures was approximately 1.6 ML, the interface recipe for MWIR structures (Table 6.3) had to be modified to increase indium content at the interfaces. All samples had a 1.0 μm thick GaSb buffer layer grown, and a 1.5 μm thick superlattice region. The first approach attempted was to use MEE at both interfaces as shown in

Normal	Inverted
6.9‘s Sb soak	4.1 s Sb soak
1 ML In MEE	
2 s interrupt	
0.6 s As soak	

Table 6.3: Interface shutter sequence for MWIR superlattices.

column A of Table 6.4. While this produced good lattice matching with strain being 2.5×10^{-4} and the x-ray rocking curve showed superlattice diffraction peaks up to 4^{th}th order, the superlattice peaks were broad, with full width at half maximum of 69.7 seconds of arc. Broad peaks are indicative of interface roughness [114]; in this case likely a result of excess antimony on the growth surface or an excessively thick inverted interface. Next, three samples were grown with MEE at the normal interface and only an antimony soak at the inverted interface.

Unlike the case of the MWIR interfaces where the MEE layer was followed by an arsenic soak, the MEE layer for the series of three samples was followed by an antimony soak and arsenic soak in the LWIR devices. The variable of these samples (B, C, and D

A		B		C		D	
Normal	Inverted	Normal	Inverted	Normal	Inverted	Normal	Inverted
6.9 s Sb soak	1.4 s Sb soak	6.9 s Sb soak	1.4s Sb soak	6.9 s Sb soak	4.1 s Sb soak	6.9 s Sb soak	4.1 s Sb soak
1 ML In MEE	0.5 ML In MEE	1 ML In MEE		1 ML In MEE		1 ML In MEE	
2 s interrupt	2 s interrupt	2 s interrupt		2 s interrupt		2 s interrupt	
0.6 s As soak	4.1 s Sb soak	0.6 s Sb soak		0.6 s Sb soak		0.6 s Sb soak	
		0.1 s As soak		0.3 s As soak		0.5 s As soak	

Table 6.4: Interface shutter sequences for four 15/14 ML InAs/GaSb superlattices.

in Table 6.4) was the duration of the arsenic soak which followed the second antimony soak in the normal interface shutter sequence. The rationale for this series was as follows; using an antimony soak after the indium MEE layer should encourage InSb-like bonds to form, and the subsequent arsenic soak should remove residual antimony from the growth surface to prevent intermixing in the InAs layer. Additional arsenic, however, will shift the diffraction peak to the right (larger angle) due to the decrease in lattice constant.

Parameter	Sample			
	A	B	C	D
Strain	2.5×10^{-4}	8.1×10^{-5}	3.1×10^{-4}	4.4×10^{-4}
SL_{-1} FWHM	59.2	55.4	24.2	26.9
SL_0 FWHM	69.7	73.1	21.7	20.5
SL_{-1} FWHM	60.5	63.3	24.8	33.7

Table 6.5: Structural results of the interface study; full width at half-maximum (FWHM) values for the superlattice diffraction peaks (SL_i) are given in arc seconds.

The trend of increasing strain with increasing arsenic soak was indeed observed, as listed in Table 6.5. Superlattice diffraction peak widths were also observed to decrease significantly going from 0.1 s of arsenic soaking to 0.3 s. Peak widths changed little when the arsenic soak was again increased to 0.5 s. The increase in strain needs no further explanation. Dependence of the peak widths (FWHM) on arsenic soak was of somewhat more interest. Increasing the soak to 0.3 s significantly improved the peak widths; this was expected due to removal of excess antimony on the growth surface thereby yielding a sharper interface. The slight increase in the peak widths for the 0.5 s arsenic soak was likely due to the increased level of strain, or possibly arsenic-for-antimony exchange on the InSb-like interface which had just been deposited. These data demonstrate that the

soaks which complete the MEE deposited normal interface offer a direct means to form sharp interfaces, as well as control strain. Optimized cascaded devices made use of the 0.3 s arsenic soak; the x-ray diffraction data for the test sample based on this interface shutter sequence is shown in Figure 6.3.

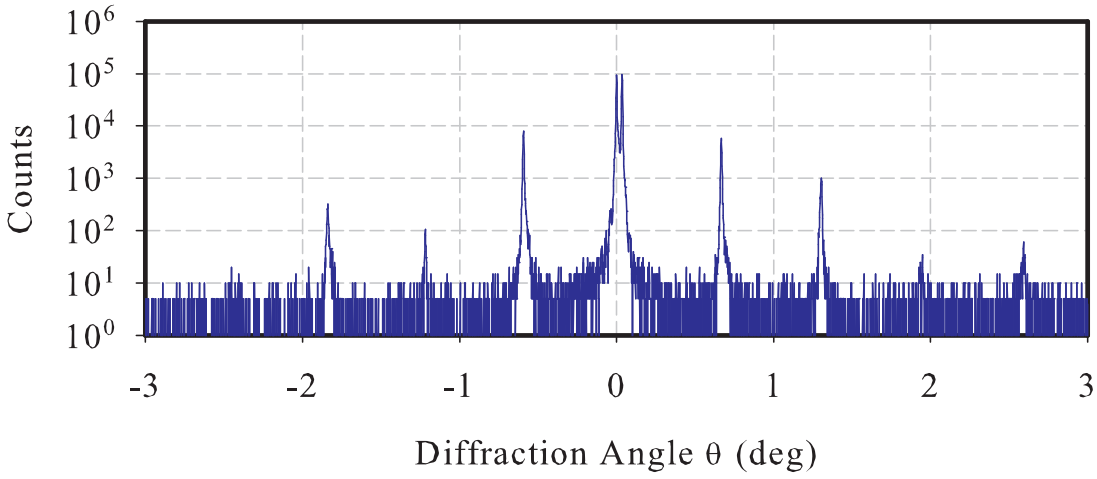

Figure 6.3: X-ray rocking curve for the 0.3 s arsenic soak case (sample C).

6.2.2 Tunnel Junction Strain

Due to the high fraction of epilayer material in the tunnel junctions, which was approximately 20% for a cascaded LED with 100 nm thick active regions, strain was addressed separately for this graded SL region. A sample was grown consisting of only 33 repeats (1 μm thick) of the tunnel junction graded SL for which the x-ray rocking curve is shown in Figure 6.4; typical InSb-like interfaces were encouraged. Due to the high number of individual layers in the growth stack, simulation of the x-ray data to determine layer thicknesses (and consequently strain) was not possible due to convergence issues with the simulation software. Strain was estimated based on the 220 arc second splitting of the substrate and superlattice peak, which was referenced to a curve of peak-splitting as a function of strain (Figure 6.5) determined from x-ray models of several SL active

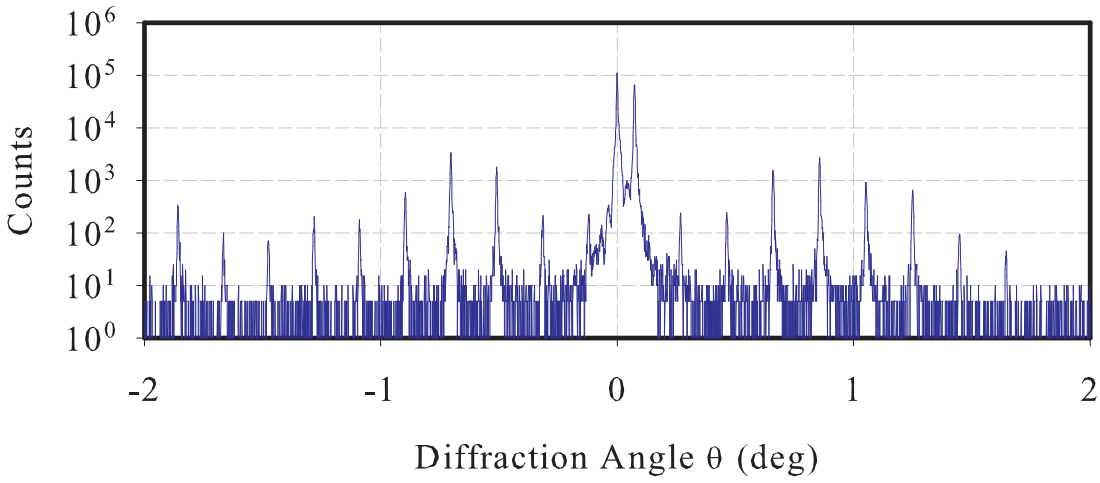

Figure 6.4: X-ray rocking curve for a sample where only graded SL regions were grown. Total sample thickness was 1 μm.

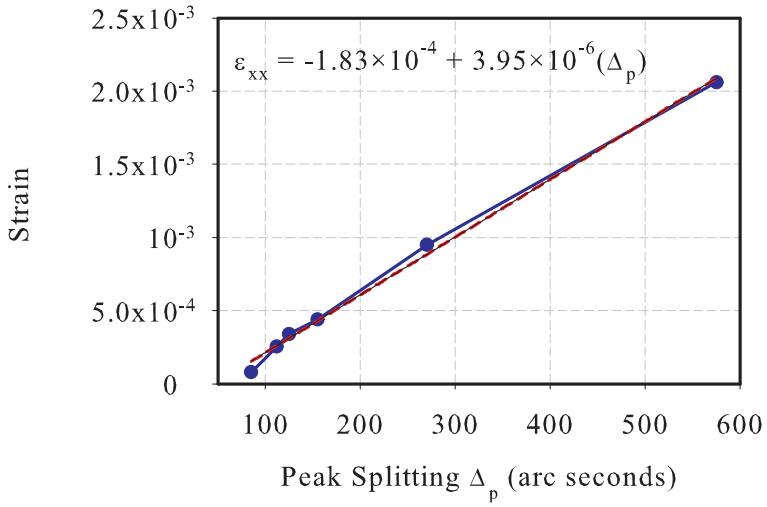

Figure 6.5: Strain as a function of substrate-superlattice peak splitting for InAs/GaSb SLs in tensile strain. The solid line (with circles) shows strain which was calculated by x-ray rocking curve model fitting and elastic theory; the dashed line is a linear fit to the data for which the equation is given in the plot.

regions. The plot of strain as a function of splitting of diffraction peaks is shown in Figure 6.5. Using this fit to the data, the tunnel junction shown in Figure 6.4 was in tensile strain of 7.34×10^{-4}. While the strain was not excessive, interfaces were modified to have slightly higher InSb-like content in subsequent growths.

6.2.3 Photoluminescence Tests

Prior to growth of LED devices, several LWIR InAs/GaSb active regions were tested in samples designed for photoluminescence. Photoluminescence testing is useful in that samples may be rapidly analyzed, as no device fabrication or packaging are necessary. Another unrelated advantage of growing active regions in a sample designed for optical carrier injection is that ultrafast spectroscopic techniques may be used to study carrier dynamics, a topic which will be discussed briefly in Chapter 7. Samples for photoluminescence consisted of an undoped GaSb buffer followed by a superlattice active layer, which was cladded on either side by 100 nm of $AlAs_{0.08}Sb_{0.92}$ for carrier confinement. A 10 nm thick GaSb cap layer was used to help prevent oxidation of the aluminum-containing layers. Three superlattice active regions were grown: 14/14 ML, 15/14 ML, and 16/14 ML InAs/GaSb. Corresponding calculated cutoff wavelengths were 8.4 μm, 9.6 μm, and 11 μm; measured values of cutoff (half intensity on the long wavelength side of the spectrum) were 8.3 μm, 9.8 μm, and 10.8 μm as shown in Figure 6.6. As the goal was to locate the emission spectrum in the 8-12 μm band, the 16/14 ML InAs/GaSb active region was chosen as the nominal design for LED devices.

6.2.4 Growth Conditions

Epitaxial growth conditions for LWIR samples were modified somewhat from those used for MWIR samples. Perhaps most significantly, growth rates for both InAs and GaSb were increased to 0.8 ML/s. The primary reason for this was efficient use of reactor time; growth of 16-stage devices at an average growth rate of 0.42 ML/s took in

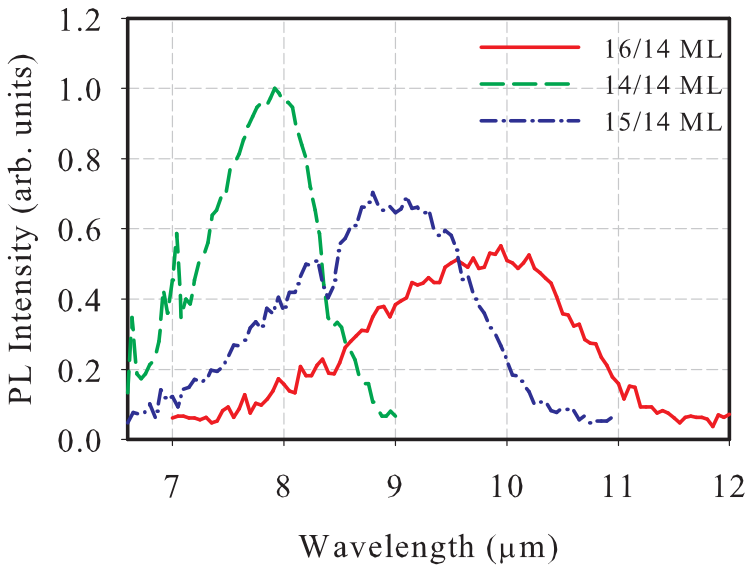

Figure 6.6: Photoluminescence spectra taken at 77 K from samples with 14/14 ML, 15/14 ML, and 16/14 ML InAs/GaSb superlattice emitting regions.

excess of 12 hours, while using 0.8 ML/s a growth could be completed in 6 hours. Beam equivalent pressure ratios as measured with an ion gauge were 2.0 and 2.8 for InAs and GaSb, respectively. Arsenic cross-contamination in the GaSb layers was not expected to cause significant degradation to the devices, even at high growth rates. Closing the valve of the arsenic cell cracking zone during deposition of non-arsenic-containing layers prevented excessive arsenic from remaining in the chamber when the shutter was closed. Results from studies of photoluminescence samples in fact indicated that the higher growth rates yielded enhanced optical quality [86]. While optical quality may benefit from the high growth rate, shutter timing becomes increasingly important as beam transients at high flux may cause deviation from the intended structure. Due to the high growth rates and the low thickness of the SL/clad graded regions, no dopant ramps were used in the grades.

All samples made use of a 2.0 μm thick n-GaSb buffer layer doped at 1×10^{18} cm^{-3}. This buffer was grown thick so that the mesa etch could be stopped in a highly doped layer and a satisfactory n-type contact could be formed, as the underlying substrates were

very lightly doped n-GaSb. The absorption properties of n-doped GaSb were discussed briefly in Section 1.1; plots of absorption in three different n-GaSb substrates at 100 K are shown in Figure 6.7. Measured absorption in Te-doped GaSb wafers demonstrated similar results to those presented by Chandola *et al.* [115]. Clearly, substrates with very

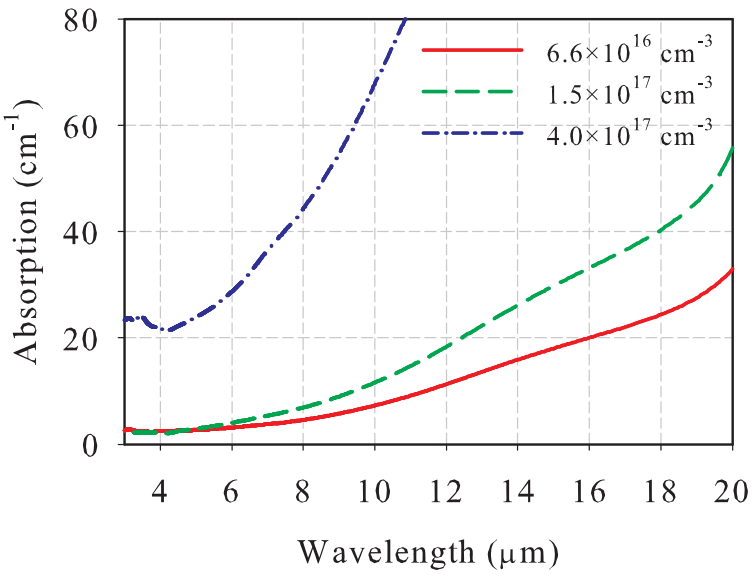

Figure 6.7: Absorption in n-GaSb substrates at 100 K. Tellurium doping level is indicated in the plot legend.

low n-type doping are necessary for back-emitter configured LEDs in the LWIR unless substrates are thinned substantially. Samples should also be grown from adjacent wafers in a boule when possible if the substrate is not to be thinned, as doping variations may easily lead to variation in output power due to absorption.

6.3 Electrical and Optical Characteristics: Quasi-DC Results

In the following, LWIR devices are characterized in much the same manner as were MWIR devices in Chapter 5, however fewer samples were grown due to generalizations which may be carried from MWIR results. Output power temperature dependence, for

example, was not characterized. It follows that room temperature performance would be significantly poorer than performance at LN_2 temperature, with the added complication that the wavelength shift with temperature is appreciable for narrow-gap samples. A sample grown for 11 μm cutoff wavelength at 77 K, for instance, would have the cutoff wavelength shifted to approximately 17.8 μm at room temperature; this is not in a useful spectral band for the intended applications.

6.3.1 Performance of Cascaded LEDs

Assessment of output power and efficiency improvement in cascaded LEDs in the LWIR was made by comparing results from single-stage and eight-stage samples. Before growth of thick emitters, where a host of growth parameters can weigh on the performance, it was necessary to determine whether the tunnel junction design was functional and how a cascaded LED compared to a single stage LED. While intended for a peak emission wavelength of 10 μm, the samples had peak emission at $\sim$8 μm as shown in Figure 6.8, this was likely due to a slight drift in growth rate. For a device with a design cutoff wavelength of 11 μm, a growth rate drift of indium of $\sim$10% is sufficient to cause a 38 meV (2.5 μm) shift in cutoff wavelength.

Performance of single stage versus cascaded material was made by comparing a single-stage device with 1.0 μm active region thickness with an eight-stage device having 200 nm thick active regions. As in the MWIR study presented in Section 5.5.2, the single stage LED emitted less power and had poorer efficiency. Light-current and quantum efficiency curves are shown in Figure 6.9. Similar characteristics were observed as in the MWIR samples; the cascaded material had higher output power and higher efficiency. A series voltage contributed from the cathode contact was again suspect in the low efficiency for the single stage device; Figure 6.9(c) shows the single stage device using 2.5 V of bias at peak emission while the bandgap was only 0.15 V. The same clamping of the output occurred as was observed for many of the MWIR samples, again this was

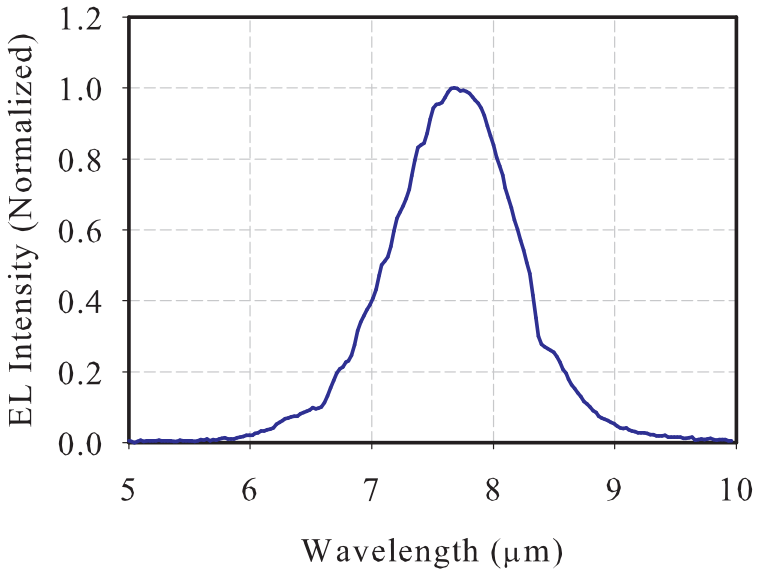

Figure 6.8: Electroluminescence spectrum of an eight-stage cascaded LED with cutoff wavelength of ∼8.3 μm.

largely attributed to both carrier leakage and Joule heating. As the active regions in the cascaded device were only 200 nm thick, the current density for a given drive current was a factor of five higher than for the 1.0 μm thick single stage sample. Despite this limitation, the eight stage device performed better in all aspects.

Interference microscopy revealed comparable levels of large oval defects (approximately 10×7 μm) on both the single-stage and eight-stage devices, however the eight stage device also presented smaller oval defects as shown in Figure 6.10(b). These small defects measured approximately 2-3 μm in diameter; and may have arisen simply due to the 1 μm of increased epilayer thickness.

6.3.2 Comparison: Active Region Thickness

Growth of 16-stage LEDs followed the comparison of single stage to eight stage, as that study clearly demonstrated the the cascaded LED design was functional. In an attempt to optimize the tunnel junctions and assure low resistance, the doping level in

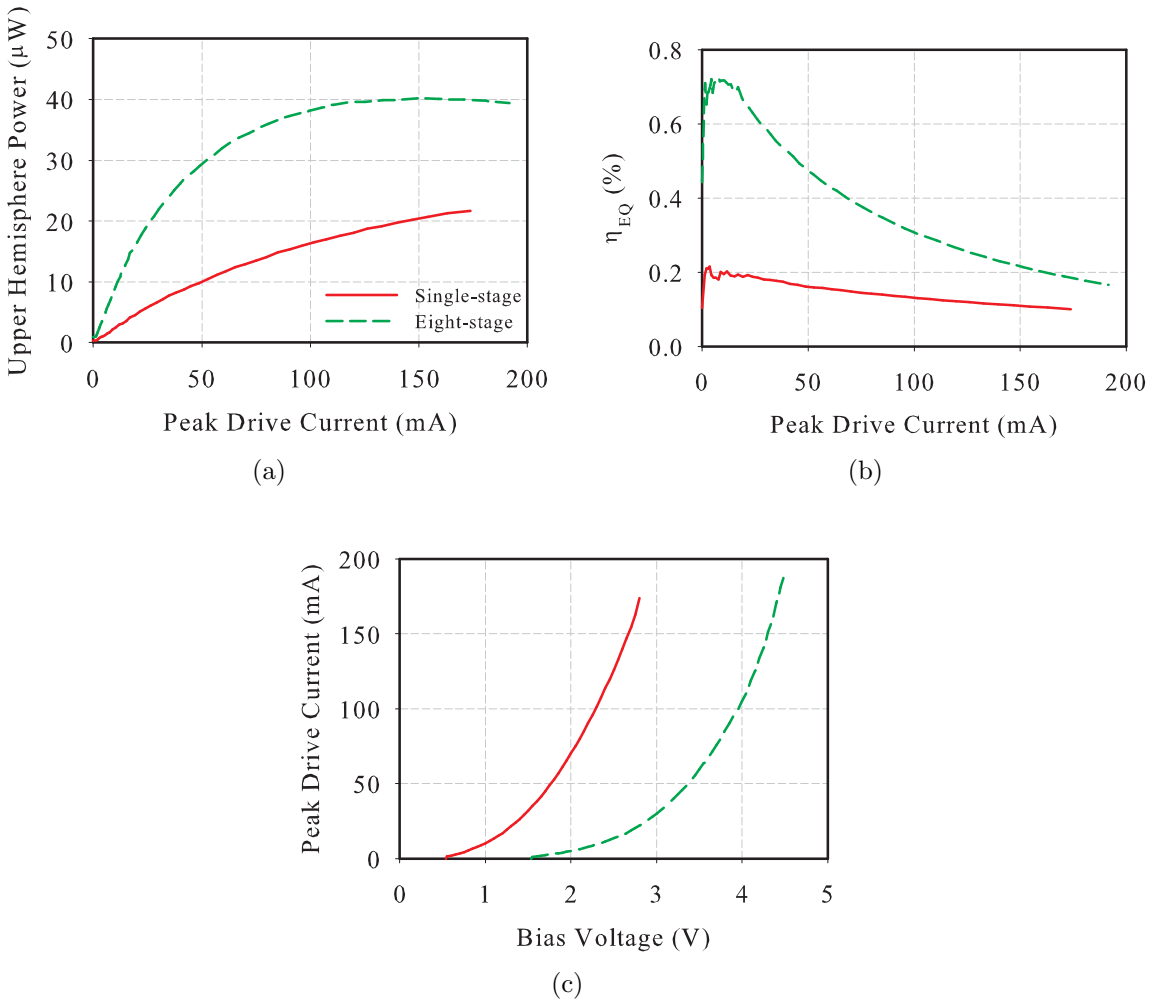

Figure 6.9: (a) Power output, (b) external quantum efficiency, and (c) current-voltage plots for single-stage and eight-stage LEDs with peak emission near 8 μm.

the n-type SL grade side of the junction was increased from 5×10^{17} cm^{-3} to 3×10^{18} cm^{-3}. Growth rates remained at 0.8 ML/s for both InAs and GaSb; the BEP ratios were 2.0 and 2.8, respectively. The growth stack employed for all 16-stage emitters is shown in Figure 6.11, the tunnel junction is highlighted by the dark gray region.

Because band-to-band Auger recombination scales approximately as λ^2, this loss mechanism is expected to be much more pronounced in the LWIR LEDs. Assessment of the impact of Auger recombination was made by growing two 16-stage samples with different active region thicknesses, thereby effectively scaling down the carrier density

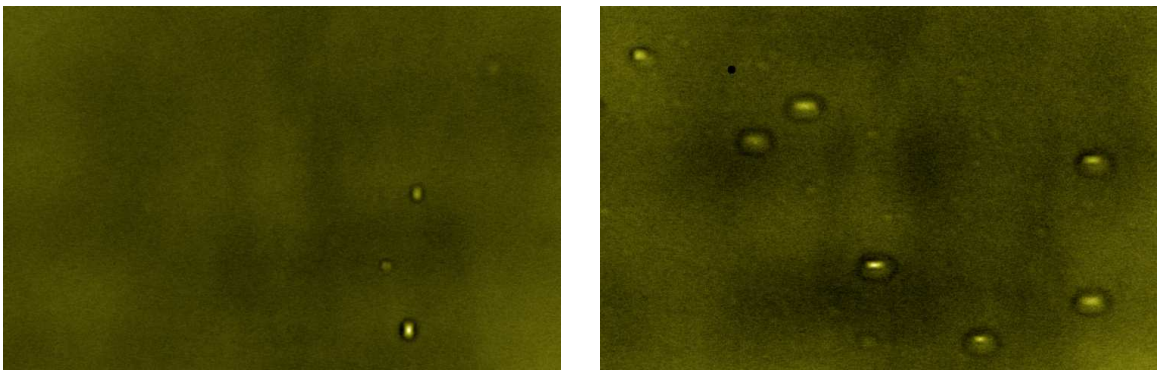

(a) (b)

Figure 6.10: Interference micrographs (122×93 μm^2 image) of defects on the (a) single stage and (b) cascaded devices.

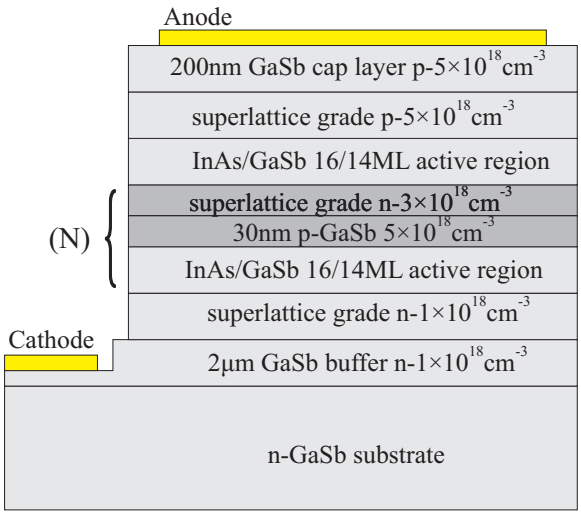

Figure 6.11: Growth stack for the 16-stage LWIR LEDs.

in the thicker active region by a factor of two. Active regions 100 nm and 200 nm in thickness were used, yielding overall device thicknesses of 2.75 μm and 4.35 μm excluding the buffer layer, respectively. Naturally the thicker structure was also more susceptible to the effects of strain; this was evaluated by structural and morphological analysis. The X-ray rocking curve for the LED with 100 nm active regions is shown in Figure 6.12. Rather than the typical diffraction peaks observed in other samples, double peaks were observed. This feature was attributed to the n-type graded SL regions in the tunnel

junctions, however modeling of the structure was not possible due to the number of variables in the growth stack. Using the same technique to estimate the strain from the substrate-SL peak splitting as depicted in Figure 6.5, the strain was determined to be approximately 1.9×10^{-4} from a peak splitting of $\Delta_p = 100$ arc seconds. The 16-stage sample with 200 nm thick active regions experienced strain of 2.6×10^{-4} by the same calculation.

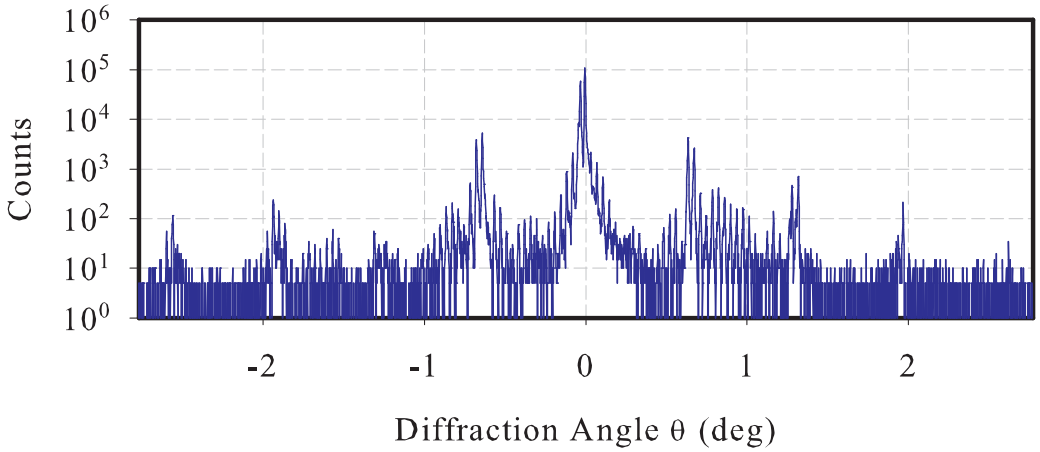

Figure 6.12: X-ray diffraction of the 16-stage LED with 100 nm thick active regions. The doublets present in the SL peaks were attributed to the graded regions in the tunnel junctions.

Interference and atomic force microscopy rendered similar results for both samples, with both having RMS surface roughness of 1.3 Å. Defect morphology was also similar for both samples as shown in Figure 6.13. These results together with the x-ray diffraction data suggest that no degradation in structural or morphological quality occurred for the sample with 200 nm thick active regions. This increase in thickness without loss of device quality was permitted due to the low strain in the structures. As devices with yet thicker epilayers likely require consideration for future applications, strain balancing is of upmost importance to ensure high device quality.

Quasi-DC electrical and optical characterization of the LEDs was performed at

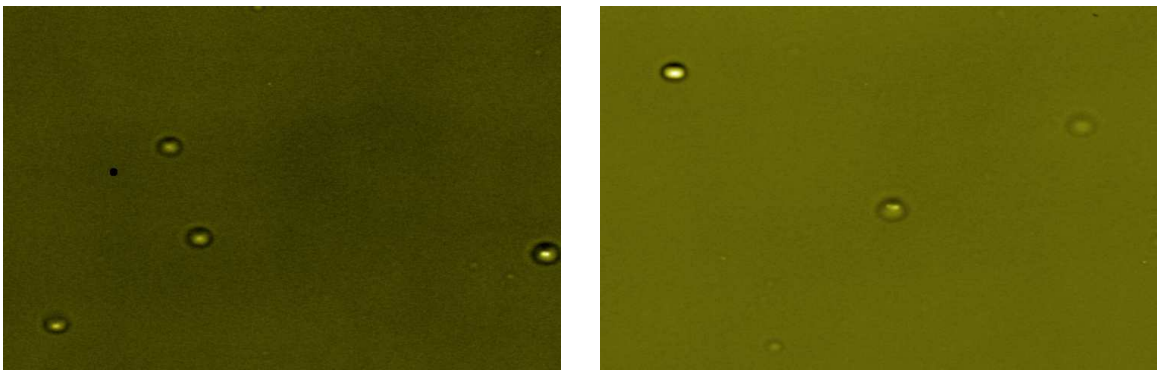

(a) (b)

Figure 6.13: Interference micrographs (306×233 μm^2 image) of defects on the 16-stage cascaded LEDs with (a) 100 nm and (b) 200 nm active region thickness. Measurement by atomic force microscopy yielded RMS surface roughness values of 1.3 Å over a 10 μm×10 μm scan for both samples.

77 K. Current-voltage and light-current characteristics are shown in Figure 6.14. The device with 200 nm active regions had an on-voltage which exceeded the 100 nm active region thickness device by 150 mV. The reason for the additional voltage consumption of 9 mV per stage was not immediately clear, however it could have been a result of inconsistency in fabrication or the need for additional potential to allow carriers to traverse the thicker structure. Output was observed to increase by 76% in the device with 200 nm active regions. This was partially attributed to suppressed Auger recombination as the current density was a factor of two lower for a given input current for the sample with 200 nm thick active regions. Another possible explanation for the increase in optical output is that the input power density was lower for the sample with 200 nm thick active regions and thermal loading was consequently reduced.

To provide comparison to MWIR results in terms of apparent temperature capability, the device with 100 nm active regions yielded 185 μW of power translating to 1300 K apparent temperature. Similarly, the device with 200 nm thick active regions yielded 1740 K. These calculations integrated over the 7-12 μm spectral band, as the entirety of the emission did not fall within the 8-12 μm as intended. No fill factor was

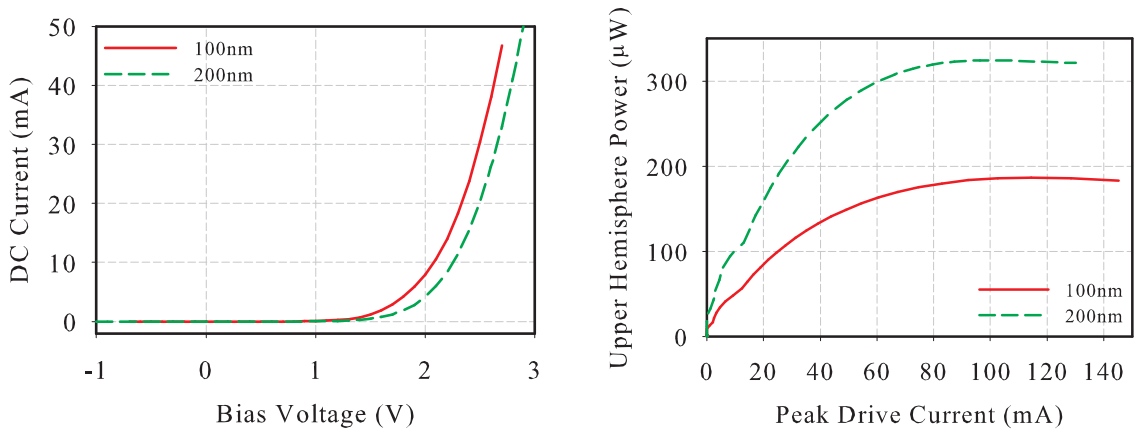

Figure 6.14: Output characteristics for 16-stage LEDs with 100 nm and 200 nm thick active regions. The cutoff wavelength was again somewhat less than expected: being 9.4 μm with a peak wavelength of 8.3 μm.

taken into account in these calculations, as devices were fabricated only into variable sized mesa test chips.

The device having 200 nm thick active regions was also tested with a larger mesa to produce higher output power. Figure 6.15(a) shows a comparison between 120×120 μm^2 and 220×320 μm^2 mesas; the larger mesa delivered in excess of 1 mW of power at 500 mA drive current. Corresponding external quantum efficiency plots are shown in Figure 6.15(b), little difference in peak efficiency was observed. High drive current was necessary to achieve 1 mW of output, thus the LWIR devices were (as expected) far less efficient than their MWIR counterparts.

6.4 Pulsed Measurements

In order to further sort out the limitations imposed by Joule heating and carrier leakage, pulsed excitation measurements were performed on both small and large area mesas of optimized 16-stage LWIR material. Measuring light-current characteristic

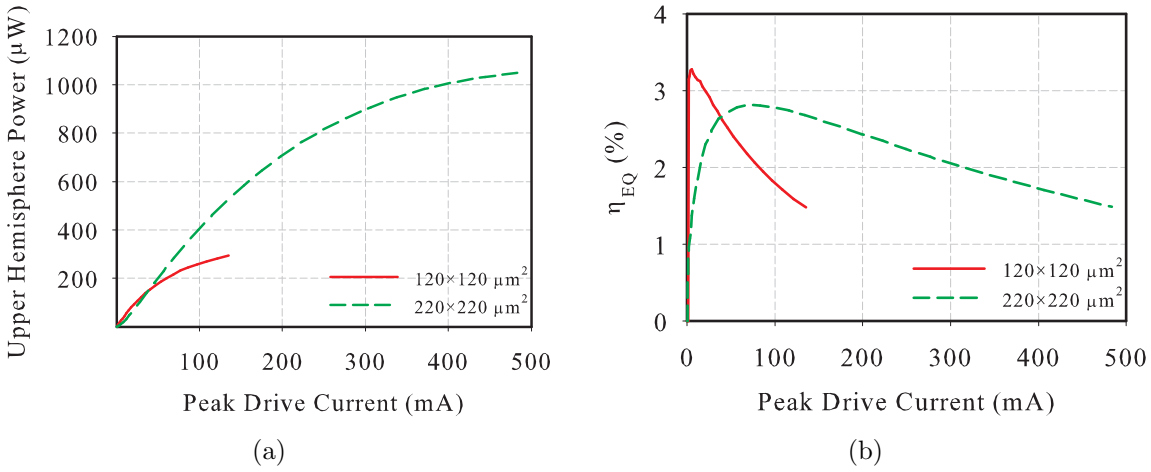

Figure 6.15: Examination of size dependence on output characteristics of the 16-stage device with 200 nm thick active regions.

curves as a function of duty cycle allows analysis of the effects of Joule heating on a device: lower duty cycles deliver lower average electrical power to the device active region, and heating may be minimized. In the case of small area mesas shown in Figure 6.16, changing the duty cycle from 50% (quasi-DC) to 10% produced only ∼12% improvement in optical output. Although significantly less electrical power was delivered to the device at 10% duty cycle, the current density was very high given the small area of the mesa. The high current density increases carrier leakage; thus the L-I curves exhibit only modestly better optical output due to reduced Joule heating.

Similar measurements on large area mesas yielded far different results. As shown in Figure 6.17, decreasing the duty cycle from 50% to 10% showed a gain of 56% in optical output at 60 A/cm^2 current density. Further decreasing the duty cycle to 5% yielded a 100% increase in optical output at the maximum drive current compared to 50% duty cycle excitation. The explanation for this follows from the argument for small area mesas: the current density supplied to the 1×1 mm^2 area devices was comparatively much smaller than that supplied to the 120×120 μm^2 devices. Therefore the carrier density was low, and carrier leakage likely not a limiting factor in device performance.

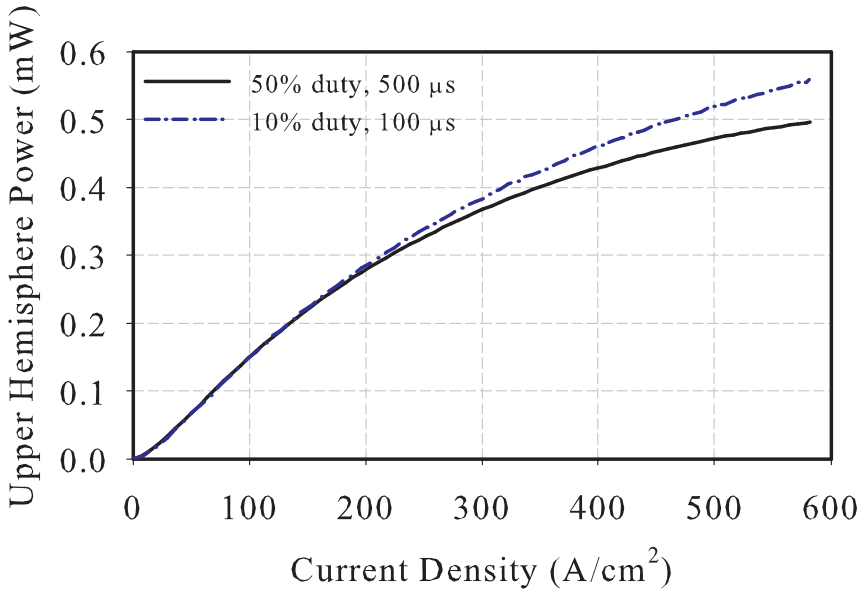

Figure 6.16: Pulsed excitation measurements on a 120×120 μm^2 LWIR mesa at 77 K.

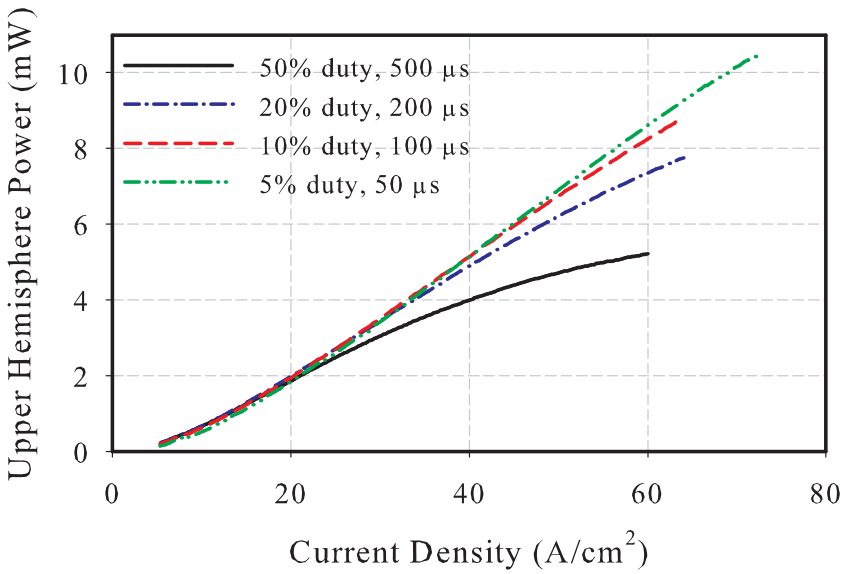

Figure 6.17: Pulsed excitation measurements on a 1×1 mm^2 LWIR mesa at 77 K.

Joule heating, on the other hand, was substantial at high duty cycle, as 1.5 W of average electrical power was dissipated in the LED at 600 mA drive current. Reducing the duty cycle to 10% reduced the average power dissipation to 0.3 W, and to 5% reduced it to 0.15 W. Over the range of drive currents applied, no observable slope change occurred (first derivative plot) at high drive current when the duty cycle was 5%, indicating that higher output power is likely achievable.

6.5 Projection of LWIR Device Performance in Arrays

In identical fashion to the projections on array performance for MWIR emitters in Section 5.6, projections for LWIR emitters are presented here. Emitters for LWIR operation demonstrated in this work, while intended to operate within the 8-12 μm atmospheric transmission window, actually had a peak emission wavelength of approximately 8 μm as discussed in Section 6.3.1. As moving the emission spectrum to fall within the desired band by proper growth modifications is straightforward, the center wavelength of the electroluminescence was shifted to 10 μm for the calculations presented in the following. Scaling the mesa size to 30×30 μm^2 yielded an output power of 30 μW, as shown in Figure 6.18. The full-band apparent temperature (8-12 μm) for a 48 μm pitch (40% fill factor) is shown in Figure 6.19 to be approximately 1700 K. Following are the results from three potential means to increase the observed apparent temperature: angled facets, consideration of the emission/detection spectral windows, and reduction of substrate absorption. These potential improvements were treated independently for clarity; again, no combined improvement is shown. Incorporating the potential improvement factor of 1.74 from angled sidewalls yields 2500 K. It should be noted that, with angled sidewalls, the actual fill factor is somewhat vague by definition. The apparent temperature will ultimately depend upon the number of camera counts over an area of many emitting pixels, effectively integrating over the entire contiguous

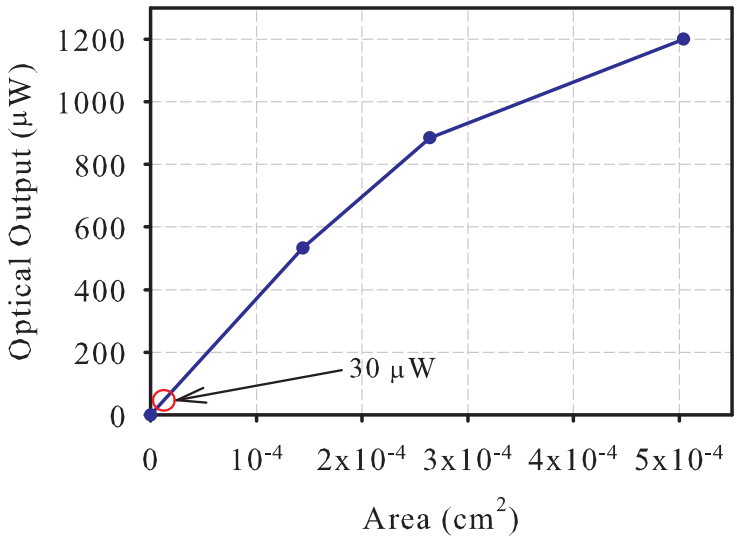

Figure 6.18: Scaling of LWIR peak upper hemisphere output power with mesa area. The output power from the smallest tested mesa was projected to zero to allow extrapolation to smaller devices.

array surface, including space which is unoccupied by emitting material. The fill factor (or mesa size) for calculation purposes was calculated from a plane vertically centered in a mesa with angled sidewalls, thus the actual mesa top would be roughly 20×20 μm^2 if a 45°, 10 μm deep etch were used.

Detection bandwidth scaling in the LWIR, shown in Figure 6.20, shows a similar trend to the scaling in the MWIR. As the LED emission wavelength spectrum is broader in the LWIR, the widest detection bandwidth was 4 μm with the center wavelength being 10 μm. This calculation assumed that the integrated power of the full emission spectrum was 30 μW, as no potential improvement factors were included. Again, apparent temperatures on the order of 3000 K seem possible with a sufficiently narrow detection bandwidth.

A further improvement factor for LWIR devices may come from substrate thinning. Absorption coefficients of 20 cm^{-1} at 10 μm wavelength are typical for GaSb wafers with n-type doping of 1-2$\times10^{17}$ cm^{-3}. Such an absorption coefficient in a 0.5 mm thick

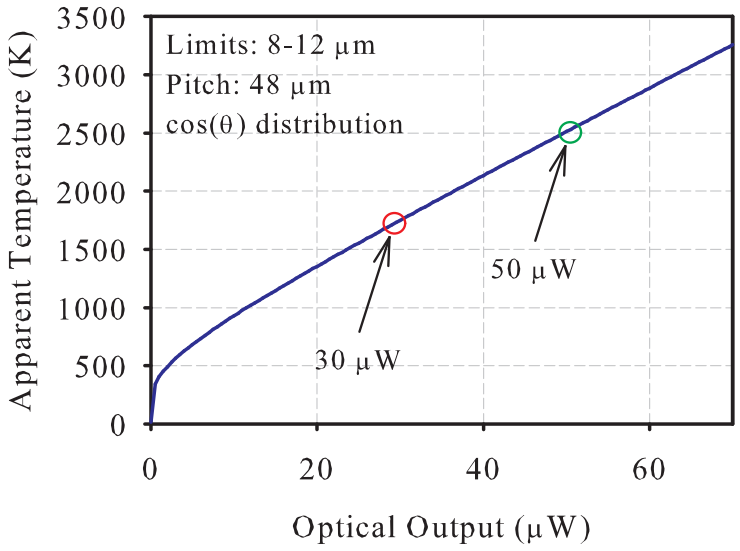

Figure 6.19: Scaling of apparent temperature with potential improvement from angled sidewalls. The improvement factor of 1.74 yields power output of nearly 50 μW, translating to approximately 2500 K.

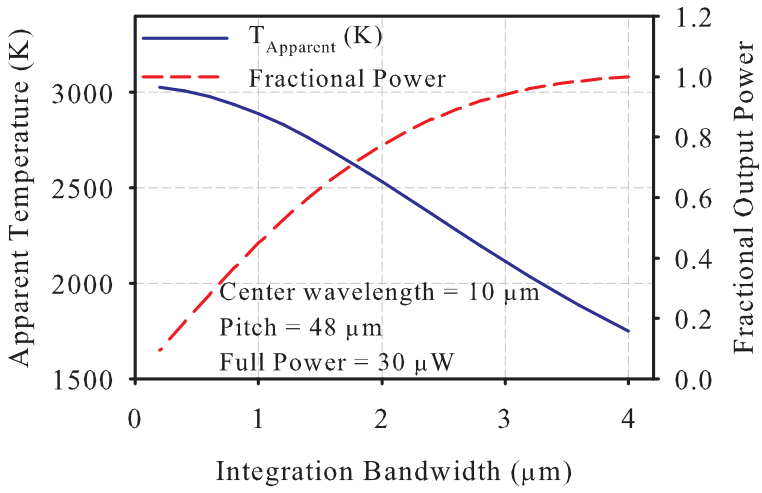

Figure 6.20: The effect of detection bandwidth (spectral integration limits) on LWIR apparent temperature.

substrate would lead to 63% absorption. Thinning the substrate to 50 μm thickness by lapping or fly-cutting would yield only 10% absorption, boosting output by a factor of nearly 2.5. Taking the original output power of a 30×30 μm^2 mesa through a substrate with absorption coefficient of 20 cm^{-1} and 0.5 mm in thickness (30 μW), and reducing the substrate thickness to 50 μm, would yield an output power of 75 μW and apparent temperature exceeding 3000 K with full-band integration.

6.6 Conclusions

Superlattice LEDs in the LWIR spectral band were demonstrated, with output powers that compare favorably to the published work in this spectral band. Mesas of 120×120 μm^2 size demonstrated output power exceeding 300 μW at 77 K, corresponding to a single-pixel (full-band) apparent temperature exceeding 1700 K. Structural and morphological quality were maintained even as epilayer thickness approached 4.5 μm, and interfaces were used to effectively manage strain. Results suggested that enhanced thermal management may lead to further improvement in output power, as Joule heating remains problematic. Carrier leakage was suspect as a limiting mechanism as well, and provided explanation for the clamping of output power at high drive current for small mesas; pulsed measurements support these assertions.

CHAPTER 7
CONCLUSIONS AND FUTURE EFFORTS IN LED DEVELOPMENT

Significant progress has been made in improving efficiency and output power of MWIR and LWIR superlattice LEDs, however much effort is required to optimize the material system and devices. Single pixel MWIR devices have shown external quantum efficiency exceeding 10%, and output power from a single 120×120 μm^2 mesa exceeding 2.5 mW under quasi-DC bias conditions. These figures yielded single-pixel, full-band apparent temperatures exceeding 2000 K, and when scaled to an 80×80 μm^2 mesa, 1800 K. While encouraging, and certainly an improvement over the state-of-the-art, performance in an array is the true test of functionality. In an array format, heating from adjacent pixels reduces output power. As discussed in Section 5.5.1, the performance of these superlattice LEDs is very temperature dependent, and optical output will be reduced when local heating increases active region temperature.

Results in the long-wave infrared have also shown promising results in comparison with published material [42]. Single pixel 120×120 μm^2 emitters have demonstrated output in excess of 300 μW at 77 K under quasi-DC bias conditions. This level of output corresponded to an apparent temperature exceeding 2000 K, however it is again emphasized that fill-factor considerations and array heating will reduce this value when the LED material is implemented in an array.

Large area cascaded SL emitters have been demonstrated as high power emitters in the MWIR and LWIR. Power in excess of 25 mW was measured from a 1×1 mm^2 mesa emitting at 3.8 μm with LN_2 cooling. Under similar conditions, emitters with peak emission wavelength of 8.3 μm had measured output of 1 mW from a 220×320 μm^2 mesa under quasi-DC bias conditions. A 520×520 μm^2 MWIR emitter also emitted 1.4 mW of power at 220 K, a temperature accessible with thermoelectric cooling. Such

single-element high power LEDs may find use in spectroscopy or process monitoring.

7.1 Device Optimization

Despite the advances in SL infrared emitters presented in this work, numerous technological improvements could yield higher performance. Only precious few of the many growth parameters which beg for optimization have been considered here. Studies of growth temperature dependence, V/III BEP ratio variation, and growth rate dependence on material quality could be performed to name only a small subset. Perhaps one of the most studied, yet most controversial topics in InAs/GaSb SL development is interface deposition. While general trends in interface behavior may be observed, interfaces must to some extent be uniquely adapted to the layer combination used. This is to say that a particular shutter sequence for a 8/8ML InAs/GaSb SL will likely not work verbatim in a 16/14 ML design. Interface deposition techniques are numerous, as are the active region designs on which those interface studies are based.

Naturally, first and foremost strain needs to be managed. This in and of itself largely dictates the interface content; the fraction of this interface content which is deposited at the normal and inverted interfaces, and how that content is deposited, is the technological challenge which must be addressed. As the interface bond content is a large fraction of the overall device in short period SLs, it stands to reason that device quality is heavily dependent on interfaces.

Development of device fabrication techniques and technology of antimonide-based materials is necessary. Painstaking efforts may be spent on optimizing growth and material quality; the fruits of this labor can only be fully realized if parasitic effects introduced by device fabrication are minimized. Oxidation, contamination, Schottky barriers, and sidewall leakage must be minimized to produce high quality, robust devices. Improvements in LED output may be realized by clever processing techniques such as, for example, angled facet etching as discussed in Section 5.4.2, anti-reflective coating

application, and sidewall passivation.

7.2 Multispectral Emitters

In this work, both MWIR and LWIR LEDs were presented. Interest exists to develop the InAs/GaSb SL technology further to produce devices which emit two colors simultaneously. This can be accomplished by growing two cascaded SL emitters in tandem as shown in Figure 7.1. Although this may appear trivial, the epilayer is necessarily thick to produce emitters with sufficient intensity. Strain management becomes key in

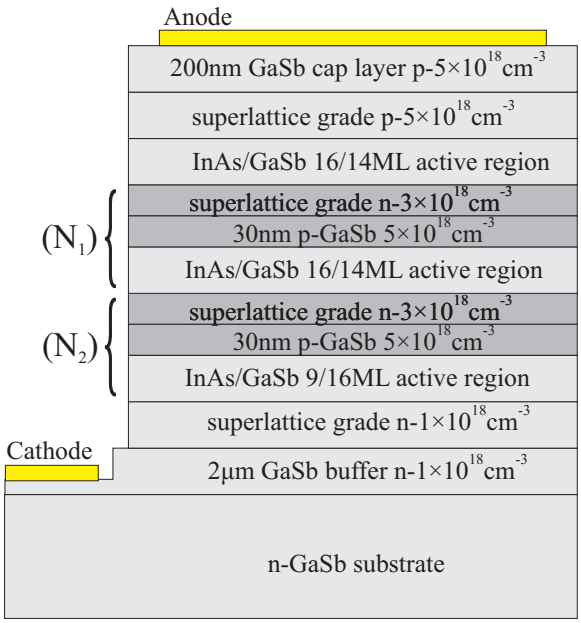

Figure 7.1: Potential growth configuration for a two-color MWIR/LWIR LED device.

this situation; as significant strain will likely cause poor quality in such a thick epilayer. A possible route to thin the epilayer is to use the thinnest InAs/GaSb layer combinations which yield the desired cutoff wavelength. For any design wavelength, multiple combinations of layer thicknesses are available. Adding indium to the GaSb layer provides a further degree of freedom and allows for yet thinner layers.

7.3 Ultrafast Measurements

Understanding of device performance and design tradeoffs requires having as much knowledge about the sample as possible. While structural and morphological characterization of materials may provide insight on quality, electronic and optical characterization are necessary to optimize device quality. X-ray rocking curves showing sharp peaks and little strain may be produced from a device which has poor optical quality; analysis beyond structure yields better understanding.

Optical characterization of materials with characteristics measurable with visible light is, while not always trivial, far more common than mid-wave and long-wave infrared optical characterization. Sources, detectors, and measurement techniques for MWIR and LWIR radiation are often expensive or nonexistent. Optical sources often rely on nonlinear optical generation mechanisms such as optical parametric amplification and difference frequency generation; conversion efficiencies become low as wavelength is increased, it follows that signal-to-noise ratio often assumes a similar trend. Upcoming work involves ultrafast optical characterization of MWIR and LWIR InAs/GaSb material. Development of a two-color transient absorption spectroscopy system based on an amplified Ti:Sapphire laser system and two optical parametric amplifiers is ongoing. Such a system should enable measurement of Shockley-Read-Hall recombination times in order to assess material quality. While simply measuring light output of a LED or detectivity of a detector gives some measure of material quality, these measurements are dependent on a host of factors. Ultrafast recombination measurements provide a more direct probe of material quality.

REFERENCES

[1] C. H. Grein, M. E. Flatté, J. T. Olesberg, S. A. Anson, L. Zhang, and T. F. Boggess. Auger recombination in narrow-gap semiconductor superlattices incorporating antimony. *J. Appl. Phys.*, 92(12):7311–7316, 2002.

[2] A. Rogalski. HgCdTe infrared detector material: history, status, and outlook. *Rep. Prog. Phys.*, 68:2267–2336, 2005.

[3] C. D. Maxey, M. U. Ahmed, C. L. Jones, R. A. Catchpole, P. Capper, N. T. Gordon, M. Houlton, and T. Ashley. Growth of Long Wavelength Infrared MCT Emitters on Conductive Substrates. *J. Electron Mater.*, 30(6):723–727, 2001.

[4] T. Ashley, C. T. Elliot, N. T. Gordon, R. S. Hall, A. D. Johnson, and G. J. Pryce. Negative luminescence from $In_{1-x}Al_xSb$ and $Cd_xHg_{1-x}Te$ diodes. *Electron. Lett.*, 36(7):1037–1044, 1995.

[5] O. B. Williams. Dynamic infrared scene projection: a review. *Infrared Phys. Techn.*, 39:473–486, 1998.

[6] M. Brown, A. G. Hayes, K. Anderson, J. James, and D. C. Harrison. Spectral Radiant Emission of Dynamic Resistive Arrays. In *Technologies for Synthetic Environments: Hardware-in-the-Loop Testing XII*, volume 6544 of *Proc. SPIE*, 2007.

[7] F. Fuchs, U. Weimer, W. Pletschen, J. Schmitz, E. Ahlswede, M. Walther, J. Wagner, and P. Koidl. High performance InAs/$Ga_{1-x}In_xSb$ superlattice infrared photodiodes. *Appl. Phys. Lett.*, 71(22):3251–3253, 1997.

[8] R. Rehm, M. Walther, J. Schmitz, J. Fleißner, F. Fuchs, W. Cabanski, and J. Ziegler. InAs/(GaIn)Sb short-period Superlattices for Focal Plane Arrays. In *Infrared Technology and Applications XXXI*, volume 5783 of *Proc. SPIE*, pages 123–130, 2005.

[9] H. S. Kim, E. Plis, J. B. Rodriguez, G. D. Bishop, Y. D. Sharma, L. R. Dawson, S. Krishna, J. Bundas, R. Cook, D. Burrows, R. Dennis, K. Patnaude, A. Reisinger, and M. Sundaram. Mid-IR focal plane array based on type-II InAs/GaSb strain layer superlattice detector with nBn design. *Appl. Phys. Lett.*, 92(18):183502, 2008.

[10] P.-Y. Delaunay, B.-M. Nguyen, D. Hoffman, E. K.-W. Huang, and M. Razeghi. Background Limited Performance of Long Wavelength Infrared Focal Plane Arrays Fabricated From M-Structure InAs/GaSb Superlattices. *IEEE J. Quantum Electron.*, 45(2):157–162, 2009.

[11] R. Rehm, M. Walther, J. Schmitz, J. Fleissner, J. Ziegler, W. Cabanski, and R. Breiter. Dual-colour thermal imaging with InAs/GaSb superlattices in mid-wavelength infrared spectral range. *Electron. Lett.*, 42(10):577–578, 2006.

[12] W. W. Bewley, E. H. Aifer, C. L. Felix, I. Vurgaftman, J. R. Meyer, C.-H. Lin, S. J. Murry, D. Zhang, and S. S. Pei. High-temperature type-II superlattice diode laser at $\lambda = 2.9$ μm. *Appl. Phys. Lett.*, 71(25):3607–3609, 1997.

[13] M. E. Flatté, T. C. Hasenberg, J. T. Olesberg, S. A. Anson, T. F. Boggess, C. Yan, and D. L. McDaniel, Jr. III-V interband 5.2 μm laser operating at 185 K. *Appl. Phys. Lett.*, 71(26):3764–3766, 1997.

[14] J. T. Olesberg, M. E. Flatté, T. C. Hasenberg, and C. H. Grein. Mid-infrared InAs/GaInSb separate confinement heterostructure laser diode structures. *J. Appl. Phys.*, 89(6):3283–3289, 2001.

[15] F. Fuchs, N. Herres, J. Schmitz, K. M. Pavlov, J. Wagner, P. Koidl, and J. H. Roslund. InAs/GaSb superlattices characterized by high resolution X-ray diffraction and infrared optical spectroscopy. In *Growth and Characterization of Materials for Infrared Detectors II*, volume 2554 of *Proc. SPIE*, pages 70–77, 1995.

[16] R. Hao, Y. Xu, Z. Zhou, Z. Ren, H. Ni, Z. He, and Z. Niu. Growth of GaSb layers on GaAs (001) substrate by molecular beam epitaxy. *J. Phys. D.: Appl. Phys.*, 40(4):1080–1084, 2007.

[17] J. W. Matthews and A. E. Blakeslee. Defects in Epitaxial Multilayers I: Misfit Dislocations. *J. Crystal Growth*, 27:118–125, 1974.

[18] B. R. Bennett. Strain relaxation in InAs/GaSb heterostructures. *Appl. Phys. Lett.*, 73(25):3736–3738, 1998.

[19] D. Effer and P. J. Etter. An investigation into the apparent purity limit in GaSb. *J. Phys. Chem. Solids*, 25(5):451–460, 1964.

[20] M. Ichimura, K. Higuchi, Y. Hattori, T. Wada, and N. Kitamura. Native defects in the $Al_xGa_{1-x}Sb$ alloy semiconductor. *J. Appl. Phys.*, 68(12):6153–6158, 1990.

[21] H. Kroemer. A Proposed Class of Heterojunction Injection Lasers. *Proc. IEEE*, 51:1782–1783, 1963.

[22] L. Esaki and R. Tsu. Superlattice and Negative Differential Conductivity in Semiconductors. *IBM J. Res. Dev.*, 14(61):61–65, 1970.

[23] H. Sakaki, L. L. Chang, G. A. Sai-Halasz, C. A. Chang, and L. Esaki. Two-dimensional electronic structure in InAs-GaSb superlattices. *Solid State Commun.*, 26(9):589–592, 1978.

[24] D. L. Smith and C. Mailhiot. Proposal for strained type II superlattice infrared detectors. *J. Appl. Phys.*, 62(6):2545–2548, 1987.

[25] D. Hoffman, A. Gin, Y. Wei, A. Hood, F. Fuchs, and M. Razeghi. Negative and Positive Luminescence in Midwavelength Infrared InAs/GaSb Superlattice Photodiodes. *IEEE J. Quantum Electron.*, 41(12):1474–1479, 2005.

[26] A. Krier, M. K. Parry, and D. S. Lancaster. Optoelectronic properties of gallium antimonide light emitting diodes. *Semicond. Sci. Technol.*, 6(11):1066–1071, 1991.

[27] C. H. Wang, J. G. Crowder, V. Mannheim, T. Ashley, D. T. Dutton, A. D. Johnson, G. J. Pryce, and S. D. Smith. Detection of nitrogen dioxide using a room temperature operation mid-infrared InSb light emitting diode. *Electron. Lett.*, 34(3):300–301, 1998.

[28] R. Q. Yang. Infrared laser based on intersubband transitions in quantum wells. *Superlattice Microst.*, 17(1):77–83, 1995.

[29] R. Q. Yang, C.-H. Lin, P. C. Chang, S. J. Murry, D. Zhang, S. S. Pei, S. R. Kurtz, A.-N. Chu, and F. Ren. Mid-IR interband cascade electroluminescence in type-II quantum wells. *Electron. Lett.*, 32(17):1621–1622, 1996.

[30] R. Q. Yang, C.-H. Lin, S.J. Murry, S.S. Pei, H.C. Liu, M. Buchanan, and E. Dupont. Interband cascade light emitting diodes in the 5-8 μm spectrum region. *Appl. Phys. Lett.*, 70:2013–2015, 1997.

[31] J. R. Meyer, I. Vurgaftman, R. Q. Yang, and L. R. Ram-Mohan. Type-II and type-I interband cascade lasers. *Electron. Lett.*, 32(1):45–46, 1996.

[32] A. Krier, H. H. Gao, and V. V. Sherstnev. Investigation of rare earth gettering for the fabrication of improved mid-infrared LEDs. *IEEE Proc-Optoelectron.*, 147(3):217–221, 2000.

[33] A. Krier and X. L. Huang. Design considerations for uncooled InAs mid-infrared light emitting diodes grown by liquid phase epitaxy. *J. Phys. D.: Appl. Phys.*, 39:255–261, 2006.

[34] A. Krier and V. V. Sherstnev. Powerful interface light emitting diodes for methane gas detection. *J. Phys. D.: Appl. Phys.*, 33(2):101–106, 2000.

[35] A. Krier, V. V. Sherstnev, and H. H. Gao. A novel LED module for the detection of H_2S at 3.8 μm. *J. Phys. D.: Appl. Phys.*, 33(14):1656–1661, 2000.

[36] M. Aidaraliev, N. V. Zotova, S. A. Karandashev, B. A. Matveev, M. A. Remennyi, N. M. Stus, G. N. Talalakin, and V. V. Shustov. Two-Wavelength Emission from a GaInPAsSb-InAs Structure with a Broken-Gap Isotype Heterojunction and a p-n Junction in the Substrate. *Tech. Phys. Lett.*, 28:1001–1003, 2002.

[37] T. N. Danilova, B. E. Zhurtanov, A. N. Imenkov, and Yu. P. Yakovlev. Light-Emitting Diodes Based on GaSb Alloys for the 1.6-4.4 μm Mid-Infrared Spectral Range. *Semiconductors*, 39(11):1281–1311, 2005.

[38] E. A. Grebenshchikova, A. N. Imenkov, B. E. Zhurtanov, T. N. Danilova, A. V. Chernyaev, N. V. Vlasenko, and Yu. P. Yakovlev. Properties of GaSb-based light-emitting diodes with chemically cut substrates. *Semiconductors*, 37(12):1414–1420, 2003.

[39] B. Matveev, N. Zotova, N. Il'lnskaya, S. Karandashov, M. Remennyi, N. Stus, and G. Talalakin. Radiation Source. UK Patent GB 2,363,906, Oct. 26, 2003.

[40] B. Matveev, N. Zotova, N. Il'lnskaya, S. Karandashov, M. Remennyi, N. Stus, and G. Talalakin. Radiation Source. US Patent 6,876,006, Apr. 5, 2005.

[41] N. C. Das. Increase in midwave infrared light emitting diode light output due to substrate thinning and texturing. *Appl. Phys. Lett.*, 90(1):011111, 2007.

[42] N. C. Das, J. Bradshaw, F. Towner, and R. Leavitt. Long-wave (10 μm) infrared light emitting diode device performance . *Solid State Electron*, 52(11):1821–1824, 2008.

[43] N. C. Das, W. Chang, G. Simonis, and M. Tobin. MWIR LED array for high temperature target simulation. In Jr. Robert Lee Murrer, editor, *Technologies for Synthetic Environments: Hardware-in-the-Loop Testing XI*, volume 6208 of *Proc. SPIE*, 2006.

[44] M. A. Omar. *Elementary Solid State Physics*. Addison-Wesley Publishing Company, 1993.

[45] S. M. Sze. *Semiconductor Devices, Physics and Technology*. John Wiley and Sons, 2001.

[46] W. Shockley and W. T. Read. Statistics of the Recombinations of Holes and Electrons. *Phys. Rev.*, 87(5):835–842, Sep 1952.

[47] R. N. Hall. Electron-Hole Recombination in Germanium. *Phys. Rev.*, 87(2):387, Jul 1952.

[48] G. P. Agrawal and N. K. Dutta. *Semiconductor Lasers*. Van Nostrand Reinhold, New York, 1993.

[49] M. P. Mikhailova, N. D. Stoyanov, O. V. Anderychuk, K. D. Moiseev, I. A. Andreev, Y. P. Yakovlev, and M. A. Afrailov. Type II GaSb based photodiodes operating in the spectral range 1.5-4.8 μm at room temperature. *IEEE Proc-Optoelectron.*, 149(1):41–44, 2002.

[50] W. R. Frensley. *VLSI Electronics: Microstructure Science*, chapter Heterostructure and Quantum Well Physics. Academic Press, San Diego, 1994.

[51] B. Rotelli, L. Tarricon, E. Gombia, R. Mosca, and M. Perotin. Photoelectric properties of GaSb Schottky diodes. *J. Appl. Phys.*, 81:1813–1819, 1997.

[52] M. A. Herman and H. Sitter. *Molecular Beam Epitaxy: Fundamentals and Current Status*, chapter 1, pages 36–47. Springer-Verlag, Heidelberg, 1996.

[53] P. Cohen, G. S. Petrich, and G. J. Whaley. *Molecular Beam Epitaxy: Applications to Key Materials*, chapter Reflection High Enery Electron Diffraction Studies of the Dynamics of Molecular Beam Epitaxy. Noyes Publications, Park Ridge, NJ, 1995.

[54] E. M. Jackson, G. I. Boishin, E. H. Aifer, B. R. Bennett, and L. J. Whitman. Arsenic cross-contamination in GaSb/InAs superlattices. *J. Crystal Growth*, 270:301–308, 2004.

[55] J. Schmitz, J. Wagner, M. Maier, H. Obloh, P. Koidl, and J. D. Ralston. Unintentional As incorporation in molecular beam epitaxially grown InAs/AlSb/GaSb heterostructures. *J. Electron Mater.*, 23(11):1203–1207, 1994.

[56] J. D. Grange. *The Growth of the MBE III-V Compounds and Alloys*, chapter 3, pages 47–59. Plenum Press, New York, 1985.

[57] C. E. C. Wood, K. Singer, T. Ohashi, L. R. Dawson, and A. J. Noreika. A pragmatic approach to adatom-induced surface reconstruction of III-V compounds. *J. Appl. Phys.*, 54(5):2732–2737, 1983.

[58] S. C. Jain, M. Willander, and H. Maes. Stresses and strains in epilayers, stripes and quantum structures of III-V compound semiconductors. *Semicond. Sci. Technol.*, 11:641–671, 1996.

[59] C. H. Grein, P. M. Young, M. E. Flatté, and H. Ehrenreich. Long wavelength InAs/InGaSb infrared detectors: Optimization of carrier lifetimes. *J. Appl. Phys.*, 78(12):7143–7152, 1995.

[60] R. Beanland, D. J. Dunstan, and P. J. Goodhew. Plastic relaxation and relaxed buffer layers for semiconductor epitaxy. *Adv. Phys.*, 45(2):87–146, 1996.

[61] K. Takahashi, H. Kawada, S. Ueda, M. Furuse, and S. Shirayone. The origins and elimination of oval defects in GaAs layers grown by molecular beam epitaxy. *J. Vac. Sci. Technol. A*, 9(3):854–857, 1991.

[62] S. Izumi, T. Sonoda, N. Hayafuji, S. Mitsui, and S. Takamiya. Less than 10 defects/cm$^2 \cdot \mu$m in molecular beam epitaxy grown GaAs by arsenic cracking. *J. Crystal Growth*, 150(1-4):7 – 12, 1995.

[63] C. J. Vineis, C. A. Wang, and K. F. Jensen. In-situ reflectance monitoring of GaSb substrate oxide desorption. *J. Crystal Growth*, 225(2-4):420 – 425, 2001.

[64] Z. Y. Liu, B. Hawkins, and T. F. Kuech. Chemical and structural characterization of GaSb(100) surfaces treated by HCl-based solutions and annealed in vacuum. *J. Vac. Sci. Technol. B*, 21(1):71–77, 2003.

[65] T. Van Buuren, M. K. Weilmeier, I. Athwal, K. M. Colbow, J. A. Mackenzie, T. Tiedje, P. C. Wong, and K. A. R. Mitchell. Oxide thickness effect and surface roughening in the desorption of the oxide from GaAs. *Appl. Phys. Lett.*, 59(4):464–466, 1991.

[66] N. Bertru, M. Nouaoura, J. Bonnet, L. Lassabatere, E. Bedel, and M. Mamy. Preparation of GaSb(100) surfaces by ultraviolet irradiation. *J. Vac. Sci. Technol. A*, 15(4):2043–2050, 1997.

[67] J. S. Solomon, L. Petry, and D. H. Tomich. Optimizing GaSb($\overline{111}$) and GaSb(001) surfaces for epitaxial film growth. *Thin Sol. Films*, 343-344:500 – 503, 1999.

[68] G. R. Bell and C. F. McConville. Atomic hydrogen cleaning of GaSb(001) surfaces. *Appl. Phys. Lett.*, 69(18):2695–2697, 1996.

[69] E. Weiss, O. Klin, S. Grossman, S. Greenberg, P. C. Klipstein, R. Akhvlediani, R. Tessler, R. Edrei, and A. Hoffman. Hydrogen and thermal deoxidations of InSb and GaSb substrates for molecular beam epitaxial growth. *J. Vac. Sci. Technol. A*, 25(4):736–745, 2007.

[70] D. A. Allwood, S. Cox, N. J. Mason, R. Palmer, R. Young, and P. J. Walker. Monitoring epiready semiconductor wafers. *Thin Sol. Films*, 412:76–83, 2002.

[71] C. A. Wang, D. A. Shiau, and A. Lin. Preparation of GaSb substrates for GaSb and GaInAsSb growth by organometallic vapor phase epitaxy. *J. Crystal Growth*, 261(2-3):385–392, 2004.

[72] E. Papis, A. Kuda, T. T. Piotrowski, K. Goaszewska, E. Kamiska, and A. Piotrowska. Ellipsometric investigations of (100) GaSb surface under chemical etching and sulfide treatment. *Mater. Sci. Semicond. Process.*, 4(1-3):293–295, 2001.

[73] F. W. O. Da Silva, C. Raisin, N. Silga, M. Nouaoura, and L. Lassabatere. Chemical preparation of GaSb (001) substrates prior to MBE. *Semicond. Sci. Technol.*, 4:565–569, 1989.

[74] B. Z. Nosho, B. R. Bennett, E. H. Aifer, and M. Goldenberg. Surface morphology of homoepitaxial GaSb films grown on flat and vicinal substrates. *J. Crystal Growth*, 236(1-3):155–164, 2002.

[75] A. Szerling, K. Kosiel, A. Wojcik-Jedlinska, M. Pluska, and M. Bugajski. Properties and origin of oval defects in epitaxial structures grown by molecular beam epitaxy. *Opt. Appl.*, 35(3):537–548, 2005.

[76] A. S. Bracker, M. J. Yang, B. R. Bennett, J. C. Culbertson, and J. W. Moore. Surface reconstruction phase diagrams for InAs, AlSb, and GaSb. *J. Crystal Growth*, 220:384–392, 2000.

[77] E. H. Aifer, E. M. Jackson, B. R. Bennett, L. Vurgaftman, J. R. Meyer, and G. G. Jernigan. Suppression Of Bulk Defects In Antimonide Superlattice Infrared Photodiodes. In *Mat. Res. Soc. Symp. Proc.*, volume 722, 2002.

[78] K. Möller, L. Töben, Z. Kollonitsch, Ch. Giesen, M. Heuken, F. Willig, and T. Hannappel. In-situ monitoring and analysis of GaSb(100) substrate deoxidation. *Appl. Surf. Sci.*, 242:392–398, 2005.

[79] P. S. Dutta, H. L. Bhat, and V. Kumar. The physics and technology of gallium antimonide: An emerging optoelectronic material. *J. Appl. Phys.*, 81(9):5821–5870, 1997.

[80] I. Horcas, R. Fernández, J. M. Gómez-Rodríguez, J. Colchero, J. Gómez-Herrero, and A. M. Baro. WSXM: A software for scanning probe microscopy and a tool for nanotechnology. *Rev. Sci. Instrum.*, 78(1):013705, 2007.

[81] D. M. Hofmann, D. Kovalev, G. Steude, B. K. Meyer, A. Hoffmann, L. Eckey, R. Heitz, T. Detchprom, H. Amano, and I. Akasaki. Properties of the yellow luminescence in undoped GaN epitaxial layers. *Phys. Rev. B.*, 52(23):16702–16706, Dec 1995.

[82] W. Grieshaber, E. F. Schubert, I. D. Goepfert, Jr. R. F. Karlicek, M. J. Schurman, and C. Tran. Competition between band gap and yellow luminescence in GaN and its relevance for optoelectronic devices. *J. Appl. Phys.*, 80(8):4615–4620, 1996.

[83] J. J. Zinck, E. J. Tarsa, B. Brar, and J. S. Speck. Desorption behavior of antimony multilayer passivation on GaAs (001). *J. Appl. Phys.*, 82:6067–6072, 1997.

[84] S. G. Alcock, M. J. Everard, C. L. Nicklin, J. S. G. Taylor, C. A. Norris, and S. L. Bennett. An investigation of the growth and removal of protective antimony caps for antimonide epilayers. *Thin Sol. Films*, 514:198–203, 2006.

[85] J. P. Faurie, A. Million, and G. Jacquier. Molecular-Beam Epitaxy of CdTe and $Cd_xHg_{1-x}Te$. *Thin Sol. Films*, 90(1):107–112, 1982.

[86] L. M. Murray, E. J. Koerperick, T. F. Boggess, and J. P. Prineas. Photoluminescence Optimizations of InAs/GaSb Superlattices. *Submitted to J. Crystal Growth.*

[87] L. Esaki. New Phenomenon in Narrow Germanium $p-n$ Junctions. *Phys. Rev.*, 109(2):603–604, Jan 1958.

[88] O. Dier, M. Grau, C. Lauer, C. Lin, and M.-C. Amann. Diffusion of dopants in highly (similar to 10^{20} cm^{-3}) n- and p-doped GaSb-based materials. *J. Vac. Sci. Technol. B*, 23:349–353, 2005.

[89] S. Koumetz, J. Marcon, K. Ketata, M. Ketata, and P. Launay. Beryllium diffusion in InGaAs compounds grown by chemical beam epitaxy. *J. Phys. D.: Appl. Phys.*, 30(5):757–762, 1997.

[90] R. Q. Yang and Y. Qiu. Bipolar cascade lasers with quantum well tunnel junctions. *J. Appl. Phys.*, 94(11):7370–7372, 2003.

[91] A. Lyakh and P. Zory. Gallium Arsenide-Based Bipolar Cascade Lasers With Deep Quantum-Well Tunnel Junctions. *IEEE Photon. Technol. Lett.*, 18(24):2656–2658, 2006.

[92] J. Steinshnider, M. Weimer, R. Kaspi, and G.W. Turner. Visualizing Interfacial Structure at Non-Common-Atom Heterojunctions with Cross-Sectional Scanning Tunneling Microscopy. *Phys. Rev. Lett.*, 85(14):2593–2596, 2000.

[93] R. Kaspi, J. Steinshnider, M. Weimer, C. Moeller, and A. Ongstad. As-soak control of the InAs-on-GaSb interface. *J. Crystal Growth*, 225:544–549, 2001.

[94] R. Kaspi. Compositional abruptness at the InAs-on-GaSb interface: optimizing growth by using the Sb desorption signature. *J. Crystal Growth*, 201/202:864–867, 1999.

[95] Y. Horikoshi. Advanced epitaxial growth techniques: atomic layer epitaxy and migration-enhanced epitaxy. *J. Crystal Growth*, 201/202:150–158, 1999.

[96] D. H. Chow, R. H. Miles, and A. T. Hunter. Effects of interface stoichiometry on the structural and electronic properties of $Ga_{1-x}In_xSb$/InAs superlattices. *J. Vac. Sci. Technol. B*, 10(2):888–891, 1992.

[97] B. R. Bennett, B. V. Shanabrook, R. J. Wagner, J. L. Davis, and J. R. Waterman. Control of interface stoichiometry in InAs/GaSb superlattices grown by molecular beam epitaxy. *Appl. Phys. Lett.*, 63(7):949–951, 1993.

[98] B. Satpati, J. B. Rodriguez, A. Trampert, E. Tournié, A. Joullié, and P. Christol. Interface analysis of InAs/GaSb superlattice grown by MBE. *J. Crystal Growth*, 301-302:889 – 892, 2007. 14th International Conference on Molecular Beam Epitaxy - MBE XIV.

[99] R. J. Nelson and R. G. Sobers. Minority-carrier lifetimes and internal quantum efficiency of surface-free GaAs. *J. Appl. Phys.*, 49(12):6103–6108, 1978.

[100] E. Dupont, M. Gao, M. Buchanan, Z. R. Wasilewski, and H. C. Liu. Optimization of p-doping in GaAs photon-recycling light-emitting diodes operated at low temperature. *Semicond. Sci. Technol.*, 16(5):L21–L23, 2001.

[101] L. Tapfer. X-ray Investigation Of Multilayered Semiconductor Heterostructures. *Lasers and Electro-Optics Society Annual Meeting, 1992. LEOS '92, Conference Proceedings*, pages 131–132, Nov 1992.

[102] E. F. Schubert and N. E. J. Hunt. 15 000 hrs stable operation of resonant cavity light emitting diodes. *Appl. Phys. A.-Mater*, 66(3):319–321, 1998.

[103] N. C. Das, M. Taysing-Lara, K. A. Olver, F. Kiamilev, J. P. Prineas, J. T. Olesberg, E. J. Koerperick, L. M. Murray, and T. F. Boggess. Flip Chip Bonding of 68×68 MWIR LED Arrays. *IEEE T. Electron. Pa. M.*, 32(1):9–13, Jan. 2009.

[104] P. S. Dutta, K. S. Sangunni, H. L. Bhat, and V. Kumar. Sulphur passivation of gallium antimonide surfaces. *Appl. Phys. Lett.*, 65(13):1695–1697, 1994.

[105] A. Gin, Y. Wei, A. Hood, A. Bajowala, V. Yazdanpanah, M. Razeghi, and M. Tidrow. Ammonium sulfide passivation of Type-II InAs/GaSb superlattice photodiodes. *Appl. Phys. Lett.*, 84(12):2037–2039, 2004.

[106] A. Vogt, A. Simon, J. Weber, H. L. Hartnagel, J. Schikora, V. Buschmann, and H. Fuess. Non-annealed ohmic contacts to p-GaSb grown by molecular beam epitaxy. *Mat. Sci. Eng. B.-Solid*, 66(1-3):199–202, 1999.

[107] N. C. Das, F. Kiamilev, J. P. Prineas, J. T. Olesberg, E. J. Koerperick, L. M. Murray, and T. F. Boggess. Performance of 64x64 MWIR super lattice light-emitting diode (SLED) array for IR scene generation. In *Technologies for Synthetic Environments: Hardware-in-the-Loop Testing XIII*, volume 6942, page 69420I. SPIE, 2008.

[108] E. J. Koerperick, J. T. Olesberg, T. F. Boggess, J. L. Hicks, L. S. Wassink, L. M. Murray, and J. P. Prineas. InAs/GaSb cascaded active region superlattice light emitting diodes for operation at 3.8 μm. *Appl. Phys. Lett.*, 92(12):121106, 2008.

[109] E. J. Koerperick, J. T. Olesberg, J. L. Hicks, J. P. Prineas, and T. F. Boggess. Active Region Cascading for Improved Performance in InAs/GaSb Superlattice LEDs. *IEEE J. Quantum Electron.*, 44(12):1242–1247, 2008.

[110] E. J. Koerperick, J. T. Olesberg, J. L. Hicks, J. P. Prineas, and T. F. Boggess. High Power MWIR Cascaded InAs/GaSb Superlattice Light Emitting Diodes. *IEEE J. Quantum Electron.*, 45(7):849–853, 2009.

[111] E. J. Koerperick, J. T. Olesberg, D. T. Norton, B. V. Olson, J. P. Prineas, and T. F. Boggess. Cascaded Superlattice InAs/GaSb Light Emitting Diodes for Operation in the Long-Wave Infrared. *In preparation for submission to Applied Physics Letters.*

[112] M. E. Twigg, B. R. Bennett, B. V. Shanabrook, J. R. Waterman, J. L. Davis, and R. J. Wagner. Interfacial roughness in InAs/GaSb superlattices. *Appl. Phys. Lett.*, 64(25):3476–3478, 1994.

[113] Q. Xie, J. E. Van Nostrand, J. L. Brown, and C. E. Stutz. Arsenic for antimony exchange on GaSb, its impacts on surface morphology, and interface structure. *J. Appl. Phys.*, 86(1):329–337, 1999.

[114] L. Tapfer, W. Stolz, A. Fischer, and K. Ploog. High Resolution Double-Crystal X-ray Diffraction for Improved Assessment of Modulated Semiconductor Structures. *Surf. Sci.*, 174:88–93, 1986.

[115] A. Chandola, R. Pino, and P. S. Dutta. Below bandgap optical absorption in tellurium-doped GaSb. *Semicond. Sci. Technol.*, 20(8):886–893, 2005.